



University of Kentucky
UKnowledge

Theses and Dissertations--Mechanical
Engineering

Mechanical Engineering


2021

Tailoring Texture, Microstructure, and Shape Memory Behavior of NiTi Alloys Fabricated by L-PBF-AM

Sayed Ehsan Saghaian N.E.

University of Kentucky, ehsansaghaian@gmail.com

Author ORCID Identifier:

 <https://orcid.org/0000-0003-0070-0958>

Digital Object Identifier: <https://doi.org/10.13023/etd.2021.212>

[Right click to open a feedback form in a new tab to let us know how this document benefits you.](#)

Recommended Citation

Saghaian N.E., Sayed Ehsan, "Tailoring Texture, Microstructure, and Shape Memory Behavior of NiTi Alloys Fabricated by L-PBF-AM" (2021). *Theses and Dissertations--Mechanical Engineering*. 171.
https://uknowledge.uky.edu/me_etds/171

This Doctoral Dissertation is brought to you for free and open access by the Mechanical Engineering at UKnowledge. It has been accepted for inclusion in Theses and Dissertations--Mechanical Engineering by an authorized administrator of UKnowledge. For more information, please contact UKnowledge@lsv.uky.edu.

STUDENT AGREEMENT:

I represent that my thesis or dissertation and abstract are my original work. Proper attribution has been given to all outside sources. I understand that I am solely responsible for obtaining any needed copyright permissions. I have obtained needed written permission statement(s) from the owner(s) of each third-party copyrighted matter to be included in my work, allowing electronic distribution (if such use is not permitted by the fair use doctrine) which will be submitted to UKnowledge as Additional File.

I hereby grant to The University of Kentucky and its agents the irrevocable, non-exclusive, and royalty-free license to archive and make accessible my work in whole or in part in all forms of media, now or hereafter known. I agree that the document mentioned above may be made available immediately for worldwide access unless an embargo applies.

I retain all other ownership rights to the copyright of my work. I also retain the right to use in future works (such as articles or books) all or part of my work. I understand that I am free to register the copyright to my work.

REVIEW, APPROVAL AND ACCEPTANCE

The document mentioned above has been reviewed and accepted by the student's advisor, on behalf of the advisory committee, and by the Director of Graduate Studies (DGS), on behalf of the program; we verify that this is the final, approved version of the student's thesis including all changes required by the advisory committee. The undersigned agree to abide by the statements above.

Sayed Ehsan Saghaian N.E., Student

Dr. Haluk E. Karaca, Major Professor

Dr. Alexandre Martin, Director of Graduate Studies

TAILORING TEXTURE, MICROSTRUCTURE, AND
SHAPE MEMORY BEHAVIOR OF NiTi ALLOYS
FABRICATED BY L-PBF-AM

DISSERTATION

A dissertation submitted in partial fulfillment of the
requirements for the degree of Doctor of Philosophy in the
College of Engineering
at the University of Kentucky

By:

Sayed Ehsan Saghaian

Lexington, Kentucky

Director: Dr. Haluk E. Karaca, Professor of Mechanical Engineering
Lexington, Kentucky
2021

Copyright © Sayed E. Saghaian 2021
<https://orcid.org/0000-0003-0070-0958>

ABSTRACT OF THE DISSERTATION

TAILORING TEXTURE, MICROSTRUCTURE, AND SHAPE MEMORY BEHAVIOR OF NiTi ALLOYS FABRICATED BY L-PBF- AM

Laser Powder Bed Fusion (L-PBF) is one of the most promising Additive Manufacturing (AM) methods to fabricate near net-shape metallic materials for a wide range of applications such as patient-specific medical devices, functionally graded materials, and complex structures. NiTi shape memory alloys (SMAs) are of great interest due to a combination of unique features, such as superelasticity, shape memory effect, high ductility, work output, corrosion resistance, and biocompatibility that could be employed in many applications in automotive, aerospace, and biomedical industries. Due to the difficulties with traditional machining and forming of NiTi components, the ability to fabricate complex parts, tailor properties that can show superelasticity, and fabricating highly textured alloys via AM is a paradigm shift for its shape memory alloy applications. Therefore, this study aims to establish process parameters, building strategy, microstructure, and property relationship of NiTi alloys. It will present that process parameters, sample orientation, loading type, and post heat treatments can be used effectively to tailor the transformation temperatures, grain shapes and sizes, texture, strength, transformation strain, and superelasticity of L-PBF-AM NiTi.

The AM process parameters (PPs) govern the solidification characteristics, thermal gradient directions, competitive grain growth mechanisms, partial re-melting of the previous laser tracks and layers, which highly affect the composition, grain shape and size, texture, and thus mechanical properties of fabricated materials. Therefore, a comprehensive and systematic study is conducted to gain an in-depth understanding of the relationship between the AM processing parameters, microstructure, and shape memory properties of NiTi alloys fabricated by using the Ni-rich Ni_{50.8}Ti_{49.2} (at. %) powder. It was found that the decrease of laser power from 250 to 100 W, scanning speed from 1250 to 125 mm/s, and hatch spacing from 80 to 40 μm alter the texture from the [001] to [111] orientation along the building direction. Moreover, it was revealed that transformation temperatures (TTs), microstructure, and the correlated thermo-mechanical response could be significantly changed with the process parameters. By the careful selection of PPs, as-fabricated NiTi samples can show superelasticity with 6% recovery and a recovery ratio of more than 87%.

The shape memory behavior of NiTi alloys is highly texture/orientation dependent. Thus, it was hypothesized that the properties of NiTi alloys can be tailored by not only altering the process parameters but also adjusting the relative position of the sample orientation to the building direction, BD. Fabrication of the samples along different directions (loading directions, LD) relative to the BD impacts the re-melting and reheating

processes of the layers, altering the texture of the fabricated samples along the testing direction. Moreover, since the impact of defects (e.g., cracks, pores) and crystallographic orientation formed during L-PBF-AM on the strength and shape memory behavior of NiTi could significantly be different in respect to the loading mode (compression or tension), both dog bone tensile and rectangular compressive samples were fabricated along the selected directions. It was revealed that when the LD was altered from 0 or 90 degrees (respect to the build plate) to 45 degree, the texture along the LD was altered from [100] to [110] orientation and significantly lowered the transformation stress. These texture variations created anisotropic compression-tension behaviors with deformation patterns consistent with single crystals. The [001]-textured parts showed higher strength and lower transformation strain (2.87% @ 200 MPa in tension for 0 degree), while the [110] samples showed higher transformation strain at lower stresses (5.31% @ 150 MPa in tension for 45 degree).

Heat treatment is a very efficient method to control the TTs and improve the strength of Ni-rich NiTi alloys. The chemical composition, volume fraction, and coherency of the precipitates highly impact the TTs, matrix strength, hardness, and martensitic morphology and shape memory behavior of Ni-rich NiTi alloys. Therefore, post-heat treatment effects on the transformation characteristics (TTs, thermal hysteresis, and recoverable strain) and the microstructure of the L-PBF-AM Ni-rich NiTi SMAs have been investigated through transmission electron microscopy, thermal cycling under stress, and isothermal stress-strain experiments. L-PBF-AM NiTi samples were fabricated with laser power of 250 W, scanning speed of 1250 mm/s, and hatch spacing of 80 μm to show improved shape memory response as they presented strong [001] texture. It was revealed that post heat treatment at 500 °C for 1.5 h increased the TTs, decrease the hysteresis, and significantly improve the strength of the L-PBF-AM samples due to the formation of coherence precipitates. Perfect superelastic behavior with superelastic strain of 7% and superelastic window of 100 °C was observed for aged L-PBF-AM samples.

KEYWORDS: Additive Manufacturing, Laser Powder Bed Fusion, Shape Memory Alloys, Material Characterization, Texturing, NiTi

Sayed Ehsan Saghaian

05//2021

TAILORING TEXTURE, MICROSTRUCTURE, AND SHAPE
MEMORY BEHAVIOR OF NiTi ALLOYS FABRICATED BY L-
PBF-AM

By

Sayed Ehsan Saghaian

Haluk E. Karaca

Director of Dissertation

Alexandre Martin

Director of Graduate Studies

05//2021

This work is dedicated to my beautiful wife and my great parents.

ACKNOWLEDGEMENTS

First and foremost, I would like to express my special appreciation and thanks to my advisor Prof. Haluk Karaca, who has been a tremendous mentor. I would like to thank him for encouraging me and for allowing me to grow as a researcher. His patience and endless support have been invaluable throughout this time. This dissertation could not have been made possible without his immense guidance and valuable comments.

I would like to thank my committee members Dr. Ebrahim Jawahir, Dr. Y.T Cheng, Dr. Y. Charles Lu, Dr. Babak Bazrgari, and Dr. Mohammad Elahinia, for their help. I would like to express my gratitude to our collaborator at the University of Toledo, Prof. M. Elahinia, for his valuable suggestions and support. Also, I should mention his research group in Dynamic and smart systems lab of the University of Toledo for sample fabrications.

Special thanks to my former and current lab-mates Soheil Saedi, Peizhen Li, Guher Pelin Toker, Ankur Madjmur, Bhargava Boddeti, Utsav Shah, and Ausencio Fuentes. I also appreciate the generous help of technicians of the mechanical engineering department.

Words are not enough to express how grateful I am to my amazing family, particularly my wife Sepideh Dadkhah, parents, brothers Yasser and Mohammad Saghaian, and my handsome boys Elias and Zachary for their love, support, and constant encouragement; I have gotten over the years.

Table of Contents

ACKNOWLEDGEMENTS	iii
List of Tables	viii
List of Figures	ix
1 Introduction	1
1.1A brief background on shape memory alloys (SMAs).....	1
1.1.1 Thermal Induced Martensitic Transformation	2
1.1.2 Shape Memory Effect (SME).....	4
1.1.3 Superelasticity	5
1.2 Binary NiTi	8
1.2.1 Impact of composition on NiTi	9
1.2.2 Impact of heat treatment on NiTi	11
1.2.3 Impact of loading Mode (LD) on NiTi.....	13
1.2.4 Impact of Crystallographic orientation on NiTi.....	14
1.3 NiTi Fabrication	17
1.4 L-PBF-AM NiTi.....	18
1.5 Motivation and Statement of Problem	21
1.6 Technical Approach and Objectives	23
2 Experimental Procedure	26

2.1	Materials Fabrication.....	26
2.2	Materials Preparation	27
2.3	Heat Treatments	28
2.4	Calorimetry Measurements	29
2.5	Microstructural Analysis	30
2.6	Mechanical Testing	32
3	Impact of L-PBF-AM Process Parameters (PPs).....	34
3.1	Fabrication.....	34
3.2	Microstructure	35
3.3	Transformation Temperatures	44
3.4	Mechanical Behavior.....	46
3.5	Discussion	53
3.6	Conclusion.....	60
4	Impact of Building direction (BD) and Loading Mode on L-PBF-AM Ni _{50.8} Ti _{49.2}	62
4.1	Fabrication.....	63
4.2	Phase transformation Responses	64
4.3	Microstructural analysis	66
4.4	Load-biased shape memory behavior.....	69

4.5	Superelastic Cycling.....	74
4.6	Discussion	77
4.7	Conclusion.....	78
5	Effect of Heat Treatment on L-PBF-AM and Conventional NiTi	79
5.1	Stress-free transformation temperatures (TTs)	80
5.2	Microstructure Analysis	82
5.3	Load-biased shape memory behavior.....	85
5.4	Failure response at body temperature.....	88
5.5	Compressive response at selected temperatures.....	90
5.6	Discussion	95
5.6.1	Transformation Strain and Thermal Hysteresis	95
5.6.2	Clausius–Clapeyron relationship and Work Output.....	97
5.6.3	Superelastic Temperature Window, Recovery Ratio, and Stress Hysteresis.....	99
5.6.4	Comparison to other NiTi	102
5.7	Conclusions	105
6	Summary and Future Work	106
6.1	Summary and Conclusion	106
6.2	Future Work	109

7	Contribution	111
	References.....	112
	VITA.....	124

List of Tables

Table 1.1: RSSF and Maximum experimental strain of NiTi under tension and compression [9].....	16
Table 3.1 List of L-PBF-AM fabrication parameters concerning effect of hatch spacing and laser power	35
Table 3.2 Summary of cyclic test results of group A (100 W) and group B (50 W) L-PBF-AM-fabricated Ni _{50.8} Ti _{49.2} SMAs.	52
Table 4.1 TTs of Ni _{50.8} Ti _{49.2} (at. %) in forms of ingot, powder, and selectively laser melted extracted from DSC graphs. (M _s -Martensite start, M _f - Martensite finish, A _s -Austenite start, and A _f -Austenite finish).....	65
Table 4.2 Summary of cyclic test results of compressive L-PBF-AM Ni _{50.8} Ti _{49.2} SMAs.	77

List of Figures

Figure 1.1: Thermal induce phase transformation in the absence (a) and presence (b) of applied stress [9].....	4
Figure 1.2: Schematic of shape memory effect and superelasticity behavior of SMAs [9].....	5
Figure 1.3 Perfect superelastic behavior of SMAs	6
Figure 1.4 Schematic illustration of stress–strain curves of a SMA at three typical temperature regions (a) ($T < M_f$),(b)($A_f < T < M_d$), (c) ($T > M_d$) [10], and (d)Schematic for the critical stresses of various deformation modes as a function of temperature in SMAs [9].....	8
Figure 1.5 M_s temperature as a function of Ni content for NiTi SMAs [42].....	10
Figure 1.6: Stress vs. strain behavior of NiTi as a function of Ni content [10].....	11
Figure 1.7 TEM micrograph from Ni_4Ti_3 precipitates of aged single crystal NiTi [49]	12
Figure 1.8 Deformation behavior of NiTi SMAs under tensile, compressive, and shear stress [55].....	14
Figure 1.9: (a) Superelastic behavior of NiTi SMA as a function of the crystallographic orientation [25].....	16
Figure 1.10 Schematic showing the principle of powder bed-based AM of complex NiTi scaffolds [69].....	18
Figure 2.1 Phenix PXM Selective Laser Melting system [125].	27

Figure 2.2 Electrical Discharge Machining (EDM) [125].	28
Figure 2.3 Whip Mix Pro 200 dental furnace [125].	28
Figure 2.4: Pyris I DSC to measure the stress-free phase TTs [125].	30
Figure 2.5 BUEHLER EcoMet/AutoMet250 Grinder-Polisher [125].	31
Figure 2.6 Keyence VH_Z250R Optical Microscopy [125].	31
Figure 2.7 MTS Landmark servo-hydraulic test platform.	33
Figure 3.1 BD optical micrographs of L-PBF-AM-fabricated Ni _{50.8} Ti _{49.2} samples produced at 100 W and various hatch spacings: A1 (40 μm), A2 (80 μm), A3 (120 μm), A4 (160 μm), A5 (200 μm), A6 (240 μm).	37
Figure 3.2 BD optical micrographs of L-PBF-AM-fabricated Ni _{50.8} Ti _{49.2} samples fabricated at 50 W and various hatch spacing: B1 (40 μm), B2 (80 μm), B3 (120 μm), B4 (160 μm)	39
Figure 3.3 The electron backscatter diffraction (EBSD) inverse pole figures (IPF) maps and respective pole figures (PF) from the 100 W fabrications for A1 = 40μm, A3 = 120 μm, and A6 = 240 μm. IPF maps for A1, A3, and A6 are seen in (a), (b), and (c), respectively. PFs for A1 A3 and A6 are seen in (d), (e), and (f), respectively.	42
Figure 3.4 The electron backscatter diffraction (EBSD) inverse pole figures (IPF) maps and respective pole figures (PF) from the 50 W fabrications for B1 = 40μm, B3 = 120 μm, and B4 = 160 μm. IPF maps for B1, B3, and B4 are seen in (a), (b), and (c), respectively. PFs for B1, B3, and B4 are seen in (d), (e), and (f), respectively.	44

Figure 3.5 DSC results of (a) group A (100W) and (b) group B (50W) specimens, and (c) Effects of hatch spacing and (d) volumetric energy density on TTs (A_s , A_p and A_f) of L-PBF-AM-fabricated $Ni_{50.8}Ti_{49.2}$ at two different laser powers: group A (100 W) and group B (50 W).....	46
Figure 3.6 Compressive stress-strain curves of L-PBF-AM $Ni_{50.8}Ti_{49.2}$ samples fabricated at different hatch spacing, tested at room temperature for (a) group A (100 W) and (b) group B (50 W) laser powers.....	48
Figure 3.7 Compressive stress-strain curves of L-PBF-AM $Ni_{50.8}Ti_{49.2}$ samples fabricated at different hatch spacing for (a) 100 W and (b) 50 W laser powers, tested at temperatures of $A_f\sigma+20$ °C.of each sample.	49
Figure 3.8 Superelastic cycling of L-PBF-AM NiTi with low, 40 μ m, (top) and high hatching spacing, 160 μ m, (bottom) for laser powers of 100 W (left) and 50 W (right) at temperatures of $A_f\sigma+20$ °C	51
Figure 3.9 EBSD IPF maps for representative samples showing the influence of laser processing parameters on the texture development for the samples fabricated with laser powers of 50 W, 100 W, and 250 W [103, 157].....	55
Figure 3.10 (a) Schematic of a melt pool, thermal gradient direction, and grain growth [158, 159]. (b) Impact of altering laser power and scanning speed on melt pool shape and cube crystal turning [160].	57
Figure 3.11 Impact of hatch spacing in solidification and texturing the L-PBF-AM samples [159, 161].....	58

Figure 4.1 Schematics and arrangement of compression and tension samples on the build plate.....	64
Figure 4.2 DSC graphs of Ni _{50.1} Ti _{49.9} (at. %) in forms of powder, ingot, and selectively laser melted.	65
Figure 4.3 EBSD results of LD sections of C0, C45, and C90 specimens. For each specimen OIM, schematic of the section, legends, and (100) and (110) pole figures are presented. LD and BD show loading and building directions, respectively [167].	68
Figure 4.4 Thermal cycling under constant stress responses of L-PBF-AM Ni _{50.8} Ti _{49.2} (at. %) in tensile (right) and compressive (left) conditions with (a) 0, (b) 45, and (c) 90 degree angels between BD and substrate.....	71
Figure 4.5 (a) The evolution of total strain and total irrecoverable strain with stress for tensile (left) and compressive (right) specimens. (b) The changes in TTs with stress for tensile (left) and compressive (right) specimens.	74
Figure 4.6 Superelastic cycling of L-PBF-AM NiTi under compression at $Af\sigma+10\text{ }^{\circ}\text{C}$ for samples: (a) C0, (b) C45, and (c) C90.....	76
Figure 5.1 DSC responses of as-fabricated (Solid line) and aged (Dash line) ingot, SLM120, and SLM80 samples	82
Figure 5.2 Bright field and Z-contrast TEM images of as-fabricated and aged L-PBF-AM alloys. (a) as-fabricated SLM120. (b) as-fabricated SLM80 ((a) and (b) adopted from Ref. [103]). (c) bright field image of aged ingot. Inset shows the [001] diffraction pattern of the matrix. (d) bright field image of aged SLM120. Inset shows the [112] diffraction pattern of the matrix. (e) Z-contrast image of aged SLM120. (f) bright field image of aged	

SLM80. (g) Z-contrast image of aged SLM80. (h) Representative EDS spectrum of a precipitate. Arrows show precipitate and pore features..... 85

Figure 5.3 Thermal cycling under constant stress levels of (a) Ingot, (b) SLM120, and (c) SLM80 for as-fabricated (solid line) and aged (dash line) samples..... 88

Figure 5.4 Failure responses of As-fabricated (Solid line) and Aged (Dash line) samples..... 90

Figure 5.5 Superelastic responses of As-fabricated (Left) and Aged (Right) samples of (a) Ingot, (b) SLM120, and (c) SLM80. 94

Figure 5.6 (a) Recoverable and irrecoverable strains, and (b) thermal hysteresis vs compressive stress of as-fabricated (solid lines) and aged (dash lines) specimens. 97

Figure 5.7 The critical stress versus Ms temperatures of As-fabricated (solid line) and Aged (dash line)..... 99

Figure 5.8 (a) Recovery ration and (b) stress hysteresis versus temperature for as-fabricated (solid line) and aged (dash line) samples..... 102

1 Introduction

1.1 A brief background on shape memory alloys (SMAs)

According to Otsuka and Wayman [1], in 1932, A. Ölander discovered that the residual strain upon unloading applied stress to gold-cadmium (Au-Cd) could fully recover by heating for the first time. Later in 1938, Greninger & Mooradian observed the formation of the martensite phase by changing the temperature of a Cu-Zn alloy [2]. The concept of shape memory effect (SME), which explained the reversible transformation of martensite upon heating, was obtained in CuZn and CuAl by Kurdjumov and Khandros in 1949 [3]. In 1951, Chang and Read [4] used electrical resistivity measurement and X-ray analysis to present the shape memory properties of Au-Cd. In 1963, Buehler and his co-workers at the U.S. Naval Ordnance Laboratory (NOL) were trying to develop lightweight high-temperature aerospace alloys which discovered the shape memory effect in nearly equiatomic nickel-titanium (NiTi) alloys [5]. The alloy was named Nitinol after the laboratory in which it was discovered (Nickel-Titanium Naval Ordnance Laboratory). During their research at NOL, Buehler noticed that the material could recover its original shape along with good mechanical properties. NiTi alloy had the most superior properties compared to other SMAs, including Cu-based SMAs (in particular CuZnAl), NiAl, and FeMnSi. After its discovery, many studies were carried out to elucidate the behavior and remarkable properties of SMA. This also promoted several investigations related to their applications in different potential fields such as aerospace, military, automotive, industrial, and biomedical. The use of NiTi for medical applications was first reported in the 1970s (Cutright et al. 1973, Iwabuchi et al. 1975, Castleman et al. 1976, Simon et al. 1977). It was in the mid-1990s that the first widespread commercial stent applications made their

breakthrough in medicine. Nowadays, NiTi SMAs are among the largest commercial in the field of bioengineering and medical applications [6].

Shape memory alloys (SMA) are a fantastic group of materials that can display large recoverable shape changes, stresses, and work outputs as a result of reversible martensitic transformations. SMAs undergo a solid to solid diffusionless phase transformation and, as a consequence, can produce considerable recoverable shape changes (up to 20% uniaxial strain), stresses (~100-500 MPa), and work output (~10 MJ/m³) [7, 8]. The phase transformation involves the atoms' coordinate motion over very short distances in the crystal as the material structure transforms from one lattice-type to another. The SMAs have two stable phases, the high-temperature phase, called “*austenite*”, and the low-temperature phase, called “*martensite*”. After a mechanical deformation, SMAs can remember their original shape when heated to a specific temperature. Or they can recover a large amount of strain if they deform within a particular temperature range. This solid to solid transformation can be induced either thermally or mechanically. Based on this transformation, two main mechanisms of SMAs, namely SME and Superelasticity (SE), will be discussed in the following sections.

1.1.1 Thermal Induced Martensitic Transformation

Austenite and martensite phases have different crystal structures. In general, while austenite is cubic, martensite can be tetragonal, orthorhombic, and monoclinic. The transformation from one phase to another phase occurs by shear lattice distortion. Figure 1.1 illustrates the temperature-induced phase transformation in the absence and presence of stress. In Figure 1.1a, phase transformations are represented as peaks. The areas under

those peaks indicate the enthalpies or latent heat of transformations. There are four significant temperature points associated with Martensite and Austenite phases. The martensite start (M_s) temperature is one at which the martensite phase begins to form during the cooling process. The martensite finish (M_f) presents the temperature that the transformation from austenite to martensite complete upon cooling. Similarly, the austenite start (A_s) and austenite finish (A_f) temperatures are the ones at which alloy starts to transfer from martensite and complete the transformation to austenite during the heating process, respectively. It is known that the forward transformation (austenite to martensite) is exothermic and the reverse transformation is endothermic reactions. Since the transformations occur without any external stress applied, they are also called zero-stress or stress-free transformation temperatures (TTs). The Differential Scanning Calorimeter (DSC) is the most well-known equipment to determine the latent heat, enthalpy, and TTs.

The thermally induced martensitic transformation is also feasible when SMA component is under stress. If the stress is isothermally applied in austenitic phase (above A_f temperature) and then the material is cooled, the phase transformation will result in detwinned martensite and a shape change will be observed. Complete shape recovery can be achieved by heating the material to a temperature well above the A_f . If the applied stress was enough to trigger the plastic deformation in the material, the full recovery might not be obtained. The TTs are also strongly stress-dependent and they linearly increase with applying higher stresses. Figure 1.1b illustrates the critical point for the transformation determined by using the graphical method. Total strain, ϵ_{total} , was determined by measuring the distance between the cooling and heating portions at M_s , and TTs were determined by the tangent method. Thermal hysteresis, ΔT , was calculated as a temperature difference at

the middle point of total cooling and heating curves. Irrecoverable strain, ϵ_{ir} , is the amount of residual strain that is not recovered at the end of the thermal cycle.

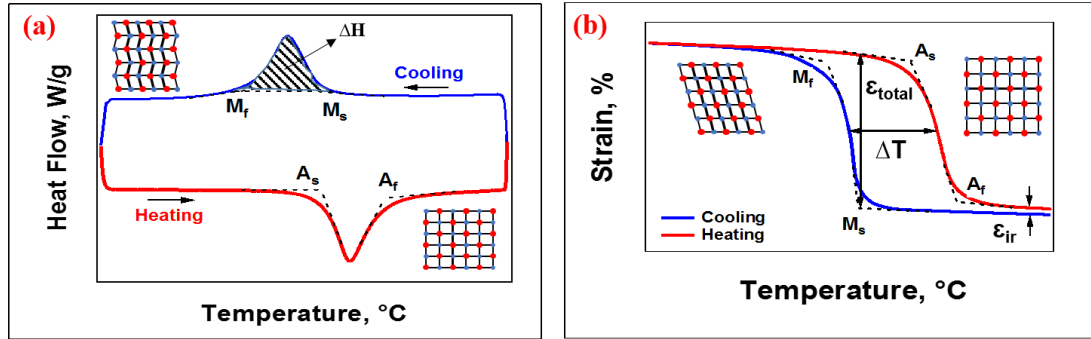


Figure 1.1: Thermal induced phase transformation in the absence (a) and presence (b) of applied stress [9].

1.1.2 Shape Memory Effect (SME)

Martensite re-orientation is stress-induced and the corresponding recoverable strain is associated with the conversion between the martensite variants. Applying stress on an SMA specimen at a temperature below M_f , activates martensite re-orientation process and detwinned martensite variants appear as shown in the first graph of Figure 1.2a. The detwinning process results in a macroscopic shape change. After the load is released, the new configuration is retained. Subsequent heating to a temperature above A_f will result in reverse phase transformation and lead to complete shape recovery (from detwinned martensite to austenite), as shown in the second graph of Figure 1.2a. This process is referred to as the shape memory effect (SME), as illustrated in Figure 1.2b. Cooling back to a temperature below M_f leads to the formation of twinned martensite again. It is worth mentioning that the remained strain might not fully recover by heating up above A_f if the loaded stress is sufficient to introduce plastic deformation, thus irrecoverable strain (ϵ_{ir})

would present after the heating cycle. The total recoverable strain is the combination of elastic (ϵ_{el}) and shape memory effect (ϵ_{sme}) strains.

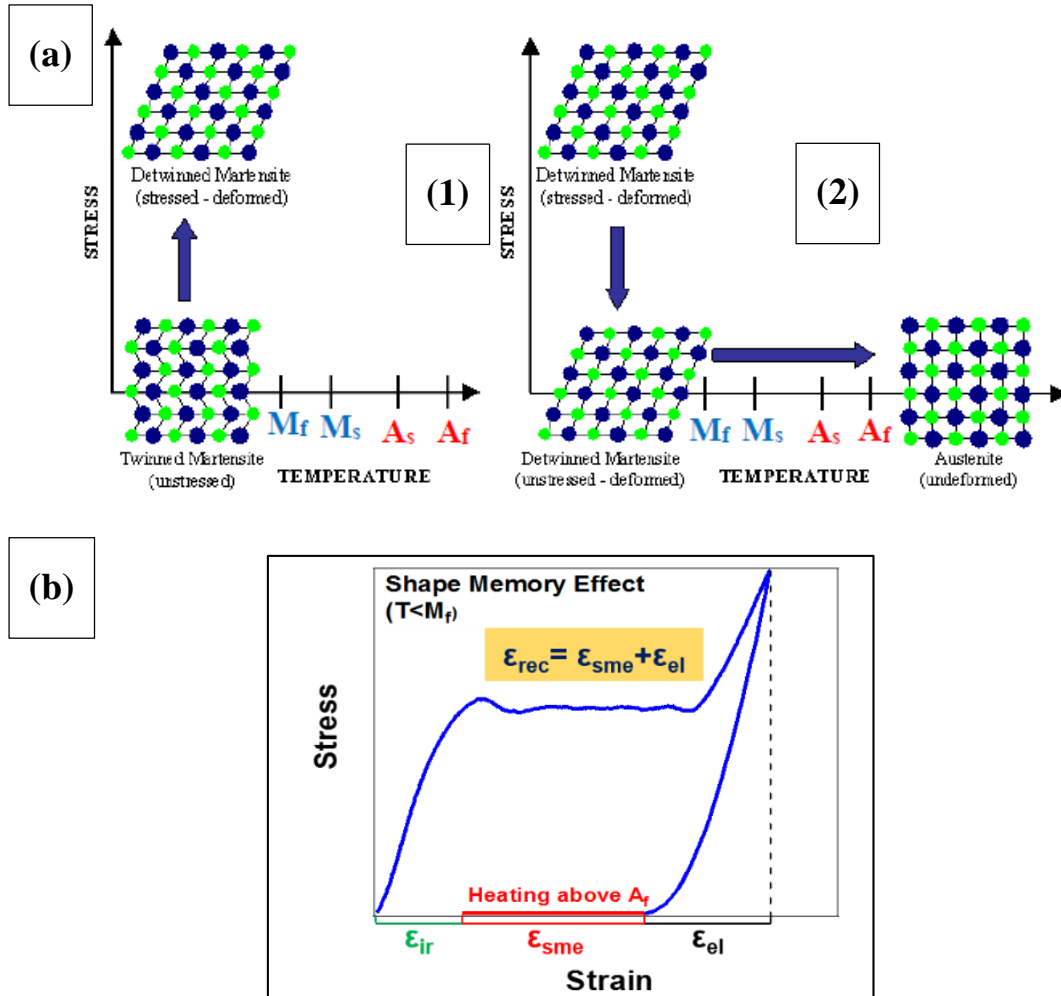


Figure 1.2: Schematic of shape memory effect and superelasticity behavior of SMAs [9].

1.1.3 Superelasticity

SMAs also exhibit stress-induced phase transformation. During loading at temperatures above A_f , stress-induced transformation leads to the formation of detwinned martensite at sufficiently high-stress levels. A complete shape recovery is observed upon unloading due to reverse transformation from martensite to austenite phase. This phenomenon is called superelasticity, represented in the stress-strain curve, as shown in Figure 1.3. After elastic

deformation of austenite, the stress-induced martensite transformation initiated at a critical stress level of σ^{Ms} , and the martensitic transformation end at σ^{Mf} , followed by elastic deformation of martensite phase. Upon unloading, the martensite transforms back to austenite with critical start and end points of σ^{As} and σ^{Af} , respectively, and deformation is ideally recovered. The total amount of superelasticity strain that is recovered upon unloading is symbolized by ϵ_{se} . The stress hysteresis mentioned in the plot depicts the stress difference ($\Delta\delta$) at the midpoint of forward and reverse transformations.

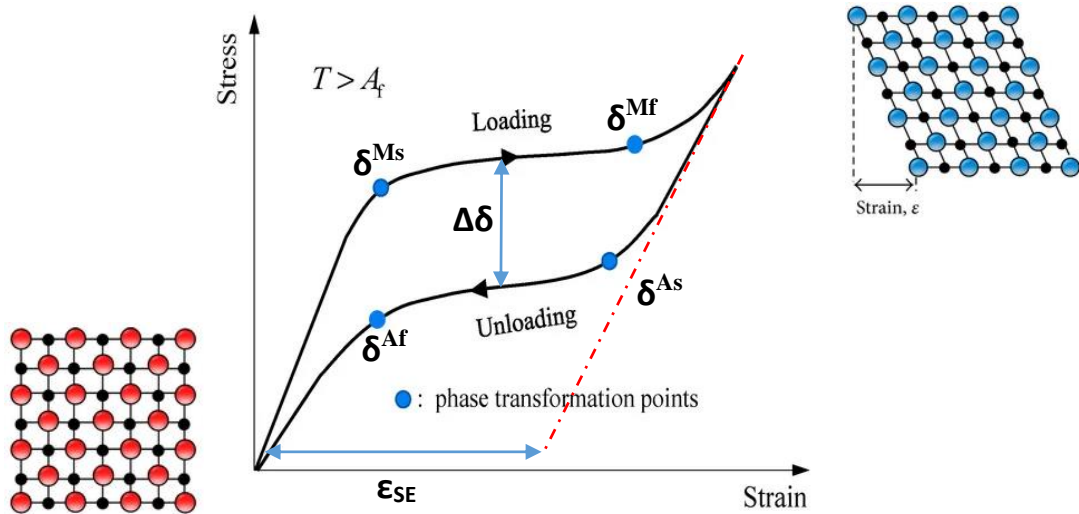


Figure 1.3 Perfect superelastic behavior of SMAs

When alloy temperature is in the range of $(T < M_f)$, the apparent phase is fully martensite. As described in the previous section, under these conditions, if an external stress is applied to the material, firstly, elastic deformation occurs. With further increasing stress, the reorientation of martensite variants starts. If it is unloaded at this point, the shape change caused by the reorientation is retained, and the strain can be recovered to the original shape by heating above A_f . The Stress-Strain curve of SMA specimen at this region can be seen in Figure 1.4a. If the temperature is between M_f and A_s ($M_f < T < A_s$), the stable

phase is either (or both) the martensite or the Austenite, and usually, both phases appear in a sample. With increasing applied stress, detwinning starts at certain stress in the martensite phase of the specimen, and simultaneously, stress-induced martensitic transformation starts in austenite phase region of the specimen. Usually, both transformations occur together and when the whole sample becomes the martensite single-phase, the martensite is stable and does not transform back to the parent phase even if the applied force is removed [10]. Then, the stress-strain curve of SMAs in this temperature region is similar to that at $T < M_f$, as shown in Figure 1.4a.

In the temperature range $A_s < T < A_f$, the deformation induced by the stress-induced martensitic transformation recovers partially upon unloading partial superelasticity and partial shape memory effect by subsequent heating. Superelasticity is observed only when the sample deformed between A_f and M_d ($A_f < T < M_d$) (Figure 1.4b). When the temperature is above the M_d temperature (martensite desist temperature), where stress-induced martensite can no longer be created, the material is then entirely in the austenite plasticity region. At these conditions, the critical stress for plastic strain begins to decrease. After this point, alloys deform like conventional materials, as in figure Figure 1.4c. M_d can be considered the intersection of critical stresses of martensitic transformation and critical stress for slip (plastic deformation). If the material is not strong enough or temperature is close to M_d , partial recovery can be observed since martensitic transformation and plastic deformation occur simultaneously. The specific region (between A_f and M_d) is called superelastic window Figure 1.4d).

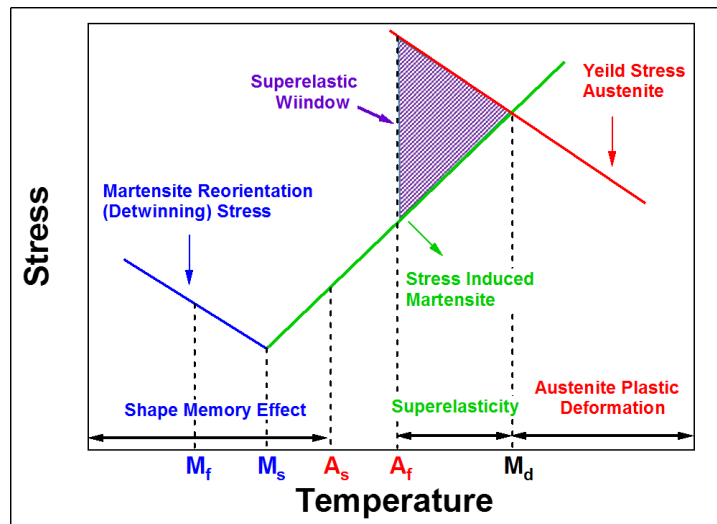
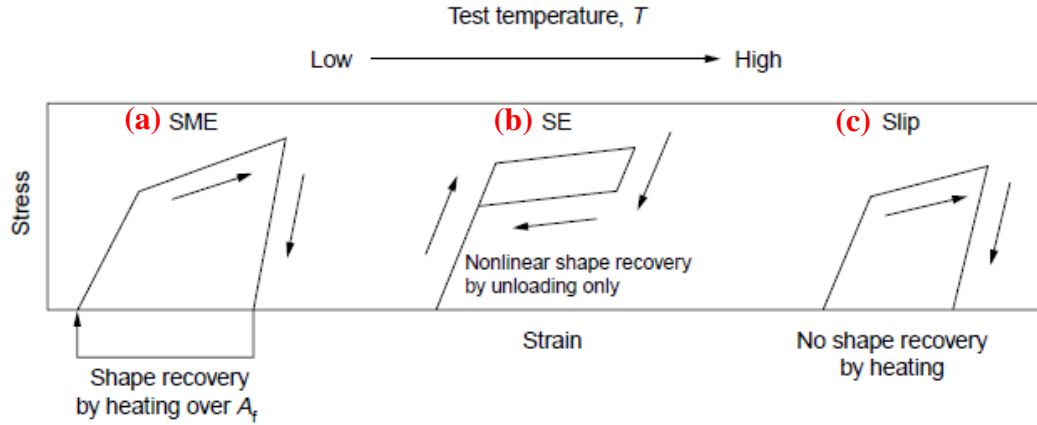


Figure 1.4 Schematic illustration of stress–strain curves of a SMA at three typical temperature regions (a) ($T < M_f$), (b) ($A_f < T < M_d$), (c) ($T > M_d$) [10], and (d) Schematic for the critical stresses of various deformation modes as a function of temperature in SMAs [9]

1.2 Binary NiTi

NiTi SMAs are of great interest due to a combination of unique features, such as superelasticity, shape memory effect, and biocompatibility [11-14]. These unique properties make NiTi a good target for automotive, aerospace, and biomedical industries [13, 15-17]. The structure of high-temperature austenite phase for NiTi is cubic (B2) and the low-temperature martensite phase can be either monoclinic (B19') or orthorhombic (B19). The high-temperature B2 austenite phase transforms directly to monoclinic B19'

upon cooling through martensitic transformation [16]. In some cases in NiTi alloys, B2 austenite could transform to R-phase first followed by R to B19' phase transformation upon cooling. In contrast, the single-step B19' to B2 phase transformation occurs during reverse transformation [18]. R-phase, which has a martensite nature and trigonal lattice, is a transition structure that commonly has rhombohedral structure, low transformation strain, and temperature hysteresis [16]. R-Phase can be formed in NiTi alloys after cold working, aging of Ni-rich alloys, and alloying with a third element such as iron [19]. The formation of R-Phase in NiTi alloys can be due to several reasons such as stress fields around the precipitates, inhomogeneous distribution of precipitates, and the microstructure's inhomogeneity [20-23]. It should be noted that various shape memory properties of NiTi depend highly on the composition [24, 25], heat treatment history [26-30], loading direction (LD) [18–21], crystallographic orientation [31-37], and manufacturing process [12, 38] which will be covered in throw following sections.

1.2.1 Impact of composition on NiTi

Ni content can alter the strength of material and phase transition temperatures can be controlled through the Ni-content [39, 40]. Nitinol is typically composed of approximately 50 to 51 at% nickel. NiTi alloys that contain more than 50.6 at.% nickel are known as Ni-rich NiTi [26]. Figure 1.5 illustrates the dependence of TTs on the composition of NiTi. It is evident from Figure 1.6a that M_s is less sensitive to compositional changes in the Ti-rich side of stoichiometry due to the formation of Ti-rich precipitates (Ti_2Ni) [16]. In contrast, when Ni content increases above 50 at.%, TTs decrease drastically to lower temperatures [39, 41]. TTs of Ni-rich NiTi alloys are very sensitive to the Ni content of the matrix, decreasing about 93 °C/at% [24].

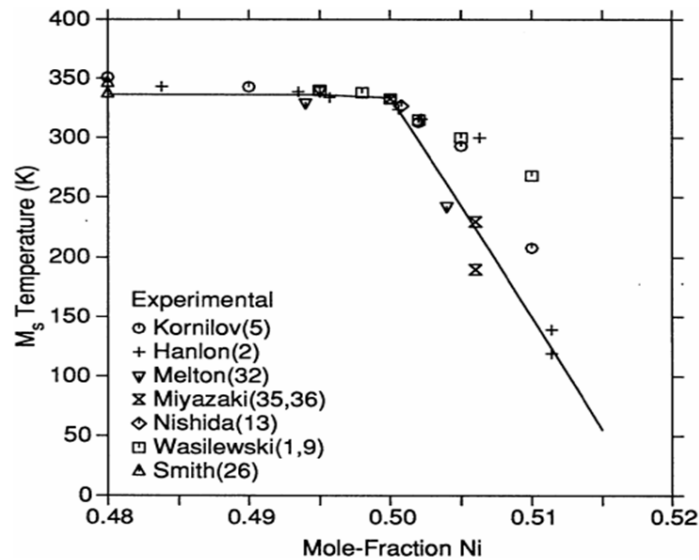


Figure 1.5 M_s temperature as a function of Ni content for NiTi SMAs [42]

Figure 1.6 depicts the tensile behavior of NiTi as a function of composition. The samples with different Ni concentrations were aged at 400 °C and tensile tested at 37 °C. As obvious in this figure, the forward critical stress increases with Ni content due to the decrease of TTs with Ni concentration. As mention previously, the deformation behavior of SMAs depends on TTs and test temperature where SME was observed for the NiTi alloy containing 50 at. % Ni while almost perfect superelasticity was obtained as Ni content increased to 50.9 (atomic %) It has also been reported that the strength of NiTi SMAs improves with increasing Ni content where the austenitic yield stress at room temperature is almost twice higher in Ni_{50.4}Ti (atomic %) compared to Ni_{49.4}Ti (atomic %) [15]. It is worth mentioning that Ni-rich NiTi SMAs are coming into prominence due to their distinct superelasticity and shape memory properties compared to near equiatomic NiTi SMAs that make them an excellent candidate for different applications in biomedical and energy industries [43].

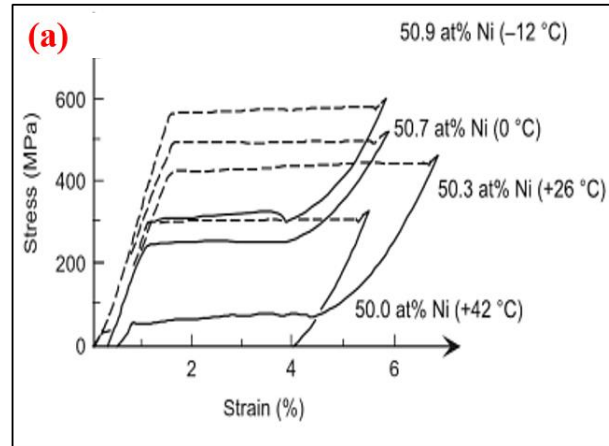


Figure 1.6: Stress vs. strain behavior of NiTi as a function of Ni content [10].

1.2.2 Impact of heat treatment on NiTi

An alternative way to significantly increase NiTi alloys' strength is thermo-mechanical treatments (e.g., cold working and post-annealing) [16]. Aging is one of the most efficient methods to alter the shape memory properties. Even in equiatomic NiTi alloys, even though the matrix is not strong enough to observe perfect superelasticity in the homogenized condition, it is possible to obtain full recovery in superelasticity after proper thermo-mechanical processing [16]. Heat treatments could result in precipitation formation in NiTi SMAs that could control TTs and increase material strength [26, 44]. Nishida et al. reported that the appearance of secondary phases (such as Ni_4Ti_3 , Ni_3Ti_2 , and Ni_3Ti) depends upon aging temperature and time. A lower aging temperature and shorter aging time result in the formation of Ni_4Ti_3 phases, which could be dissolved in the matrix by raising the aging temperature and time, followed by an increase in the number and size of Ni_3Ti_2 precipitates. Furthermore, Ni_3Ti phases appear at higher aging temperatures and longer aging time [45]. The Ni_4Ti_3 metastable precipitates give rise to coherency stress fields [22, 46]. Also, the external stress applied during aging can favor the occurrence of certain Ni_4Ti_3 variants [47,

48]. The transmission electron microscopy (TEM) of Ni_4Ti_3 precipitates after aging are shown in Figure 1.7.

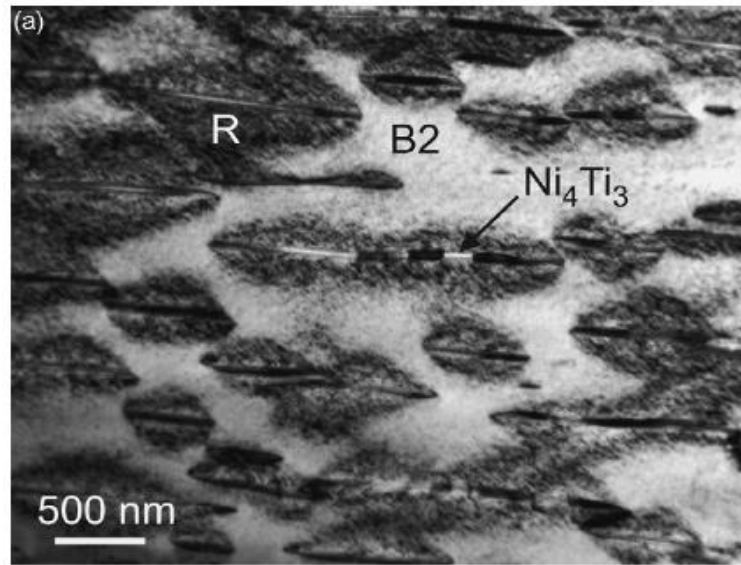


Figure 1.7 TEM micrograph from Ni_4Ti_3 precipitates of aged single crystal NiTi [49]

Generally, the size of precipitates, interparticle distances, and volume fraction of precipitates is a function of aging time and temperatures. Additionally, cooling procedures such as water quenching, oil quenching, air cooling, or furnace cooling could also affect the size and volume fraction of precipitates. However, precipitates' characteristics could change the shape memory and mechanical properties of NiTi in several competing mechanisms. The first mechanism is the chemical effect in which the formation of Ni-rich precipitates deplete the Ni-content of the matrix and thus, increases the TTs [21]. Another mechanism is related to the local stress fields around the precipitates. The TTs will increase when the stress fields are oriented correctly to nucleate the martensite and enough space is provided between particles for nucleation of martensite. However, the stress fields around the fine precipitates with small interparticle distance generate obstacles and resists

nucleation and propagation of martensitic phases. Therefore, this stress field interacts with stress fields of dislocation, resisting plastic deformation, and increasing material strength [50, 51]. Finally, fine precipitates are sheared by dislocation cutting through them, which new interface between precipitates and matrix is produced and increased the interfacial energy; hence, the strength of material improved. In the case of bigger precipitates with longer interparticle distances, dislocations could bypass the precipitates by looping around them instead of cutting through them, diminishing the strength of the alloy [52].

1.2.3 Impact of loading Mode (LD) on NiTi

Moreover, the mechanical behavior of NiTi SMAs depends on the loading mode. It means that tension, compression, and torsion can present different shape memory behaviors. Figure 1.8 shows the tension, shear, and compression behavior of NiTi. The flat stress-plateau (Lüders-like deformation) is observed in tension and torsion but not in compression. Also, the maximum stress is lower than 200 MPa for tension and torsion conditions after 6% deformation while it is ~800 MPa under compression. The asymmetry in the mechanical behavior of SMAs is related to the difference in deformation mechanisms during phase transformation and the martensite morphology. As an example, it is known that variant-variant interaction is more pronounced and detwinning is more difficult under compression, resulting in higher stress-strain slope during transformation and lower transformation strain. Furthermore, observed twinning types can also be different. It is important to note that the most common twinning type observes in NiTi alloys is $\langle 011 \rangle$ type II [53]. It has been reported that the twinning type can be a mixture of type I and type II while a combination of type I and $\langle 001 \rangle$ compound twins were also obtained after proper cold rolling [54].

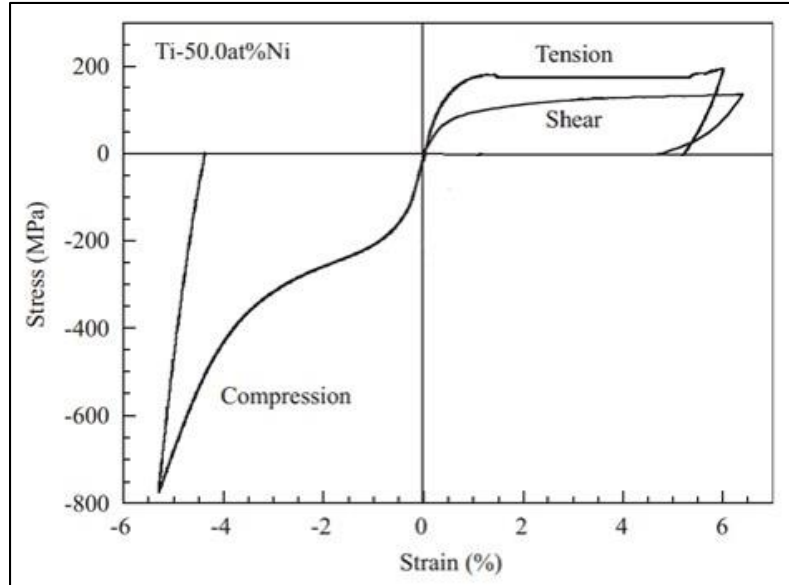


Figure 1.8 Deformation behavior of NiTi SMAs under tensile, compressive, and shear stress [55].

1.2.4 Impact of Crystallographic orientation on NiTi

The shape memory and mechanical properties (e.g., transformation strain, hysteresis, superelasticity window, CC slope, ductility) of NiTi-based SMAs are highly crystallographic orientation-dependent [29, 32, 56-59]. The stress-strain responses of aged $\text{Ni}_{50.8}\text{Ti}_{49.2}$ alloys as a function of crystallographic orientation in compression are demonstrated in Figure 1.9. The highest recoverable compressive strain, about 9%, was obtained along with [148] orientation while it was 8%, 4.8%, and 3% along the [001], [112], and [111] orientations, respectively. It is obvious that [111] and [112]-oriented single crystals exhibit steep stress-strain slope during the martensitic transformation due to the formation of multiple correspondent variant pairs (CVPs) while [001] and [148]-oriented single crystals present plateau-like behavior. The orientation step slope in the plateau region quickly passed the critical stress for plastic deformation; therefore, their transformation strain and superelastic temperature window are limited [57, 59]. In addition,

the CC slopes of aged $\text{Ni}_{51.5}\text{Ti}_{48.5}$ are 9.3 and 7.5 MPa/ °C for [111] and [110] orientations [59], respectively, while for equiatomic NiTi polycrystalline alloys are approximately 12 MPa/ °C in compression [60] and 5–8 MPa/ °C in tension [61].

In single-crystal alloys, it is possible to calculate the *resolved shear stress factor* (RSSF) for each variant based on the orientation relationship between the direction of a particular habit plane and the applied stress. RSSF and the maximum experimental recoverable strain for the $\langle 011 \rangle_{\text{B19}'}$ type II twin, which is the dominant twinning mode observed in martensite plates [62], are summarized in

Table 1.1. larger RSSF value belongs to more active/favorite variants, which present higher transformation strain under low-stress levels in stress-induced martensitic transformation. For instance, in NiTi, the [001] has lower critical stress and larger recoverable strain compared to [111] orientation under compressive load (Figure 1.9) where the RSSF values are about 0.4 and 0.27 for [001] and [111] orientations, respectively [59]. Based on the literature [58, 63, 64], [111]-oriented NiTi alloys demonstrated enormous transformation strain and low critical stress, while the [001]-oriented NiTi presented lower transformation strain and at significantly higher stress levels in tensile condition. Thus, the favorite martensite variants for tensile and compressive are [111] and [001], respectively, and have a different degree of martensite detwinning, leading to remarkably present different shape memory behaviors.

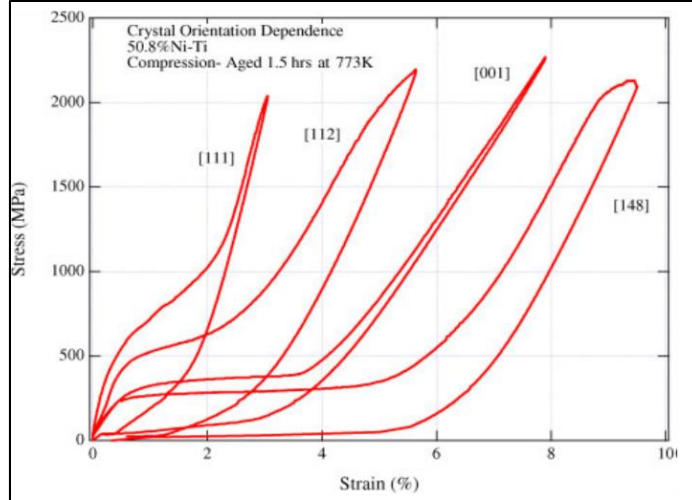


Figure 1.9: (a) Superelastic behavior of NiTi SMA as a function of the crystallographic orientation [25].

Table 1.1: RSSF and Maximum experimental strain of NiTi under tension and compression [9].

NiTi <011> type II				
Compression			Tension	
	RSSF	$\epsilon_{\text{experimental}}$	RSSF	$\epsilon_{\text{experimental}}$
[001]	0.40	> 5%	0.21	> 2%
[011]	0.37	> 4%	0.41	$\geq 6.5\%$
[111]	0.27	$\geq 3\%$	0.39	> 7.5%
polycrystalline		> 3%		$\geq 5.5\%$

It is reasonable to expect that the shape memory and superelastic behavior of SMAs depend on the orientation distribution of the grains in the material, which knows as texture. Texture can be introduced by thermomechanical processing, such as cold rolling or equal

channel extrusion. The specimen can also be cut at certain angles to present a strong texture close to an orientation that exhibits the best shape memory and material properties. Additionally, polycrystalline SMAs with strong texture in a particular orientation would be expected to have similar behavior as a single crystal alloy. It should be noted that the shape memory properties of SMAs could be optimized by texturing in polycrystalline materials. It has been reported that the tense texture in cold-rolled NiTi is along the [110] orientation [63, 65].

1.3 NiTi Fabrication

Production of SMA components conventionally entails arc or induction melting followed by a hot working process and machining to the final shape [66]. To minimize the possibility of contamination during melting, an inert gas working atmosphere is used [12]. However, machining of NiTi is challenging [12] and the significant heat generation throughout a machining process can affect the functional properties of fabricated parts [67, 68]. Besides, conventional processing routes do not allow for NiTi production in complex geometries; therefore, most NiTi devices are made in the form of simple geometries, such as wire, sheet, tube, and bar [69]. Most conventional methods lack homogeneous control of porosity (e.g., amount of porosity, pore size, pores' arrangement, and interconnection of pores), chemistry (impurity content, homogeneity, intermetallic), geometric flexibility, and freeform design. The formation of secondary phases in elemental powder usage is unavoidable since their appearance is much more favorable thermodynamically compared to NiTi formation [70]. Undesirable secondary phases and contamination do not only affect mechanical properties, but they also make the foam brittle and additionally change phase TTs, which are essential for practical applications[70].

Additive Manufacturing (AM) is another method that has attracted significant attention for overcoming the mentioned problems in the fabrication of NiTi alloys. AM technologies include selective laser melting (SLM) and selective laser sintering (SLS), laser engineered net shaping (LENS), and electron beam melting (EBM). Generally, the term AM describes processes used to create physical parts directly from CAD data by adding material in successive layers [69]. L-PBF process, which is the most common AM process, is operated by a computer-aided design (CAD), in which a focused laser beam melts the deposited powder layer locally. The melting is followed by rapid solidification and a subsequent layer is melted likewise and merged to the former layer. The process continues until the CAD-defined design 3-D part is created. Figure 1.10 schematically describes the AM process for fabrication porous NiTi.

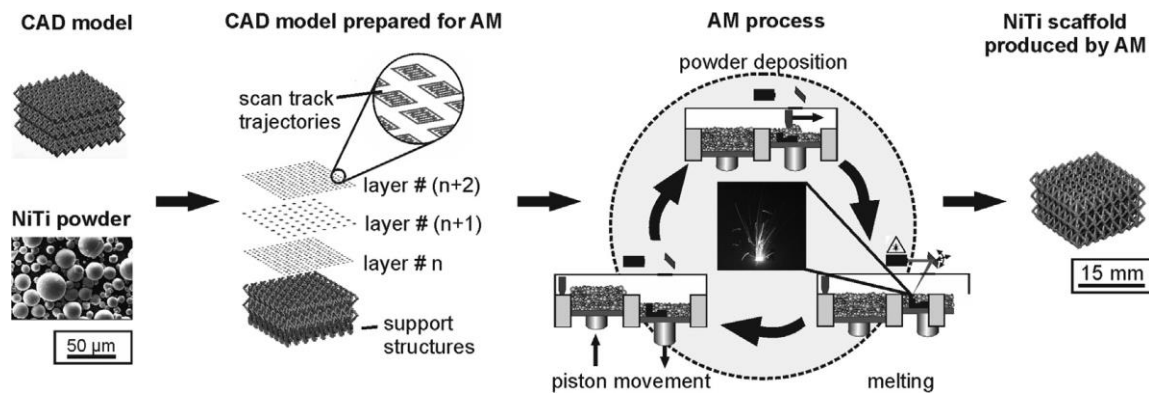


Figure 1.10 Schematic showing the principle of powder bed-based AM of complex NiTi scaffolds [69]

1.4 L-PBF-AM NiTi

L-PBF is one of the most common AM methods to fabricate near net-shape metallic materials and the flexibility of this fabrication method makes it one of the most promising production method for patient-specific medical devices [69, 71-73]. Laser Powder Bed Fusion Additive Manufacturing (L-PBF-AM) is an effective method to create highly

complex Ni-Ti geometries with pre-designed porosity, homogeneous composition, and desirable properties compared to the traditional techniques [74]. This process can result in structures with high density, near net shape, tailorable shape memory properties, eliminating the requirement of post-processing. This new fabrication method is also known as 4D printing, where produced SMA components can respond in an anticipated manner to external stimuli from the environment or through human intervention, leading to a change in shape or physical properties over time.

One of the L-PBF-AM challenges is finding the right process window and the related interaction mechanism between PPs. Parameters such as volumetric energy density, $E_v = P/v \cdot h \cdot t$, and linear energy density, $E_l = P/v$ (P: power of laser beam, h: hatch spacing v: scanning speed, t: layer thickness), are generally used to correlate the processing parameters to shape memory and material properties of L-PBF-AM fabricated samples. To date, many studies have investigated the optimum PPs as well as building direction (BD) and scanning strategy to manufacture different materials, including steels, copper components, and superalloys by AM methods. Distinct PPs have been reported for different materials. For example, an energy density window of 44.4 to 50.8 J/mm³ has been reported for L-PBF-AM AlSi10Mg [75, 76]. Li et al. observed higher porosity, smaller molten pool size, and eventually lowers the tensile strength of 316 stainless steel by increasing scanning speed [77]. By evaluating a range of L-PBF-AM PPs to fabricate Co–29Cr–6Mo, it was reported that applying energy density more than 400 J/mm³ dense L-PBF-AM alloy can be obtained while employing energy density lower than 150 J/mm³ leads to the formation of porous [78]. Vanderbroucke et al. reported that 162-293 J/mm³ energy density could produce more than 99% dense Ti6Al4V L-PBF-AM parts [79]. Moreover, the

microstructure features such as grain size, porosity, melt pool, secondary phases, texture, composition, etc., are all altered with employed parameters during the fabrication of L-PBF-AM components. For NiTi alloys, TTs are also changed due to their sensitivity to the composition. L-PBF-AM NiTi-based superalloys have also been subjected to some studies. NiTi SMAs are of great interest due to a combination of unique features, such as superelasticity, shape memory effect, and biocompatibility [11-14]. Due to the difficulties with machining and forming NiTi components, the ability to fabricate complex NiTi parts by using L-PBF-AM technique has dramatically increased their potential applications [80-84]. It is well-known that microstructure features such as grain size and average diameter are crucial for toughness, strength, and resistance to crack initiation [85, 86]. It was reported that TTs and mechanical response of L-PBF-AM NiTi greatly influenced by altering PPs [87-89]. By considering different PPs, Bormann et al. has focused on grain size, shape, and texture of L-PBF-AM NiTi and documented the tailorable microstructure via L-PBF-AM PPs [85, 90, 91]. Effects of process parameters also studied on geometrical characteristics of porous L-PBF-AM NiTi [92]. For NiTi, it has been reported that 100-200 J/mm³ energy input is required to have dense SLN NiTi [93, 94]. It has been shown that the higher energy samples show higher strength; however, the impurity level of L-PBF-AM NiTi samples is also increased with energy level [88, 93, 94]. Furthermore, it was documented that laser power and scanning speed should increase or decrease along with each other to retain the density of the NiTi parts [87].

In general, the heat flow during AM, competitive growth mechanisms, and epitaxial growth due to partial remelting of the previous layer results in the formation of long elongated grains with a preferential crystal orientation along the BD [95-98]. In many

studies on the L-PBF-AM method [95, 97, 99-101], the as-fabricated specimens presented columnar grain architecture parallel to the sample BD. This is in response to the maximum heat flow, which usually occurs through the sample thickness in the BD. However, it was shown that the texture in some BCC alloys (e.g., Tungsten) could be altered from typical [100] to [111] orientation with the change in processing parameters and thus the melt pool shape [102].

The shape memory and mechanical properties (e.g., transformation strain, hysteresis, superelasticity window) of NiTi-based SMAs are highly crystallographic orientation-dependent [29, 32, 56]. [100]-oriented NiTi single crystals show improved superelastic behavior since slip deformation is minimized due to the lack of available slip systems in B2 austenite, but the tensile transformation strain along the [100] orientation is limited compared to [111] orientation [29, 32]. Thus, it is essential to be able to tailor the texture of L-PBF-AM fabricated to alter the shape memory properties. In our previous study, the effects of hatch spacing on the thermomechanical properties of the L-PBF-AM NiTi parts with the laser power of 250 W were examined [103], and it was found samples fabricated with lower hatch spacing showed strong [100]-texture along the BD and dramatically enhanced superelastic response. We also reported that when the laser power was decreased from 250 W to 100 W with the hatch spacing of 120 μm , samples demonstrated higher strain recovery and lower mechanical hysteresis [104].

1.5 Motivation and Statement of Problem

SMAs, particularly Nickel-Titanium alloys (i.e., NiTi or Nitinol), are well known for their unique shape-memory effect and superelasticity behaviors, whereby large

deformations up to 8% can recover through reversible phase transformations [105, 106]. In addition to these two intrinsic behaviors, NiTi alloys represent other favorable characteristics, such as low stiffness (i.e., Modulus of elasticity, or Young's Modulus), biocompatibility, high damping capacity, and adequate corrosion resistance [80]. These, altogether, make NiTi alloys superior candidates for a wide range of applications, such as aerospace, medical, and military systems [13, 107, 108]. Additionally, recently elasto (magneto) caloric materials that undergo large reversible solid to solid phase transformation to exhibit adiabatic temperature change or isothermal entropy change induced by an external field (such as magnetic, uniaxial, or isotropic stress and electric fields) are introduced as promising candidates for the next generation of the vapor-compression cooling systems [109]. In recent years, most studies in elastocaloric materials are focused on the SMAs which exhibit large latent heat during stress-induced reversible martensitic transformation [110-113]. It should be noted that materials with large surfaces, porosity, and different size and shape can be more suitable to improve the heat transfer and enhance cooling performance [114, 115]

Despite the great interest in NiTi SMAs, due to their high reactivity and high ductility [68, 116, 117], their applications have been limited to simple geometries, such as rod, wire, bar, tube, sheet, and strip [116]. Hence, the fabrication of complex NiTi geometries using conventional fabrication techniques used to be costly, time-consuming, imprecise, and, most often, impossible. In recent years, thanks to AM techniques, complex shapes of alloys (e.g., patient-specific implants, porous structures, curved surfaces) have been realized [17, 82, 118]. AM techniques are either powder-bed based (e.g., SLM) or flow-based (e.g., LENS). In literature, powder-bed-based techniques have attracted the most attention for

creating complex NiTi-based parts [119-121] while the flow-based techniques have only been implemented in a small number of studies [122-124]. This is because realizing the final shape with flow-based methods is often difficult without post-fabrication processing, such as machining.

However, the structural and functional properties of NiTi are highly fabrication and process parameter dependent. Therefore, each step in the fabrication of NiTi parts requires a deep understanding of its impact on the final product's quality and performance. During the L-PBF-AM process, parameters such as laser power, powder layer thickness, scanning speed, hatch spacing, building orientation, and scanning strategy are all involved. The flexibility of these PPs in L-PBF-AM method can be employed to tailor notable features of NiTi compounds such as TTs, microstructure, texture, and consequently the mechanical response. Also, the influence of post-processing heat treatments on NiTi alloys fabricated through L-PBF-AM process requires more detailed studies to reveal the effects of aging on the quality and performance of the final product. Therefore, a comprehensive and systematic study is needed to gain an in-depth understanding of the relationship between the AM process, microstructure, and shape memory properties to be able to engineer the shape memory properties of laser manufactured NiTi components.

1.6 Technical Approach and Objectives

In this study, first, the influence of a wide range of fabrication parameters such as laser power and hatch spacing on TTs, microstructure, texture, and the mechanical response have been investigated to determine the optimum PPs to observe superelasticity. Then, dog-bone tensile and rectangular compressive of $\text{Ni}_{50.8}\text{Ti}_{49.2}$ specimens were additively manufactured using the selected PPs to evaluate the impact of sample orientation. Finally, the effects of post-

processing heat treatments were investigated on the L-PBF-AM NiTi alloys fabricated with selected PPs and compared with the reference ingot. Five types of thermomechanical experiments were performed; i) failure tests: to examine ductility, yield strength, and critical stresses of the samples, ii) thermal cycling under stress tests: to determine the thermal hysteresis, transformation strain, strength, and work output of material, which are the main factors for actuator applications, as a function of applied stress, iii) cyclic shape memory effect tests: to observe the cyclic stability of samples, iv) isothermal stress-strain experiment: to investigate the critical stress for phase transformation (or variant reorientation), strain recovery or superelasticity, stress hysteresis and Young's modulus of transforming phases as functions of temperature, and v) isothermal cyclic loading/unloading: to observe the stability of superelastic response. The thermal and stress cycling results were used to determine the phase diagram with Clausius- Clapeyron (CC) slope. Considering applications, special attention was given to superelastic response of the parts at room and body temperatures. The microstructure and texture of L-PBF-AM fabricated NiTi alloys were analyzed and their correlation to the mechanical results was addressed. The following are the objectives of this study:

- Investigate the effects of L-PBF-AM PPs, such as laser power, hatch spacing, and building orientation, on the TTs, microstructure, and mechanical response of Ni-rich NiTi.
- Characterize the shape memory behavior of Ni-rich NiTi SMAs fabricated by L-PBF-AM under compression and tension as functions of stress and temperature.
- Reveal the texture and the shape memory response of NiTi alloys fabricated along with the selected directions relative to the building direction.

- Reveal the functional and structural differences between conventionally fabricated Ni-rich NiTi and L-PBF-AM NiTi
- Study the effects of post-processing aging on shape memory response of as-fabricated Ni-rich L-PBF-AM and conventional NiTi.

2 Experimental Procedure

This chapter aims to describe details on the fabrication and processing of the materials as well as the experimental methods used in the characterization of L-PBF-AM fabricated NiTi alloys throughout this study. The details of material preparation, calorimetric measurements, mechanical testing, and microstructural analysis will be presented throughout the chapter. This work has been conducted with the collaboration of University of Toledo and University of Kentucky. Fabrication of NiTi specimens was performed at Dynamic and Smart Systems Laboratory at the department of Mechanical Industrial and Manufacturing Engineering of the University of Toledo.

2.1 Materials Fabrication

Ni_{50.8}Ti_{49.2} (atomic %) ingots produced by casting obtained from (Nitinol Devices & Components, Inc. Fremont, CA) were atomized to powder by TLS Technik GmbH (Bitterfeld Germany) using an electrode induction melting gas atomization (EIGA) technique. L-PBF-AM NiTi samples were fabricated using Phenix system PXM model, which is a L-PBF, SLM machine (Figure 2.1). Before fabrication, a 3D CAD model is drawn and imported into the Phenix system specialist software, where the CAD design is sliced into the requisite layers. Next, PPs such as laser power, scanning speed, scanning space, etc., are defined. The system equipped with a 300 W Ytterbium fiber laser was employed for the selective laser melting. The laser's beam quality is M₂ <1:2, the beam profile is Gaussian (TEM₀₀), and the beam diameter is approximately 80 mm. The machine uses a metal scraper and roller to create the powder layer. The process starts when the feeding piston moves upward and provides the powder. Then, the scraper collects the powder from the feeding piston, and the roller deposits it on the building platform. Next, the laser selectively scans and melts the

powder according to the geometry requirements of the part provided by the machine control software.



Figure 2.1 Phenix PXM Selective Laser Melting system [125].

2.2 Materials Preparation

The L-PBF-AM fabricated parts were separated from the base plate using electrical discharge machining (EDM). Also, small pieces were cut to determine the TTs of the material and microstructure analysis using EDM. Figure 2.2 shows the employed KNUTH smart EDM. EDM is a manufacturing process whereby a desired shape is obtained using electrical sparks.



Figure 2.2 Electrical Discharge Machining (EDM) [125].

2.3 Heat Treatments

samples were aged at 550°C for 1.5 hr. Aged samples were quenched in water at room temperature right after aging. The aging process was conducted using a Whip Mix Pro Press 200 dental furnace (Figure 2.3). The furnace has been equipped with a Vacuum Pump.



Figure 2.3 Whip Mix Pro 200 dental furnace [125].

2.4 Calorimetry Measurements

Stress-free phase TTs (martensite finish, M_f ; martensite start, M_s ; austenite start, A_s ; and austenite finish, A_f) were measured using a Perkin-Elmer Pyris 1 differential scanning calorimeter (DSC) as shown in Figure 2.4. The typical temperature range is from -60 to 600 °C and the heating/cooling rate was kept at 10 °C/min in a nitrogen atmosphere. The temperature scale is calibrated using a two-point (or more) calibration method where the onset temperatures for the melting points of high purity Indium and Zinc standard provided by Perkin Elmer were measured. Also, the furnace was calibrated by using the furnace calibration feature in Pyris software.

Sample preparation significantly affects the measured TTs due to residual stresses developed in a sample during the preparation process. Sample must be polished to establish good thermal contact with the bottom of the pan and its weight should be in the range of 20-40 milligrams. Both the sample weight and heating rate affect the DSC response. Increasing the sample weight and/or heating rate increases the temperature gradients in the sample, resulting in decreased signal quality and resolution.

The basic principle of the DSC operation is the measurement of the rate at which heat energy is supplied to the specimen compared to reference material to maintain a constant temperature rate [126]. The sample is thermally cycled and the difference of the provided heat power is recorded as showed in Figure 1.1a. The net amount of heat released (ΔH) during phase transformation was calculated from the area under the transformation peaks. The TTs are measured as the intersection of the baseline and the maximum gradient

line of a transformation peak. The martensite peak (M_p) and austenite peak (A_p) were measured as the points in the transformation for which the slope of the curve is equal to zero. Besides, thermal hysteresis was determined as the difference between the A_p and M_p ($\Delta H = A_p - M_p$).



Figure 2.4: Pyris I DSC to measure the stress-free phase TTs [125].

2.5 Microstructural Analysis

For polishing, the first samples mounted using Epoxy Resin and hardener. BUEHLER EcoMet/AutoMet 250 Grinder-Polisher was used, which is shown in Figure 2.5. The grinding procedure involves several stages, using a finer paper for each successive step. For polishing, diamond suspensions of $9\mu\text{m}$, $6\mu\text{m}$, and $3\mu\text{m}$ are used. Finally, alumina suspensions of $1\mu\text{m}$ and $0.5\mu\text{m}$ were used to produce a smooth surface.



Figure 2.5 BUEHLER EcoMet/AutoMet250 Grinder-Polisher [125].

Keyence VH_Z250R Optical Microscopy was used to determine the martensite morphology, grain size, and second phase formation. The equipment can be seen in Figure 2.6. Samples were also etched to reveal the microstructure of the metal through a selective chemical solution. The H_2O (82.7%) + HNO_3 (14.1%) + HF (3.2%) solution was used as etchant.



Figure 2.6 Keyence VH_Z250R Optical Microscopy [125].

In collaboration with the University of New Mexico, a JEOL 2010F transmission electron microscope (TEM) operating at 200KV, attached with a HAADF detector for Z-contrast imaging (S/TEM), was used to characterize the microstructure of aged L-PBF-AM and ingot NiTi. Cross-section TEM foils were prepared using a Thermo Fisher Helios Nanolab 650 dual beam focused-ion-beam (FIB) microscope. The aspect ratio and area fraction of precipitates were calculated using Image J software. Multiple TEM images were considered for the precipitate analyses for better statistics. Additionally, Orientation imaging (OI) was done using an FEI Apreo scanning electron microscope (SEM) at 30KV with an EDAX Hikari Super EBSD camera in collaboration with Ohio State University (chapter 3) and the Institute of Condensed Matter Chemistry and Technologies for Energy (chapter 4).

2.6 Mechanical Testing

The thermo-mechanical experiments were conducted using an MTS Landmark servo-hydraulic test frame with custom compression/tension grips shown in Figure 2.7. The applied force was measured by a 100 kN capable load cell and the axial strain was measured by an MTS high-temperature extensometer with a gauge length of 12 mm. Heating of the sample was achieved by conduction through the compression/tension plates at a rate of 10 °C/min and liquid nitrogen fellow through copper coils wrapped around the grips to cool the system at a rate of 5 °C/min. A PID driven Omega CN8200 series temperature controller ensured stable heating/cooling rates with K-type thermocouples attached to both the specimen and grips. A cryogenic grade, on/off solenoid valve commanded by the temperature controller was used to control liquid nitrogen flow. The experimental setup allowed testing of a sample in compression or tension at a temperature

range between -100 to 600 °C. This setup enabled mechanical characterization of a sample in austenite and martensite phases (stress-strain test) as well as thermal cycling under selected stress levels.

The compression/tension sample was polished mechanical with a 600 grit paper to remove the surface residue left after being cut by EDM. A K-type thermocouple was attached to the sample and the specimen was placed between the test setup in a proper position. Unless indicated, otherwise the rate of 8×10^{-4} mm/sec for loading and 100 N/sec for unloading was used in mechanical tests.



Figure 2.7 MTS Landmark servo-hydraulic test platform.

3 Impact of L-PBF-AM Process Parameters (PPs)

In this chapter, a very comprehensive and systematic study is conducted to understand the relationship between the AM PPs, microstructure, and shape memory properties. This study is an effort to complement our previous efforts [103, 104, 127, 128] to understand the effects of L-PBF-AM PPs on the texture and shape memory behavior of NiTi when they are fabricated with lower laser power levels of 50 and 100 W.

3.1 Fabrication

Cylindrical specimens with 10 mm in height and 4.5 mm in diameter were fabricated by alternating XY scanning strategy. Table 3.1 summarizes the processing parameters used in the L-PBF-AM fabrication of NiTi samples. The hatch spacing was varied from 40 μm to 240 μm , combined with two laser powers; 100 W (Group A) and 50 W (Group B). The laser scanning speed was kept constant at 125 mm/s. Corresponding volumetric and linear energy densities were calculated for each set of processing parameters and reported in this table. The linear energy density of group A samples is twice the linear energy density of Group B samples.

Table 3.1 List of L-PBF-AM fabrication parameters concerning effect of hatch spacing and laser power

	Sample	P (W)	v (mm/s)	H (μm)	E_v (J/mm^3)	E_l (J/mm)
GROUP A	A1	100	125	40	666.7	0.8
	A2	100	125	80	333.3	0.8
	A3	100	125	120	222.2	0.8
	A4	100	125	160	166.7	0.8
	A5	100	125	200	133.3	0.8
	A6	100	125	240	111.1	0.8
GROUP B	B1	50	125	40	333.3	0.4
	B2	50	125	80	166.7	0.4
	B3	50	125	120	111.1	0.4
	B4	50	125	160	83.3	0.4
	Fabrication Failed	50	125	200	66.7	0.4
	Fabrication Failed	50	125	240	55.6	0.4

3.2 Microstructure

The rapid cooling and solidification of melted powder during L-PBF-AM process affects the size and shape of the melt pool [129], demonstrating a significant impact on the microstructure and grain growth of the fabricated samples [130]. Figure 3.1 shows the optical micrographs of Group A samples. A1 has a homogeneous microstructure with visible arc-shaped melt pool boundaries and irregularly shaped grains. Black spots observed in the optical images are pores. The scattered and irregular shaped grains combined with sharper melt pool boundaries were observed when the hatch spacing increased to 80 μm in A2. Similar but larger irregular shaped grains were observed in A3 with hatch spacing of 120 μm . In A4, grain shape was changed to “S-shape” previously observed in L-PBF-AM NiTi due to the thermal gradient in the centerline of the melt pool and the overlap of the adjacent melt pools [85, 104]. In A5, the grains' shape was square

where their width corresponds to the hatch spacing due to the employed alternating XY scanning strategy. Specimen A6 showed faint melt pool boundaries and larger pores.

Most of the pores in samples fabricated with smaller hatch spacing are small and spherical (showed by red circles in the figures); thus, their formation can be attributed to gas entrapment or Ni evaporation [129, 131, 132]. When the micrographs for specimens A1 to A6 are compared, it can be concluded that increasing the hatch spacing increases the size and volume fraction of the voids. The increase in porosity with increased hatch spacing (or decreased volumetric energy density) is due to reduced overlap between the adjacent melt pools resulting in reduced fabrication temperature [133] and increased cooling rate. When the solidification happens faster, the shielding gases are trapped to result in voids [134].

Figure 3.1 shows the distance between two adjacent melt pool boundaries as blue arrows corresponding to the implemented hatch space. Previous studies have shown that the melt pool's width and depth depend on the size of the laser beam, laser power, and scanning speed but are independent of hatch spacing [133, 134]. However, if the employed hatch space is larger than the melt pool width, the adjacent tracks will not connect and consequently, aligned pores will be formed between the scan tracks [135]. Thus, to avoid a failure in the fabrication process, the hatch space should not be larger than the melt pool width. Since the melt pools of A6 are overlapped, it is concluded that the melt pool width was larger than 240 μm for all the samples in Group A. However, it should be noted that the overlap distance significantly affects the cooling rates and this the shape and the texture of the grains.

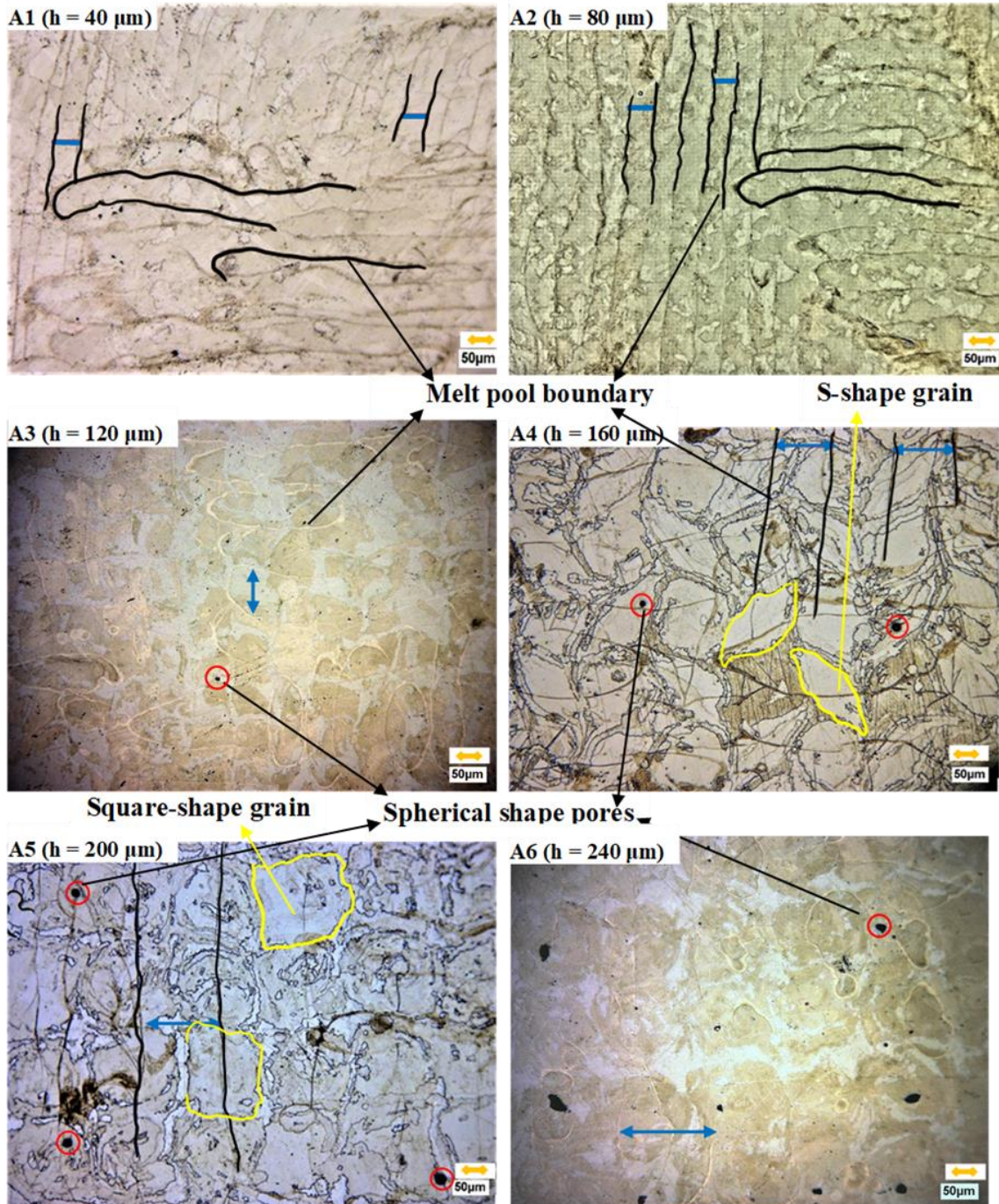


Figure 3.1 BD optical micrographs of L-PBF-AM-fabricated $\text{Ni}_{50.8}\text{Ti}_{49.2}$ samples produced at 100 W and various hatch spacings: A1 (40 μm), A2 (80 μm), A3 (120 μm), A4 (160 μm), A5 (200 μm), A6 (240 μm).

Figure 3.2 shows the optical micrographs of Group B. As indicated in Table 1, fabrication of the samples with the two largest hatch spacings of 200 and 240 μm was failed. The failure could be attributed to the low laser power combined with large hatch

spacing resulting in very low volumetric energy density and an unstable melt pool or lack of fusion between adjacent melt pools [129, 131]. Thus, it can also be concluded that the melt pool width was less than 200 μm when the linear energy is 0.4 J/mm. Similar to Group A, the number of pores in Group B increased with hatch spacing and decreased with volumetric energy density. At this laser power ($P = 50 \text{ W}$), most of the pores had irregular shapes (red rectangles) and they were observed even at the smallest hatch spacing of 40 μm and highest volumetric energy density of 333.3 J/mm³.

It should be noted that while the microstructures are considerably different, the pairs of A2-B1, A4-B2, and A6-B3 were fabricated with the same volumetric energy density. Higher porosity was observed in group B samples, which could be attributed to the melt pool size. The volumetric energy density of A2-B1 pair is 333.3 J/mm³ and both samples are almost pore-free and thus almost fully dense. When the volumetric energy density is decreased to 111.1 J/mm³ for the A6-B3 pair, A6 is still pore-free, while a high amount of pore formation was observed for B3. Thus, we can conclude that volumetric energy density is not the only parameter to ensure successful fabrication of dense materials. By decreasing the laser power from 100 W to 50 W, the melt pool's size decreases and, consequently, the track lines become discontinuous, and pores are formed [136].

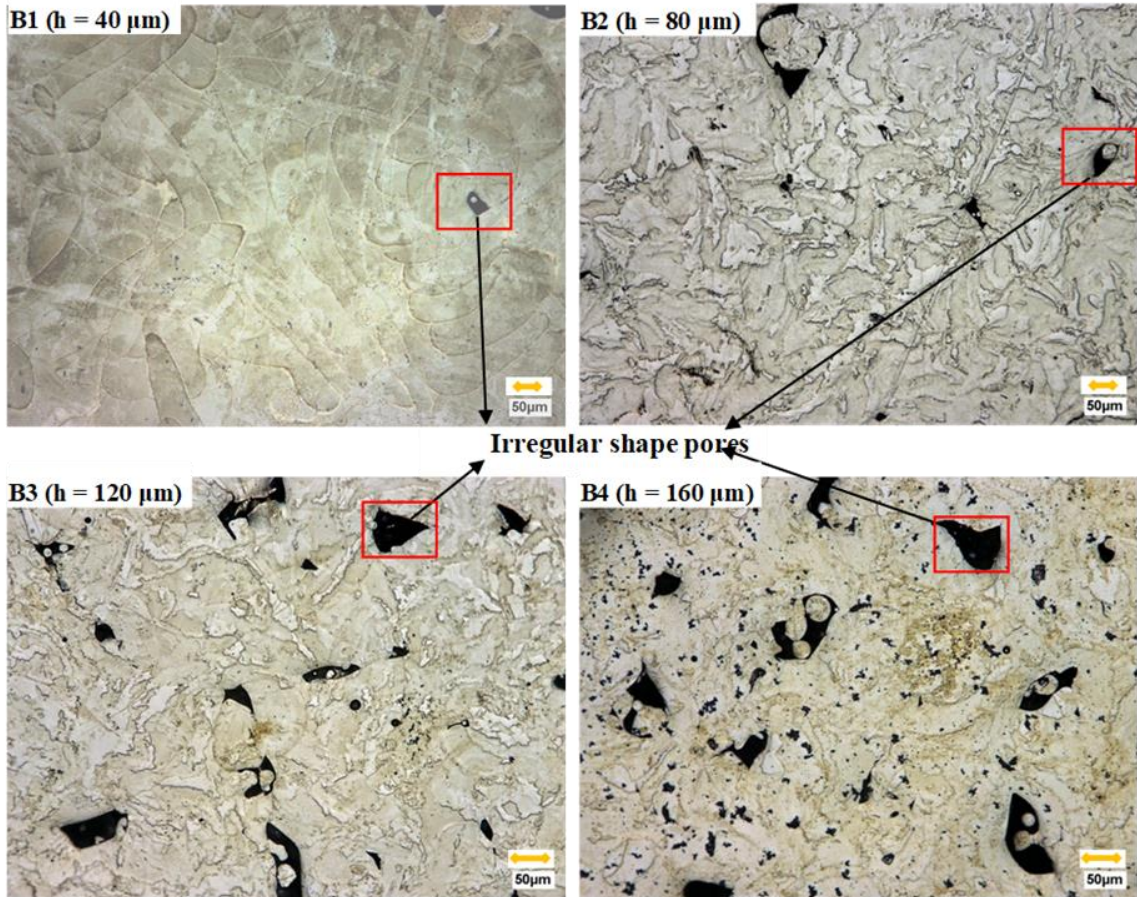


Figure 3.2 BD optical micrographs of L-PBF-AM-fabricated $\text{Ni}_{50.8}\text{Ti}_{49.2}$ samples fabricated at 50 W and various hatch spacing: B1 (40 μm), B2 (80 μm), B3 (120 μm), B4 (160 μm)

Further microstructural analysis utilizing electron backscatter diffraction (EBSD) was done on specimens of A1 (40 μm), A3 (120 μm), A6 (240 μm), B1 (40 μm), B3 (120 μm), and B4 (160 μm) samples. The results of the EBSD experiments for groups A and B are shown in Figure 3.3 and Figure 3.4, respectively. The as-collected inverse pole figure (IPF) maps are shown at the top of the figures. While the respective pole figures (PF) from the analyzed areas are shown at the bottom of the figures. A miscoloring of the grains within the analyzed area can be observed in both groups, stemming from low confidence index values during the indexing. This miscolorization can be attributed to several factors such as mechanical deformation from inadequate sample prep, strain from dislocations caused by mechanical deformation, grain sizes smaller than the step size of the scan, or phases that

were unindexable [137]. In all fabrications for groups A and B, several regions within the microstructure were unindexed, including areas outlining the grain boundaries. These regions of unindexed pixels can also be attributed to retained martensite from the fabrication.

For group A, Figure 3.3 (a-c), it is immediately apparent that the microstructures are different from one another as the hatch spacing is changed. The grain size and shape differ drastically from A1 to A6. This is not surprising as the optical micrographs of the fabrications showed differences in the melt pools overlap distance and the grains in the IPF maps solidifying in proportional dimensions. It was surmised that the melt pool boundaries are the dark bands that were unindexed as observed in the A1 and A3 fabrications, Figure 3.3 a and b respectively. These dark bands could be due to the dislocation structures left behind from the solidification. This remnant of solidification structure is not unknown and has been observed in several different L-PBF-AM fabricated materials [138-140].

Immediately, it is apparent that the A1 specimen has a [1 1 1] texture, shown both in Figure 3.3 a and d, along the build direction, combined with small irregular shape grains (with no specific orientation directions) were distributed all over the cross-section area. The A3 sample has square like collections of grains (also shown in Figure 1) and these structures look similar to those observed previously [141] [103]. A3 showed that the grains in the melt pool grow epitaxially from the melt pool boundaries and meet the centerline of the melt pool. The melt pool boundaries bisect the square grains in the center. A weak [0 0 1] texture was observed in this specimen, aligned 45° from the scan directions, which can be detected by comparing Figure 3.3 b and e. The melt pool boundaries observed in A3 are $99\pm 18\ \mu\text{m}$, which is close to the implemented hatch spaces. The IPF map for the A6 in

Figure 3.3c revealed similar but larger square like grains to those observed in A3. The center of the squares revealed circular-shaped grains with no apparent texture. The squares were outlined with [0 0 1] type grains on the melt pool's edges, which was not observed in A1 and A3. Here the melt pool boundaries were not readily observable in the IPF maps but are presumed to be present within the [0 0 1] channels. The PF in Figure 3.3 f for the A6 fabrication revealed a weak [0 0 1] texture aligned with the scan directions.

In L-PBF-AM, elongated columnar grains along the BD are often observed as during the process, the previously deposited layer is re-melted and acts as a substrate from which solidification can occur. The growth direction is parallel to the maximum thermal gradient at the solidification front, which is normal to the rear melt pool surface and thus influenced by the melt pool shape [95, 102]. It should be noted that the mode of solidification is dependent on the ratio of thermal gradient (G ($^{\circ}\text{C}/\text{mm}$)) and growth rate (R (mm/s)). Altering G/R ratio in a rapid solidification process leads to the formation of three solidification-front morphologies include planar with no segregation at high G/R ratio, cellular (columnar), and dendritic (equiaxed) with segregation at intermediate and low G/R values, respectively [97, 142, 143]. Since R equals scanning speed times the cosines of the angle between G and scanning directions along the border of the melt pool under steady-state condition, it could assume a constant value for R as the scanning speed kept constant in this study [143]. While G factor was decreased by increasing hatch spacing from 40 to 240 μm . Comparing the group A optical microscopy and EBSD results could reveal that increasing hatch spacing caused solidification-front changed from mostly planar morphology in A1 and A2 to columnar shape in A3 and A4 and finally a combination of columnar and equiaxed ones developed in A5 and A6. Additionally, the texture intensity

values were halved by almost doubling the hatch spacing. The changes in microstructure can be attributed to changes in remelting process, fabrication temperature, and thereby the thermal gradient reduction when larger hatch spacing was used. Because nucleation is a low temperature process, longer hatch spacing allows more time for the underlying sublayers to cool down. At these lower temperatures, subsequent hatch depositions do not melt into as many previously solidified layers. Hence, the resulting finer features reduce texture intensity and residual stress [97].

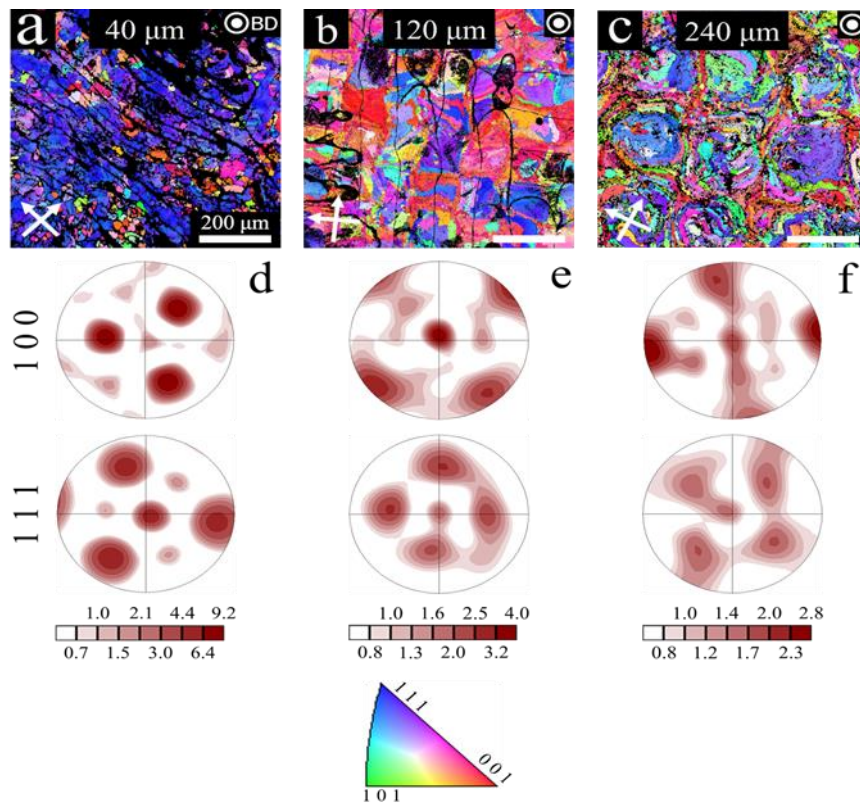


Figure 3.3 The electron backscatter diffraction (EBSD) inverse pole figures (IPF) maps and respective pole figures (PF) from the 100 W fabrications for A1 = 40μm, A3 = 120 μm, and A6 = 240 μm. IPF maps for A1, A3, and A6 are seen in (a), (b), and (c), respectively. PFs for A1 A3 and A6 are seen in (d), (e), and (f), respectively.

The fabrications for group B, Figure 3.4 a-c, are drastically different from group A where there is a little variation with the microstructure with fabrication parameters. The

grain size and shape is irregular within each fabrication and showed no apparent change within the experiment set. The B1, B3, and B4 fabrication, Figure 3.4 a-c, had elongated grains aligned with the scanning directions. Several of the large areas of unindexed areas here were caused by the porosity within the samples. No apparent texture was observed here in these fabrications which can be seen in the pole figures in Figure 3.4 d-f. Formation of equiaxed morphology during solidification and the existence of irregular shape porosity which is resultant of unmelted powder in group B samples revealed that halving the laser power from 100 to 50 W decreased the fabrication temperature and thermal gradient value, thus smaller value for scanning speed suggested to have suitable melt pool features, columnar or planar solidification morphology and stronger texture.

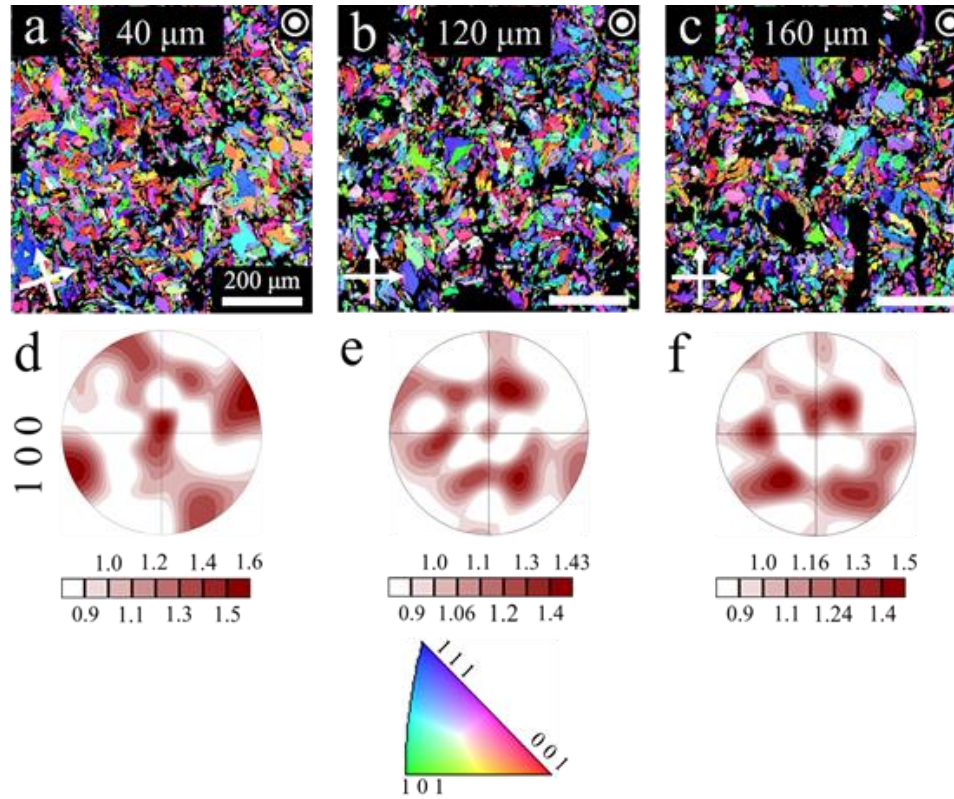


Figure 3.4 The electron backscatter diffraction (EBSD) inverse pole figures (IPF) maps and respective pole figures (PF) from the 50 W fabrications for B1 = 40μm, B3 = 120 μm, and B4 = 160 μm. IPF maps for B1, B3, and B4 are seen in (a), (b), and (c), respectively. PFs for B1, B3, and B4 are seen in (d), (e), and (f), respectively.

3.3 Transformation Temperatures

The effects of hatch spacing on the TTs of L-PBF-AM NiTi samples were studied. Figure 3.5 depicts the DSC results at the top and a variation of austenite finish (A_f), austenite peak (A_p), and austenite start (A_s) temperatures with respect to hatch spacing and volumetric energy density at the bottom. It should be noted that a shoulder was observed during heating in some samples. For better comparison, the A_f values were extracted from the sharpest peaks (not the shoulders). It is clear from this figure that TTs decrease with hatch spacing up to 160 μm (volumetric energy density of 166.7 J/mm³) for group A and up to 80 μm (volumetric energy density of 166.7 J/mm³) for group B, and then stabilizes.

For group A (100 W), A_p decreased from 50 °C to -20.5 °C as the hatch spacing increased from 40 μm to 240 μm . For group B (50 W), a similar trend was observed where A_p decreased from 8.2 °C to -31 °C when the hatch spacing was increased from 40 μm to 160 μm . Broader peaks were mostly observed for austenite to martensite transformation at low temperatures, so the martensite temperatures could not be determined accurately.

Broader peaks and higher TTs were observed in samples with higher volumetric energy density. The increase in NiTi TTs at high volumetric energy density can mainly be attributed to Ni evaporation and impurities formation during the processing [86, 104]. The smaller hatch spacing results in higher volumetric energy density and temperatures in the melt pool during the fabrication process [133], which accelerates the Ni evaporation. It is well known that the TTs of Ni-rich NiTi increase with a decrease in Ni content [24]. Therefore, the temperature variation in the melt pools resulted in different amounts of Ni evaporation and thus resulted in broader DSC peaks [144]. It should be noted that the TTs saturate around similar values at a volumetric energy density of 166.7 J/mm³ (but with different hatch spacing) in both groups. This indicates that the volumetric energy density, rather than the hatch spacing, dominates the change in the TTs when the linear energy density is kept constant. The effect of laser power on L-PBF-AM NiTi was also evaluated in our previous study, where the samples with the same volumetric and linear energy densities but with different laser powers resulted in higher TTs for higher laser power (250 W) [104], indicating the significance of laser power in L-PBF-AM fabrication.

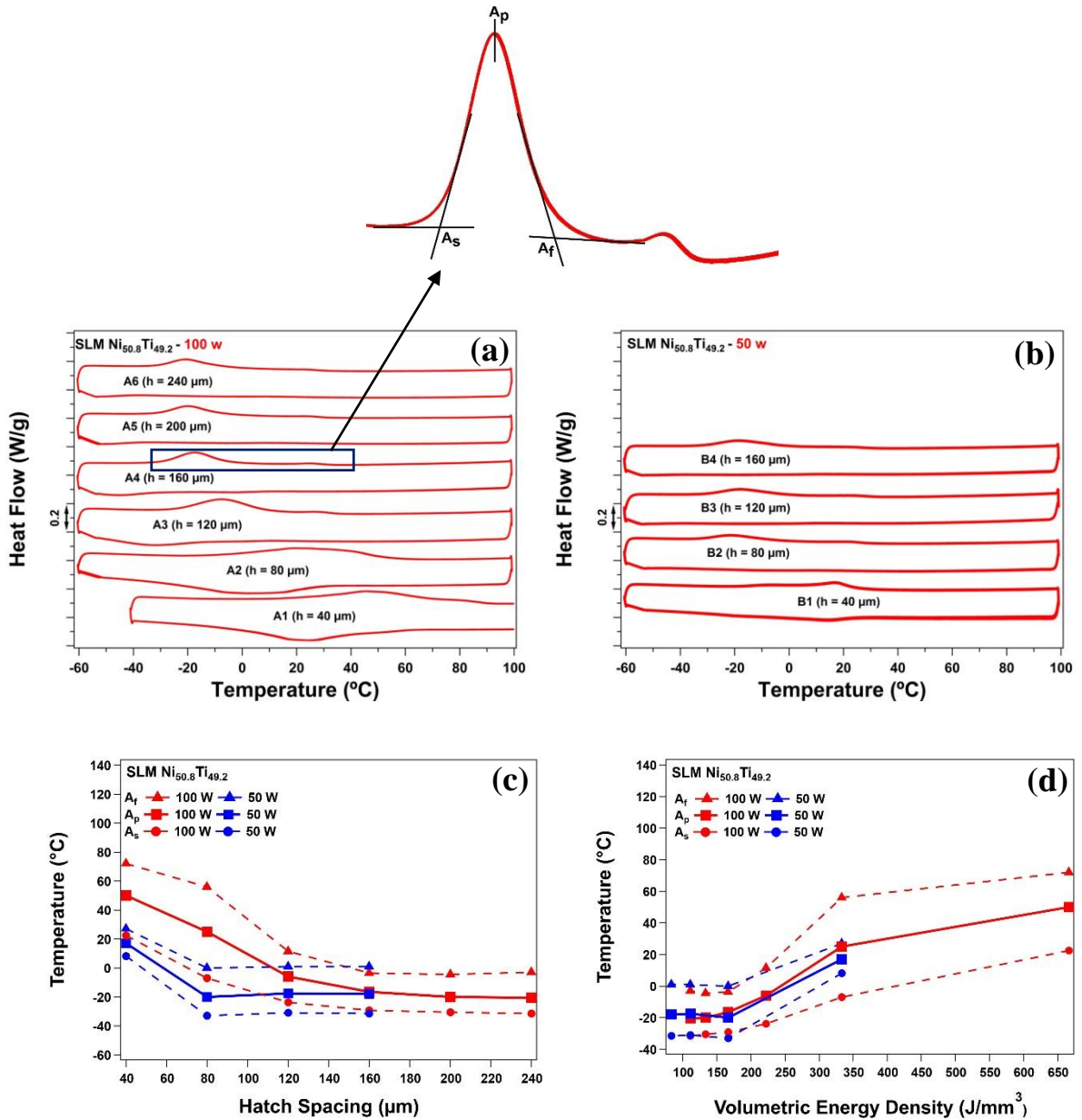


Figure 3.5 DSC results of (a) group A (100W) and (b) group B (50W) specimens, and (c) Effects of hatch spacing and (d) volumetric energy density on TTs (A_s , A_p and A_f) of L-PBF-AM-fabricated $\text{Ni}_{50.8}\text{Ti}_{49.2}$ at two different laser powers: group A (100 W) and group B (50 W)

3.4 Mechanical Behavior

Figure 3.6a and b depict the compressive responses of the L-PBF-AM NiTi samples at room temperature ($\sim 24^{\circ}\text{C}$) for the group A and B samples, respectively. Since the A_f of most specimens is higher than 24°C , samples were heated upon unloading to complete the

transformation from martensite to austenite. The colored arrows showed the amounts of recovered strain upon heating on the x-axis. A1 and A2 demonstrate low critical stress for transformation/variant reorientation during loading with limited recovery upon unloading. However, their retained strains almost fully recover upon heating. Other samples (A3-A6) show partial superelasticity as their TTs are lower than A1 and A2 and they are initially austenite at the beginning of the testing. Upon heating of A3-A6, partial recovery of the residual strain was observed due to the increased amount of plastic deformation stem from the increased critical stress. The critical stress of transformation for this group correlates well with their TTs; for specimens A1 to A6, the critical stress rises first and then saturates as the difference between test temperature and M_s of the specimens does.

For group B specimens (Figure 3.6b), partial superelasticity was observed for all the samples. Upon heating, only partial recovery was observed, as indicated by the arrows in the figure. It is worth noting that both the compressive responses and TTs of the samples fabricated with a laser power of 50 W do not alter significantly with hatch spacing. The slight decrease in critical stress with hatch spacing can be attributed to the increased porosity levels.

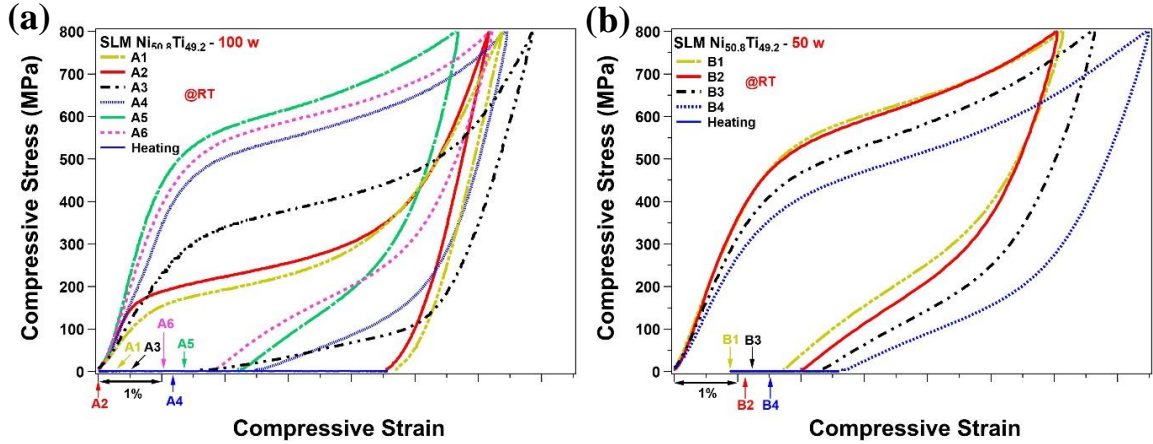


Figure 3.6 Compressive stress-strain curves of L-PBF-AM Ni_{50.8}Ti_{49.2} samples fabricated at different hatch spacing, tested at room temperature for (a) group A (100 W) and (b) group B (50 W) laser powers.

To compare specimens' superelastic behavior, the compression tests were conducted at A_f+20 °C and the results are shown in Figure 3.7. Since broad and double peaks were observed in DSC results, samples were first thermally cycled under 10 MPa to detect their A_f^σ from the strain-temperature curves via the intersection method. Then, the tests are conducted the $A_f^\sigma+20$ °C which approximately corresponds to A_p+40 °C from the DSC results. Thus, the testing temperatures in Figure 3.7 were varied from 20 °C for A6 to 90°C for A1. for most of the samples, the critical stresses are increased when compared with the results shown in Figure 3.6, obtained at 24 °C, since the testing temperatures were higher. The maximum strain upon loading was decreased due to the increase in the critical stress, resulting in incomplete forward transformation. The maximum stress of 800 MPa was selected to be consistent with our previous failure studies to avoid excessive plastic deformation [14, 104, 145].

It is revealed that, in general, critical stress decreases, and maximum strain increases in both groups as the hatch spacing increases. The critical stress of NiTi depends on the

Classius-Clapeyron slope and the difference between the testing temperature and M_s . Since all the samples were tested at $A_f^\sigma+20$, critical stress mainly depends on the transformation hysteresis (A_f-M_s), texture, enthalpy, and grain size [35, 146-148]. It should also be noted that the porosity within the samples can cause variations in the local stress that might result in lower critical stress values recorded in the experiments.

The irrecoverable strain of about 1-2% was observed in all samples and the maximum recovery was observed in the samples with lower hatch spacing regardless of the laser power. It should be noted that increased hatch spacing results in larger grain size, higher porosity (beyond a threshold hatch spacing) and Ni evaporation, and loss of [001] texture (for group A samples), resulting in decreased strength of the samples.

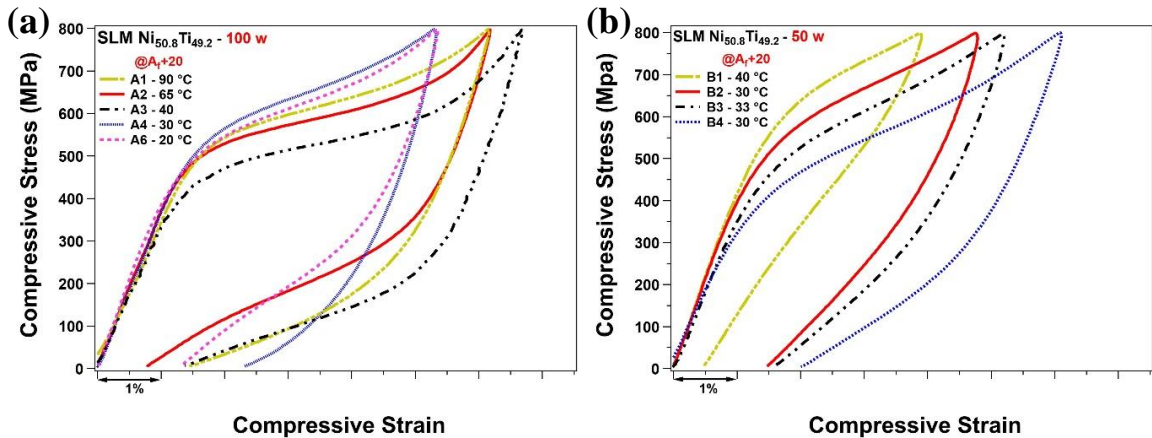


Figure 3.7 Compressive stress-strain curves of L-PBF-AM $Ni_{50.8}Ti_{49.2}$ samples fabricated at different hatch spacing for (a) 100 W and (b) 50 W laser powers, tested at temperatures of $A_f^\sigma+20$ °C. of each sample.

To investigate the cyclic response of the L-PBF-AM fabricated of SMA samples, they are stress cycled between 5 and 800 MPa for ten cycles at $A_f^\sigma+20$ °C and subsequently heated. The results of cyclic tests on samples with hatch spacings of 40 μm (A1 and B1), 80 μm (A2 and B2), and 160 μm (A4 and B4) are shown in Figure 3.8. In all samples,

mechanical cycling has significantly reduced the amount of hysteresis, even just after the first cycle. The almost fully recoverable superelastic response was achieved after several cycles. The stress-strain response was almost stabilized after ten cycles, indicating that mechanical cycling can be an effective training technique for L-PBF-AM-fabricated NiTi. A higher amount of irrecoverable strain was observed in the samples with larger hatch spacing for both groups of specimens.

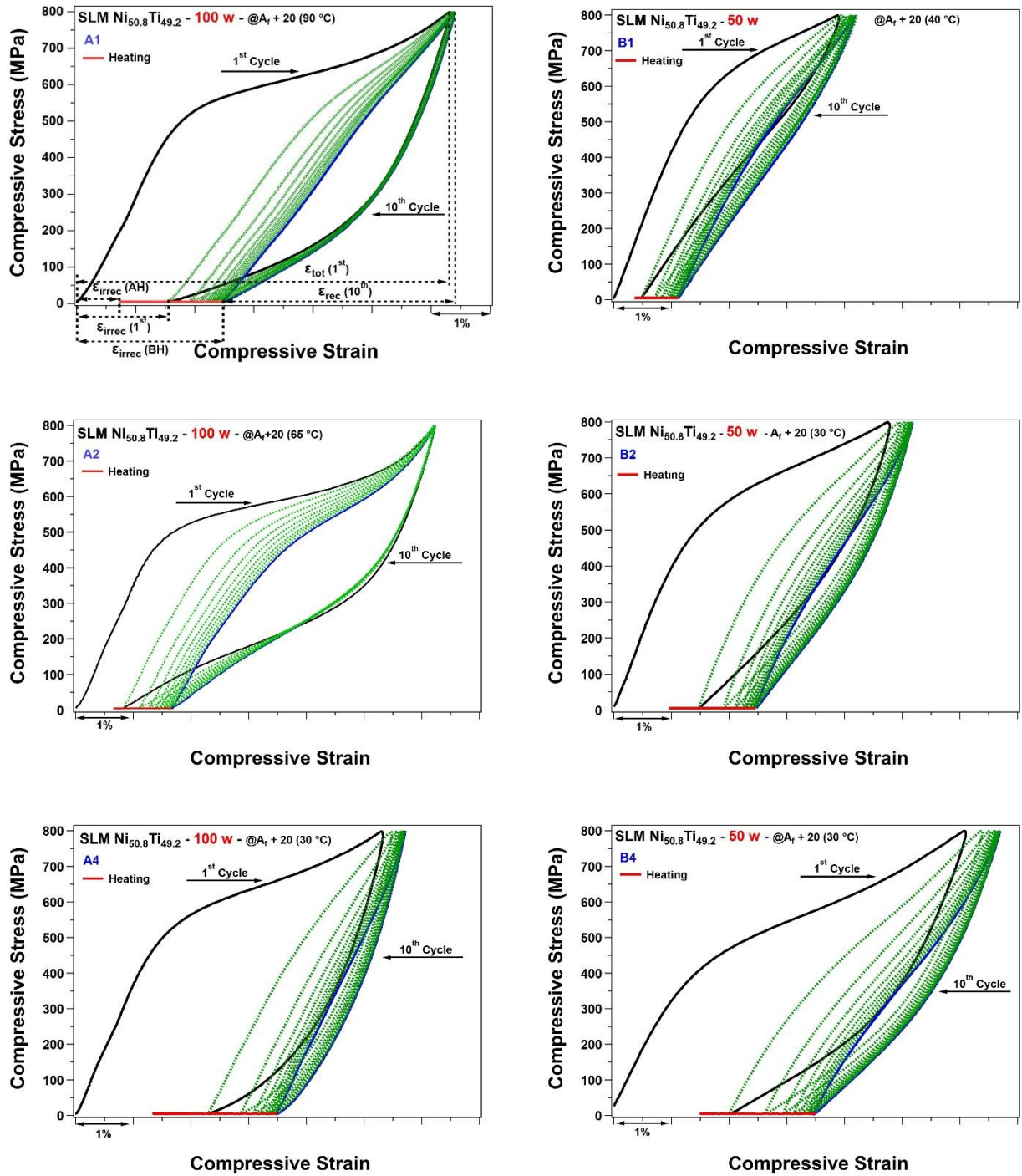


Figure 3.8 Superelastic cycling of L-PBF-AM NiTi with low, 40 μm , (top) and high hatching spacing, 160 μm , (bottom) for laser powers of 100 W (left) and 50 W (right) at temperatures of $A_f^\sigma + 20$ $^\circ\text{C}$

Table 3.2 summarizes the mechanical response of samples at the first and 10th cycles of compression at $A_f^\sigma + 20$ $^\circ\text{C}$. The total strain (ϵ_{tot} (%)), irrecoverable strain (ϵ_{irrec} (%)),

recoverable strain (ϵ_{rec} (%)) and recovery ratio ($\epsilon_{rec}/\epsilon_{tot}$) are provided in this table. It should be noted that these selected values strongly depend on the testing temperature and loading stress levels. According to the first group results, A2 (80 μm and 333.3 J/mm^3) shows a promising 86.52 % recovery ratio at the first cycle and a recoverable strain of 4.56 % after ten cycles. On the other hand, the A4 (160 μm and 166.7 J/mm^3) shows a poor behavior with a recovery ratio of 43.7% in the first cycle and a recoverable strain of 2.23 % after ten cycles.

In the second group, the best superelastic behavior belongs to B1 (40 μm) with a recovery ratio of 87.4 % and B4 (160 μm) exhibits the poorest superelasticity with a recovery ratio of 67.2 %, respectively. Increased level of porosity in the group B specimens resulted in poor superelastic response [104].

Table 3.2 Summary of cyclic test results of group A (100 W) and group B (50 W) L-PBF-AM-fabricated $\text{Ni}_{50.8}\text{Ti}_{49.2}$ SMAs.

	L-PBF-AM $\text{Ni}_{50.8}\text{Ti}_{49.2}$	Max Applied Stress MPa	1 st Cycle				Before and After Heating (BH & AH)		10 th Cycle
			ϵ_{tot} (%)	ϵ_{irrec} (%)	ϵ_{rec} (%)	Recovery Ratio (%)	Total ϵ_{irrec} BH (%)	Total ϵ_{irrec} AH (%)	ϵ_{rec} (%)
Group A	A1	800	6.31	1.59	4.71	74.64	2.46	0.73	3.93
	A2	800	6.23	0.84	5.39	86.52	1.66	0.68	4.56
	A3	800	6.73	1.42	5.31	78.90	2.86	-	4.09
	A4	800	5.31	1.14	2.32	43.69	3.49	1.35	2.23
	A6	800	5.36	1.33	4.03	75.18	2.68	-	3.07
Group B	B1	800	3.90	0.49	3.41	87.43	1.10	0.38	3.07
	B2	800	4.77	1.47	3.48	72.95	2.46	0.98	2.72
	B3	800	5.19	1.57	3.61	69.55	2.73	1.13	2.95
	B4	800	6.10	2.00	4.10	67.21	3.47	1.51	3.23

3.5 Discussion

Figure 3.9 summarized the effect of laser power/scanning speed (left to right) and hatch spacing (top to bottom) on the texture of additively manufactured NiTi. Our previous study reported almost a similar microstructure for samples fabricated by large hatch spacing where 250 W laser power and 1250 mm/s scanning speed were utilized. By increasing the hatch spacings, square shape and columnar grains appeared. The lowest hatch space employed in that study was equal with laser beam diameter (80 μm) and revealed strong [100] texture with planar morphology [103]. This intense texturing in [100] direction during L-PBF-AM process was also reported for other cubic materials when hatch spacing lower or equal to laser beam diameter was implemented such as FeAl with 100 μm focused laser spot and 70 μm hatch spacing [149], Inconel 625 with 80 μm focused laser spot and 60 μm hatch spacing [150] and NiMo with 100 μm focused laser spot and 80 μm hatch spacing [151]. For BCC metals such as NiTi, the easy growth orientation is determined as the [100] crystal direction [152, 153]. In this study, when the 40 μm hatch space was implemented, strong [111] orientation appeared in the sample (A1). [111]-texture is also observed previously in BCC Tungsten and Tantalum alloys by altering the scan strategy and changing the local direction of heat flux in the melt pool [98, 102]. It can be concluded that the decrease of laser power from 250 to 100 W results in the changing texture from [001] to [111] direction due to the change in melt pool shape in NiTi alloys, and/or reduction of hatch spacing/overlap distance from 80 to 40 μm alters the maximum temperature and thus the temperature gradient and texture [154]. Further decrease in laser power increases pores and defects, inhibiting the epitaxial grain growth and texture formation [155]. Thus, it could be concluded that selecting appropriate laser power and

specific scanning speed to secure suitable melt pool features followed by employing hatch spacing less/equal to laser beam diameter would result in a strong texture with a particular direction by L-PBF-AM process. Moreover, it was proposed that the melt pool shape affects the angle between the preferred crystal growth direction and BD, and thus the texture [156].

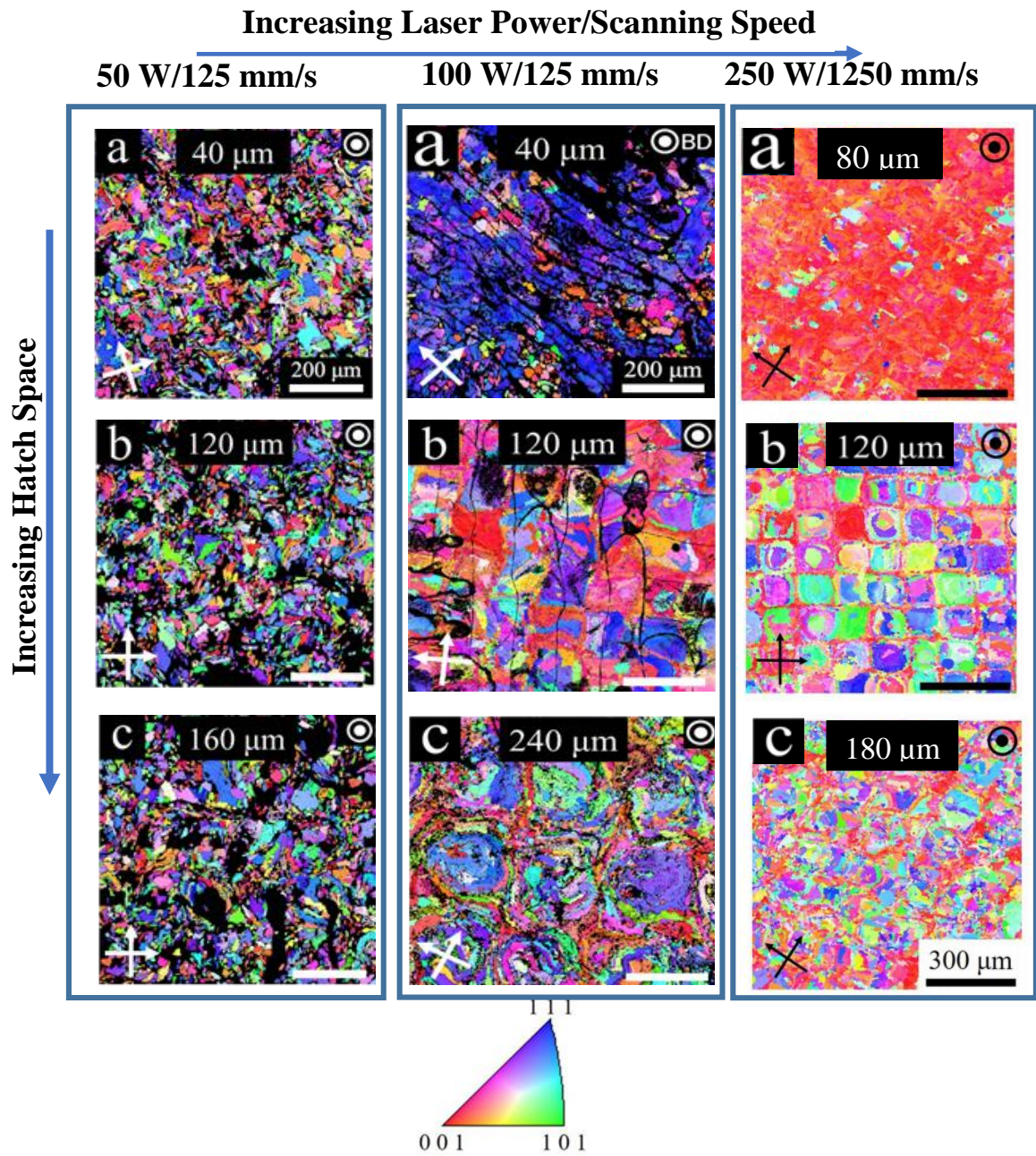


Figure 3.9 EBSD IPF maps for representative samples showing the influence of laser processing parameters on the texture development for the samples fabricated with laser powers of 50 W, 100 W, and 250 W [103, 157].

The rapid cooling and solidification of melted powder during L-PBF-AM process affects the size and shape of the melt pool [129], demonstrating a significant impact on the microstructure and grain growth of the fabricated samples [130]. Previous studies have shown that the melt pool's width and depth depend on the laser beam's size, laser power, and scanning speed [133, 134]. At constant laser beam focus, a combination of laser power

(P) and scanning speed (V) ($\text{Linear energy density} = P/V$) could predict the final shape of melt pools. Schematic of different melt pool shapes concerning the employed PPs present in Figure 3.10. Generally, by fixing V or P at a low value, as much as P or V increases, a deeper or shallower melt pool will be formed, higher or lower fabrication temperature and content evaporation will exist, the chance of keyhole appearance in microstructure will be increased or decreased, and formation of discontinuous laser tracks will be decreased or raised, respectively. Thus by adjusting the laser power and scanning speed, the melt pool shape could alter between deep, elliptical, and shallow shapes (Figure 3.10a).

In L-PBF-AM process, the laser creates a molten pool of metal where normally the hottest point belongs to the centerline, which causes thermal gradients to be perpendicular to the melt pool boundaries (Figure 3.10a). During solidification, grains tend to grow toward the temperature gradient (Figure 4.7). The [100] orientation is reported to be the favorable crystal growth direction during the solidification of cubic materials [152]. As presents in Figure 3.10b, the cubic crystals have a 90° symmetry feature, and in cubic material, this cube turns to align the [100] direction with thermal gradient direction, which is followed by aligning a specific orientation with building direction during L-PBF-AM fabrication.

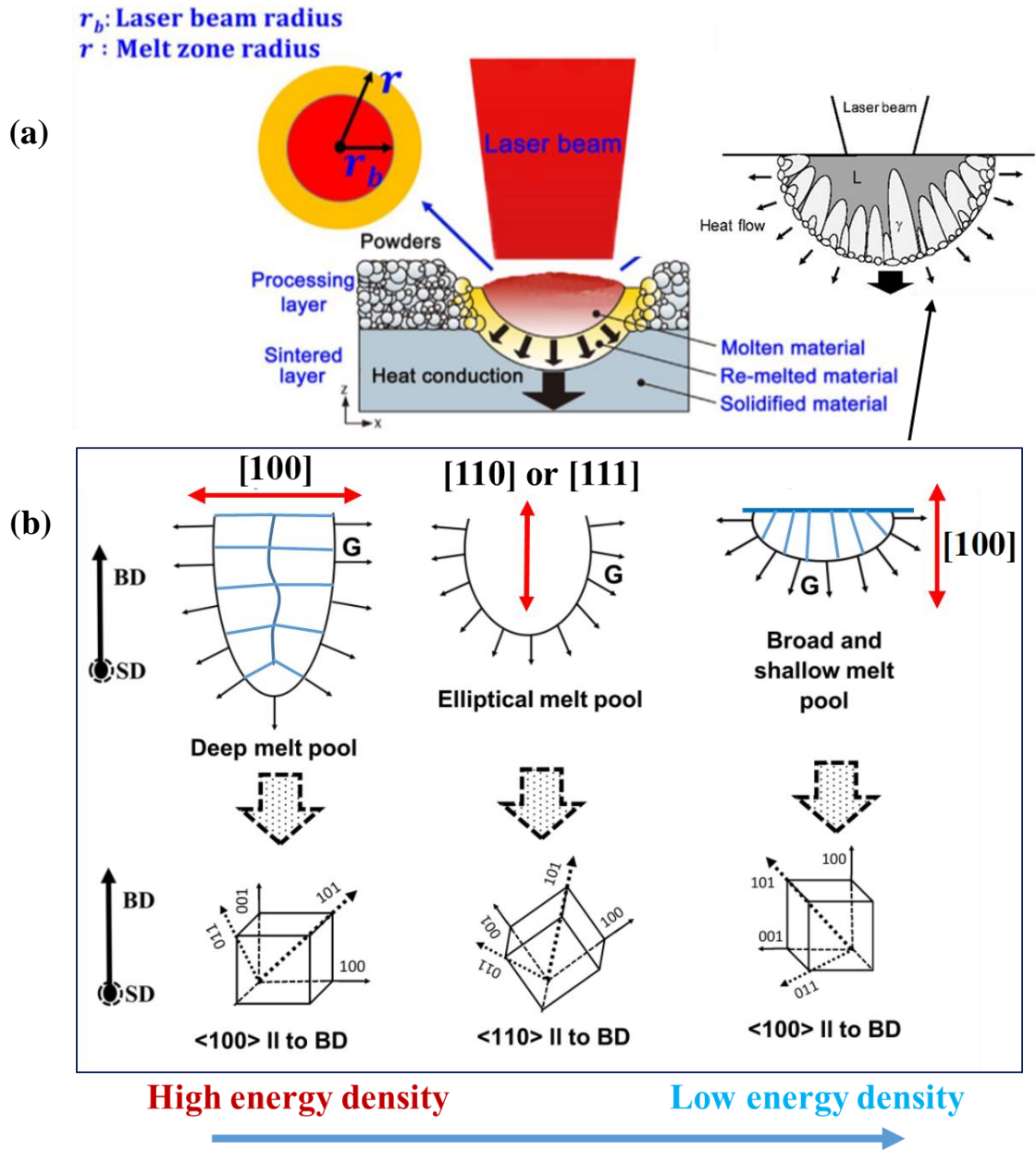


Figure 3.10 (a) Schematic of a melt pool, thermal gradient direction, and grain growth [158, 159]. (b) Impact of altering laser power and scanning speed on melt pool shape and cube crystal turning [160].

It should be noted that by careful selection of hatch spacing (lower than laser beam diameter is suggested), subsequent laser tracks re-melt the oriented grains and eliminating grains with other directions to keep the grains parallel to building direction, following by planar solidification front and formation of a strong texture in a specific direction along

the building direction (such as strong [111] and [100] textures in 40 and 80 μm hatch spacing cases) (Figure 3.11a). By increasing hatch spacing to a moderate value, the solidification front will be altered to planar (two phases) or columnar, resulting in elongated columnar grains parallel to building direction side to side each other with different orientations and the existence of channels between them (Figure 3.11b). If high hatch spacing is implemented, grains with various growth directions find a chance to develop and an equiaxed solidification front appears, resulting in island grain formation with random orientation changing (Figure 3.11c). Finally, by applying suitable layer thickness, partial re-melting of sublayers and epitaxial growth of grains in thermal gradient direction, where grains of the next layers inherit the orientation of the previously formed grains, leads to the development of an intense or poor texture in final products.

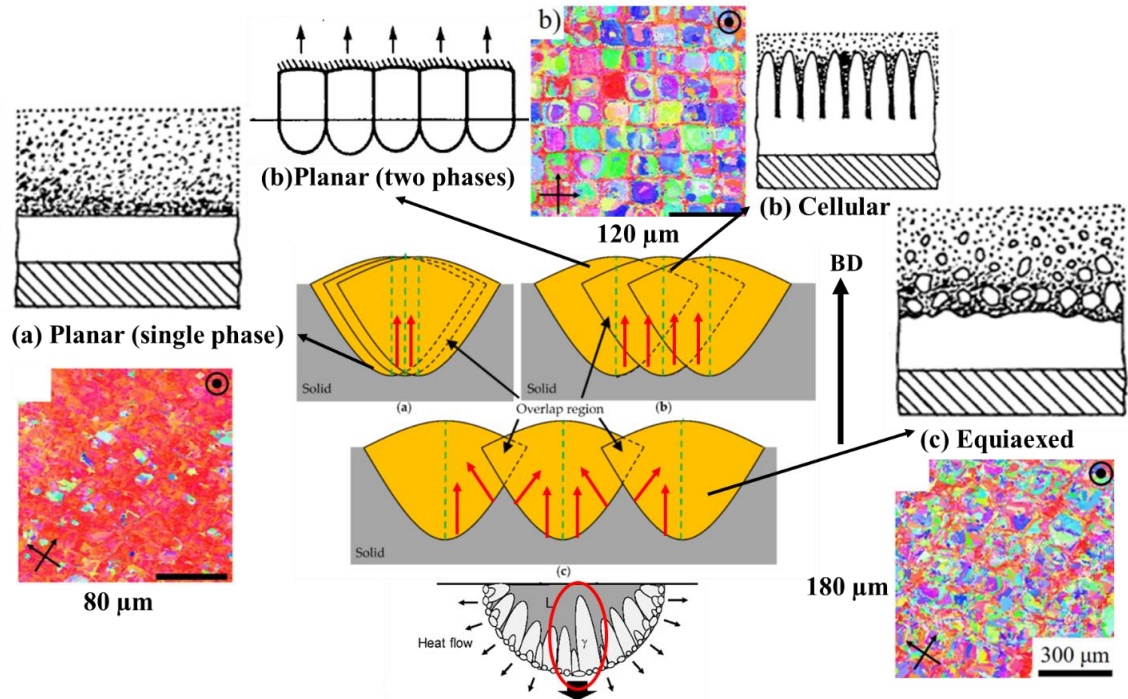


Figure 3.11 Impact of hatch spacing in solidification and texturing the L-PBF-AM samples [159, 161].

One may consider the volumetric energy density as the main parameter that governs the L-PBF-AM NiTi microstructure and mechanical response. However, in this study, although A2 & B1 (80&40 μm), A4 & B2 (160&80 μm), and A6 & B3 (240&120 μm) samples had the same volumetric energy density of 333.3, 166.7, and 111.3 J/mm^3 , respectively, they have distinct microstructure, TTs and mechanical behavior. A2 (h=80 μm) and B1 (h=40 μm) samples showed the best mechanical behavior in their groups. A2 (h=80 μm and $E_v=333.3 \text{ J}/\text{mm}^3$) demonstrated the highest total strain and recovery ratio after the first and ten cycles. Additionally, by comparing the impact of hatch spacing in samples fabricated with 100 W and 250 W, better shape memory behavior was achieved when the hatch spacing is 80 μm [103]. We recommend increasing scanning speed and decreasing hatch spacing when the laser power is growing to reach a sufficient volumetric energy density to avoid pore formation and have a good shape memory behavior.

In this section, the linear energy density was 0.8 J/mm for group A and 0.4 J/mm for the group B specimens. The linear energy density is one of the main parameters to control the shape and size, and energy of the melt pool since hatch spacing does not significantly affect the melt pool, but it affects the thermal gradient and cooling rates of the melt pool. However, it should be noted that hatch spacing (and volumetric energy density) strongly influences the microstructure (texture, grain size, porosity level, the overlap of melting pools, secondary phase formation, and the shape of the grains), TTs (thermal history, the number of re-melting and re-heating processes that affects Ni-evaporation, impurity and precipitate formation) and the mechanical response (strength depends on composition, porosity, and texture) of L-PBF-AM fabricated Ni-rich NiTi specimens. Thus, both

parameters should be considered for successful fabrication of samples and to tailor their properties.

3.6 Conclusion

This work evaluates the effects of PPs on the shape memory and mechanical properties of the L-PBF-AM-fabricated NiTi SMAs. The effect of hatch spacing on the microstructure, TTs, and compression properties of L-PBF-AM Ni_{50.8}Ti_{49.2} alloys fabricated with two selected laser powers of 100 W and 50 W are investigated. Based on the work presented here, the following conclusions can be made:

- The hatch spacing plays an essential role in the L-PBF-AM fabrication of NiTi alloys. The change in the melt pool's local heat transfer through hatch spacing can result in a drastic change in the final texture since strong [111] texture was observed when hatch spacing less than laser beam diameter was implemented.
- Linear energy density (or laser power at a constant scanning speed) plays an important role in the melt pool features of the L-PBF-AM fabricated components. A larger melt pool was obtained for higher laser power (or higher linear energy density) while the scanning speed was kept constant.
- The samples fabricated with the same volumetric energy density but different linear energy density showed distinct microstructures and shape memory behaviors.
- When the linear energy density was constant, TTs were decreased with decreasing volumetric energy density (or increasing hatch spacing in this study) and then saturated for volumetric energy density of lower than 166.7 J/mm³.
- Higher strain recovery and more stable superelastic behavior were obtained for lower hatch spacing, regardless of the employed laser power.
- Careful selection of linear energy density is needed to adjust the size and continuity of melt pools, while the selection of sufficiently high volumetric energy density is required for scan track overlaps to avoid pores and adjust the fabrication temperature to control the solidification rate and content evaporation.

4 Impact of Building direction (BD) and Loading Mode on L-PBF-AM Ni_{50.8}Ti_{49.2}

The arrangement of the part on the substrate plate can significantly influence the microstructure and properties of the L-PBF-AM parts. The effect of the build orientation on density, level of porosity, residual stress, surface roughness, microstructure, mechanical properties, and fatigue performance of the L-PBF-AM parts have been studied for several alloys, including NiTi [44–47]. Dadbakhsh et al. investigated the anisotropy of L-PBF-AM compression parts resulted from different building orientations [46]. The growth of austenite fine grains along the building direction (BD) was determined as the main source of the anisotropy in shape memory behavior of the L-PBF-AM NiTi samples. Moreover, texture can further be altered by the laser-scanning strategy employed [95] where the rotation of the scanning direction between the layers improved the competitive grain growth.

The tensile property of L-PBF-AM NiTi is an essential property in almost all applications of NiTi [162], and the functionality of NiTi alloys is highly sensitive to the loading modes and microstructure [83, 163, 164]. The defects (e.g., residual stresses, cracks, pores) associated with a layer-based feature of AM may lead to serious problems during tensile testing, but not compression, as the defects would be collapsed in compression testing. Both polycrystalline and single crystal/textured NiTi alloys show the anisotropic thermomechanical behavior under uniaxial loading [18,22,23]. Tensile loading is mostly the favored stress state for inducing martensite transformation with respect to the compression [24–26]. Higher transformation strain, lower stress-induced transformation, and steeper plateau are mostly achieved under tension rather than compression in

polycrystalline NiTi [27]. However, in the single crystal and the strongly textured NiTi alloys, the scenario could differ based on the grain orientation [28,29]. Grain size and orientation also play a significant role in the final properties of the NiTi parts [29–32].

To date, there are limited studies on the effect of the building orientation of AM NiTi in the literature. Furthermore, no comparative study has been done between compression and tension properties to see the effect of building orientation on the anisotropy in tension and compression. The present chapter aims to link the impact of build orientation on the microstructure and anisotropy behavior of L-PBF-AM Ni_{50.8}Ti_{49.2}. In this regard, NiTi compression and tension specimens are additively manufactured via L-PBF-AM technique in three different build orientations (0, 45, 90 degrees). Thermomechanical behavior of the as-fabricated samples was evaluated in compressive and tensile stress states. The microstructural evaluation was also performed to capture the influence of sample orientation relative to BD on the microstructure of the as-built samples. The anisotropic thermomechanical properties are then linked to the different microstructure and texture achieved from each build orientation condition.

4.1 Fabrication

Compression and tension samples were additively fabricated by employing laser power, scanning speed, hatch spacing, and layer thickness of 250 W, 1250 mm/s, 80 μm , and 30 μm , respectively. As demonstrated in Figure 4.1, a series of dog-bone and rectangular specimens were fabricated with three angles between sample orientation and the substrate, i.e., 0, 45, and 90 degrees. These samples will be abbreviated as C0, C45, and C90 for compression samples and T0, T45, and T90 for tension ones hereafter. The x/y

scanning strategy was considered in all cases. Important directions for microstructural analysis were presented by BD, loading direction (LD), and XY-plane (perpendicular to BD).

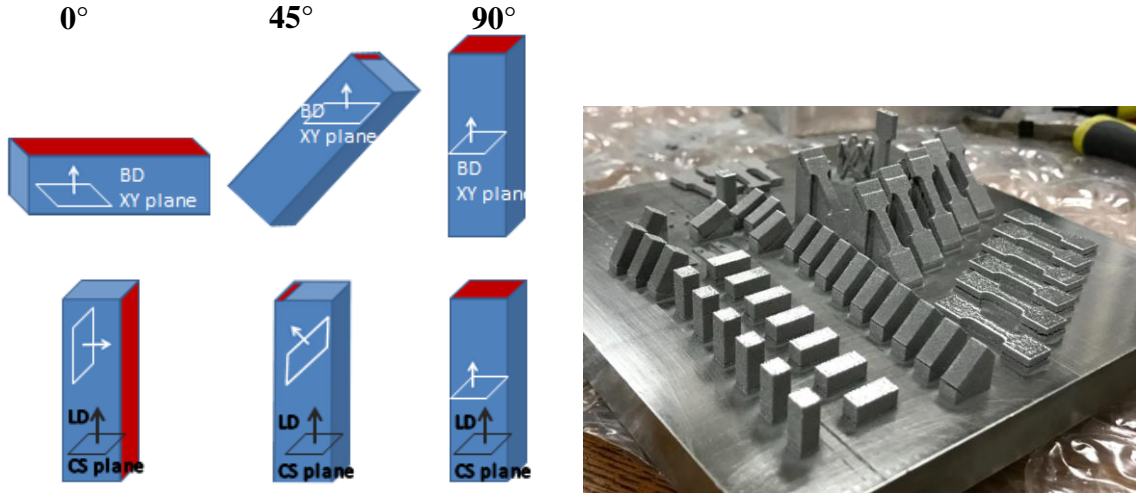


Figure 4.1 Schematics and arrangement of compression and tension samples on the build plate.

4.2 Phase transformation Responses

Figure 4.2 represents the DSC results for initial ingot, powder, and L-PBF-AM (0, 90, and 45 degrees) $\text{Ni}_{50.8}\text{Ti}_{49.2}$ (at. %). The corresponding TTs are demonstrated in Table 4.1. Multiple asymmetric and broad peaks were detected in the powder form, while a nearly perfect single-step transformation was observed in the ingot and L-PBF-AM samples. TTs of the L-PBF-AM material were higher than ingot. Additionally, Broad peaks were observed for L-PBF-AM specimens are common in additively manufactured NiTi, which is attributed to their heterogeneous microstructure. It should be noted that lower values were achieved for TTs of 45-degree samples compared to other L-PBF-AM ones. It is known that matrix composition plays an essential role in defining the TTs of NiTi alloys. The prominent mechanisms in L-PBF-AM that cause subsequent compositional changes

after fabrication are Ni evaporation due to excessive heat and temperatures above the alloys' boiling points and increases TTs [152]. In a 45-degree case, since the laser had to shift a little to the side to fabricate the next layer, less re-melting process happened for solidified layers, which decreased Ni evaporation and ended with lower TTs.

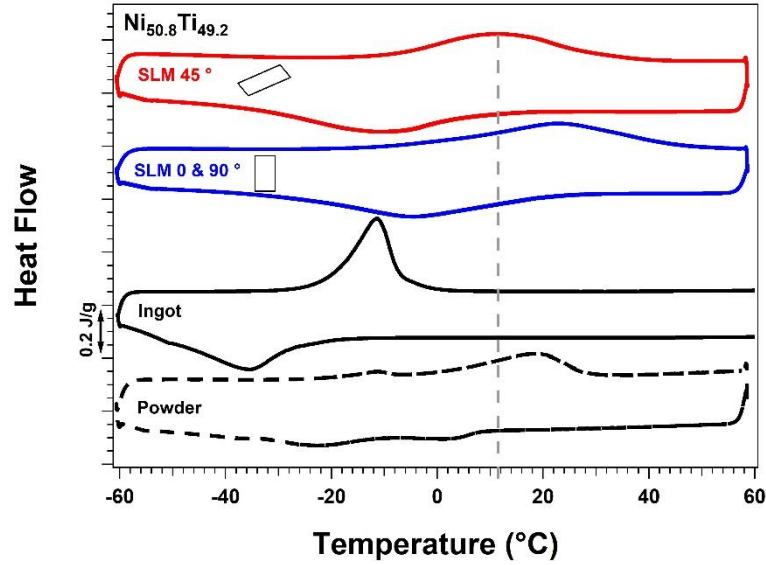


Figure 4.2 DSC graphs of $\text{Ni}_{50.1}\text{Ti}_{49.9}$ (at. %) in forms of powder, ingot, and selectively laser melted.

Table 4.1 TTs of $\text{Ni}_{50.8}\text{Ti}_{49.2}$ (at. %) in forms of ingot, powder, and selectively laser melted extracted from DSC graphs. (M_s -Martensite start, M_f - Martensite finish, A_s -Austenite start, and A_f -Austenite finish)

$\text{Ni}_{50.8}\text{Ti}_{49.2}$ (at. %)	M_s (°C)	M_f (°C)	A_s (°C)	A_f (°C)
Ingot	-26	-47	-21	-6
Powder	-8.0	-37.5	2.0	28.5
SLM 45 °	8.5	-34	-10	32
SLM 0 & 90 °	22	-28.5	-6.0	46

4.3 Microstructural analysis

EBSD analyses were performed on different directions of C0, C45, and C90 specimens. Cross-sections, XY sections, and longitudinal sections were EBSD mapped. Orientation image mapping related to LD sections is reported in Figure 4.3. All the specimens showed elongated grains in the BD, that in some case, show epitaxial growth over grains of the previous building layer, leading to larger elongated grains, with maximum size exceeding the layer thickness. Moreover, numerous smaller grains are presented besides these big elongated grains, as higher magnification EBSD maps. The latter are mostly located close to melt pool boundaries and are characterized by rather equiaxed shape with wavy grain boundaries.

It was observed that most of the grains show a preferred alignment along [001] with BD and also XY directions. A small population of big grains with different orientations can be observed, too. Their colors in OIM images are entirely different from their neighborhood, but their presence is not well visible in pole figures or inverse pole figures due to their limited number. C0 and C90 specimens show similar orientation results; grains are preferably aligned with BD, that in the former is horizontal, and in the latter is vertical: due to the 90° symmetry of cubic crystals. The [100] orientation is the predominant crystal growth direction during the solidification of cubic materials [152]. On the other hand, as well discussed in the last chapter, epitaxial growth and columnar grain growth control the solidification due to the high cooling rates; as a result, regardless of BD, the newly solidified material takes over the crystallographic orientation of previously formed grains in underlying layers [135, 165, 166] and developing a texture.

A subtle difference of the orientation with respect to the LD can be appreciated when considering the spread of the orientation in the (100) pole figures: contours of (100) pole close to the BD are elongated toward the Normal Direction. OIM appears different for the C45 specimen, as the BD is located at 45° with respect to the LD. Hence grains show a preferred [110] alignment with LD. Higher magnification EBSD maps performed on 45° sample, close to the bottom surface, evidenced that only the first layers exhibited a different orientation, with grains that grew perpendicularly to the surface.

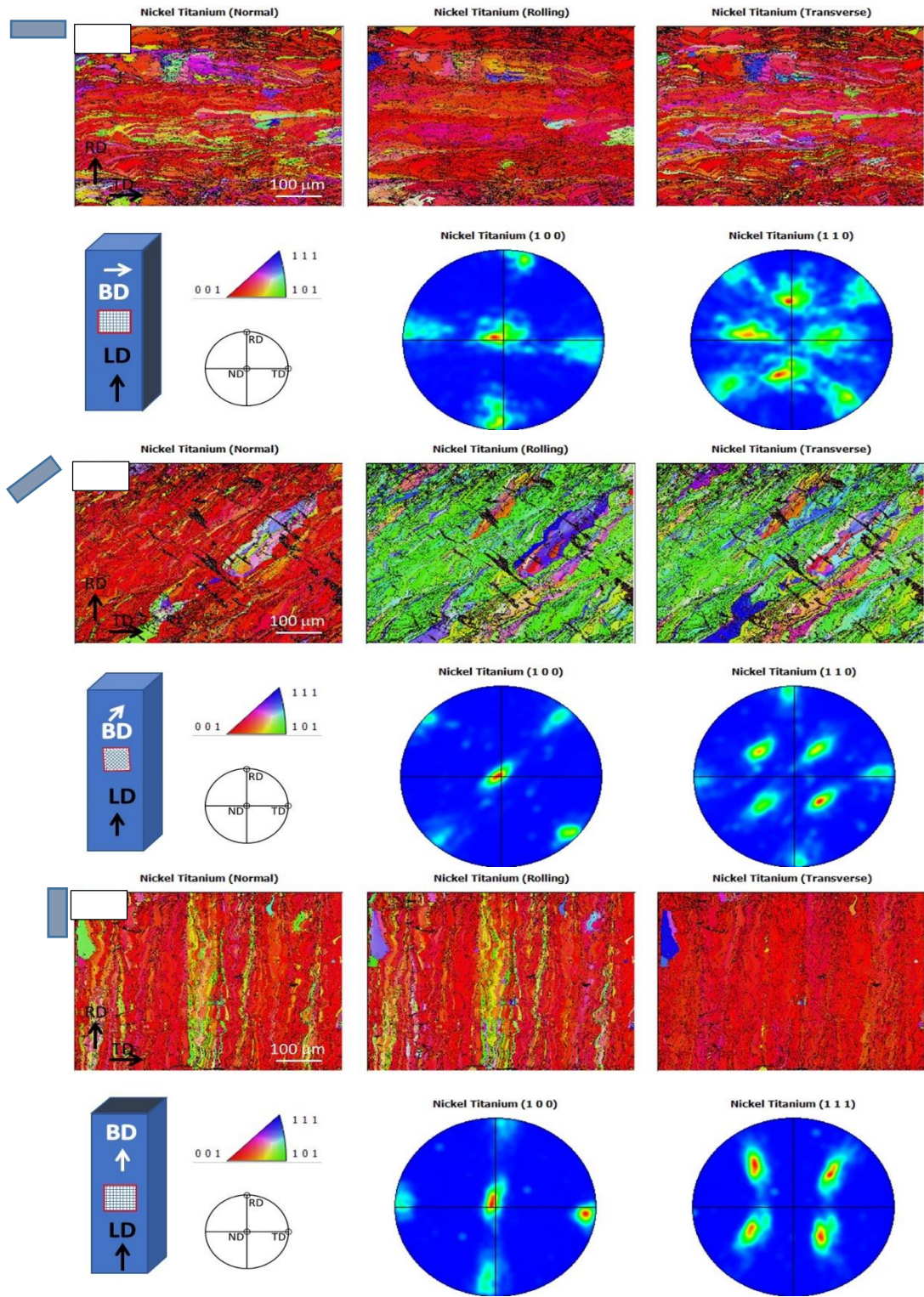


Figure 4.3 EBSD results of LD sections of C0, C45, and C90 specimens. For each specimen OIM, schematic of the section, legends, and (100) and (110) pole figures are presented. LD and BD show loading and building directions, respectively [167].

4.4 Load-biased shape memory behavior

The thermal cycling under constant compressive stress for the tensile (left) and compressive (right) samples is displayed in Figure 4.4. To perform such experiments, the samples were loaded to selected stress levels at austenite state at each cycle and then thermally cycled between a temperature below M_f and above A_f . After one complete cycle, the stress was increased incrementally and the thermal cycling was repeated for each stress level until significant plastic strain was accumulated.

Figure 4.4a depicts the shape memory behavior of T0 and C0 specimens. There was the typical stress effect on TTs, with the M_s and A_f increasing from 6 to 26 °C and 30 to 60 °C, respectively, for T0 when the stress was increased from 25 to 300 MPa. Similarly, in compressive case, the M_s and A_f were 23 and 35 °C at 50 MPa and increased linearly to 33 and 63 °C at 300 MPa stress level, and ended with 75 and 116 °C at 600 MPa, respectively. A higher recoverable transformation strain was observed for C0 with 4.4% strain compared to T0 with 2.87% at 200 MPa stress level before the appearance of irrecoverable strains.

Figure 4.4b illustrates the shape memory response of T45 and C45 samples. By changing the BD degree from 0 to 45 degrees, TTs shifted a little to the left, which has a good agreement with DSC results. As the stress level increased from 25 to 150 MPa, the M_s and A_f also raised from -7 to 10 °C and 14 to 52 °C for T45 sample, respectively. For C45, TTs increased from 16 to 35 °C and 32 to 79 °C for M_s and A_f , respectively, when the stress level raised from 50 to 400 MPa. The maximum recoverable strain of 5.31% at 150 MPa for T45 and 4.0% at 200 MPa for C45 were achieved. It should be noted that only in the 45-degree with [110] || LD condition, the tensile sample's transformation strain was

higher than the compressive sample. This behavior has a good agreement with RSSF number (section 1.2.4), in which higher RSSF value documented for tensile mode in [110] orientation resulted in higher transformation strain under lower stress levels in compression with the compressive condition.

The shape memory response of T90 and C90 specimens present in Figure 4.4d. The same increasing trend observed but in a smaller stress window of 25 and 100 MPa while M_s and A_f increased from $-7\text{ }^\circ\text{C}$ to $6.5\text{ }^\circ\text{C}$ and 20 to $28\text{ }^\circ\text{C}$ for T90, respectively. TTs were altered from 8 to 67 and 30 to $109\text{ }^\circ\text{C}$ for M_s and $A_f\text{ }^\circ\text{C}$, respectively, when stress changed from 50 to 600 MPa for C90 sample. The maximum recoverable strain of 2.16% at 100 MPa for T90, and 3.86% at 400 MPa for C90 samples were achieved.

Among the L-PBF-AM samples, it is clear that the tensile behavior highly depends on the angle between the loading and building directions, where the highest and lowest strength were observed in T0 and T90 & T45 samples, respectively. Since the LD was parallel to the BD in the case of T90 samples, while the regions of unmelted powders are between the layers [83], this made the effect of the unmelted regions between the layers more prominent, resulting in the deficient connections of consecutive layers, and hence the lower tensile strength. In addition to the LD, the difference between the tensile behavior of L-PBF-AM samples can be correlated to the number of layers along the BD [168]. For example, the higher number of layers in T90 and T45 samples might be responsible for the lower level of strength, increasing the possibility of crack formation, voids, and unmelted regions between the layers. On the other hand, in the case of T0 samples, despite that the unmelted region of powders was still between the layers, the fact that the LD was

perpendicular to the BD result in a less detrimental effect of the defects on the tensile strength of the T0 sample.

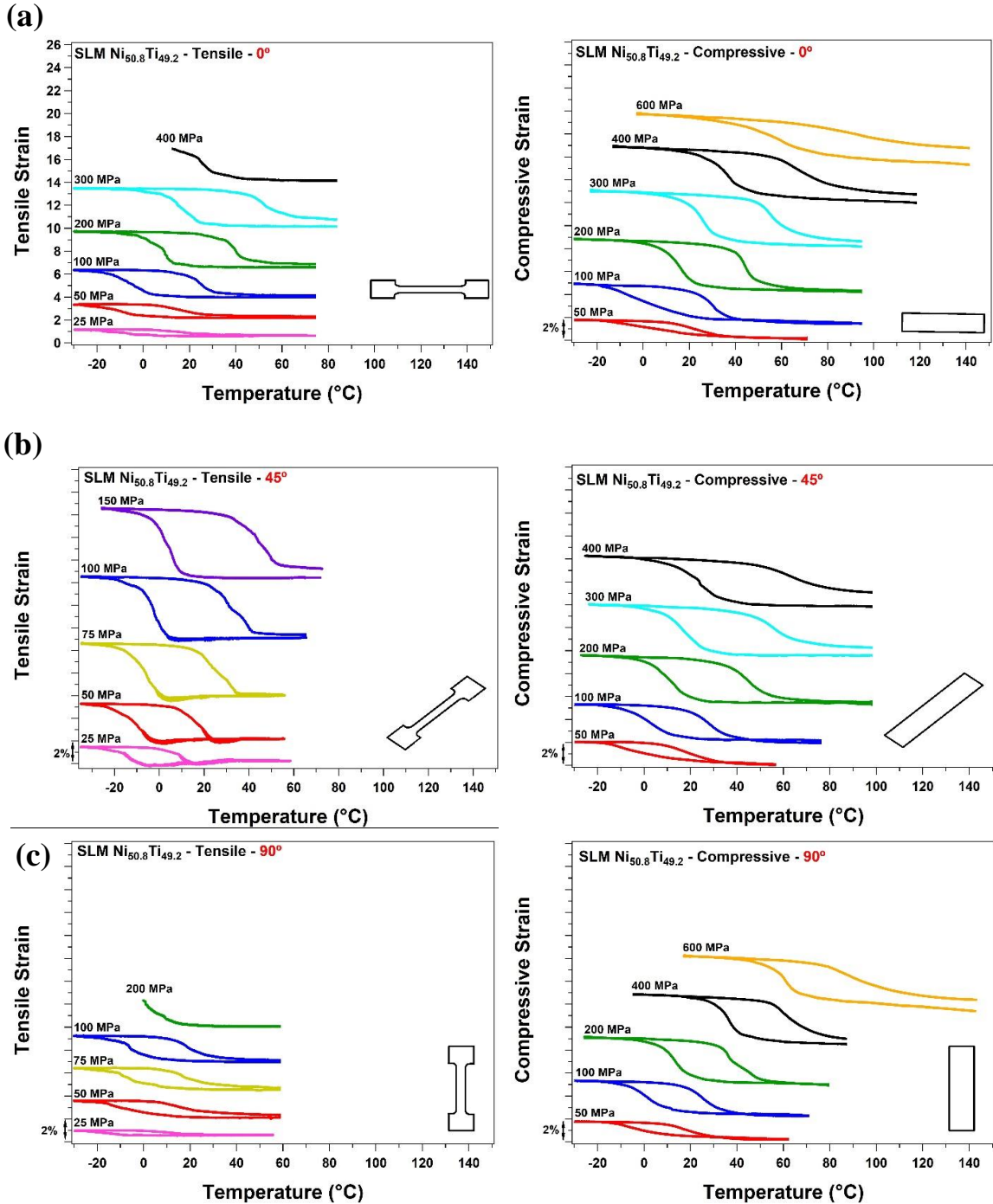


Figure 4.4 Thermal cycling under constant stress responses of L-PBF-AM Ni_{50.8}Ti_{49.2} (at. %) in tensile (right) and compressive (left) conditions with (a) 0, (b) 45, and (c) 90 degree angels between BD and substrate.

Total strain (ϵ_{tot}), irrecoverable strain (ϵ_{irr}), martensitic start (M_s), and austenitic finish (A_f) temperatures of the samples are extracted from Figure 4.4 and are plotted as a function of applied stress in Figure 4.5. In all cases, compressive samples presented higher resistance to the appearance of plasticity with illustrating a higher stress window compared to the tensile ones. However, in the compression case, the earliest failure was demonstrated for C45 sample while C0 and C90 showed the same and stronger behavior. As the defect between layers could collapse in compressive conditions, the texture could be the significant factor in altering the thermomechanical behavior of C45 specimen. While in the tensile state, as much as the number of fabrication layers increases and the angle between BD and LD decreases, developing the existing defect and layer separation becomes more comfortable; thus, the lowest resistance in front of stress raising obtained in T45 and T90 specimens. It should be noted that the highest transformation strain was obtained for T45 and C45 samples, which could be related to the formation of [110] texture in their microstructure.

Additionally, T45 presented the highest transformation strain of 5.31% in a low-stress regime (25-150 MPa) among all specimens. The active number of Correspondence Variant Pair (CVP) per grain can explain the different strain distribution in tension and compression. As the stress goes up, the active number of CVPs per grain increases, but the increase rate is higher in tension than compression. Therefore, it results in a larger number of active CVPs transforming in tensile loading than the compression. The high number of grains favorably oriented for transformation, risen the probability of transformation simultaneously, resulting in a larger transformation strain [55].

The volume fraction of oriented martensite initially increased with stress and then saturated. Moreover, plastic deformation increased with stress as well. Thus, the total strain was expected to increase [14]. Figure 4.5a shows that total strains increased with stress and then saturated after pass the 200 MPa in most of the samples. This saturation indicates that the material reached the maximum transformation strain at about 200 MPa. The T45 and T90 did not show saturation stress due to their low strength.

It should be noted that, in tension, two neighboring martensite variants, containing $\langle 011 \rangle$ type II twins, become (001) twin related to each other and reorient into one variant that is favorable to the applied stress, while in compression, the boundaries between two martensite plates are not twin related to each other [169, 170]. As a result, after tensile loading, there would be no sign of plastic deformation inside the twin bands, but only along with the variant interfaces, resulting in interfacial movement and plateau type deformation. On the other hand, after compressive loading, the high density of dislocation inside the twin bands results in no interfacial movement and a high stress-strain slope in the transformation region [171].

The results in Figure 4.5b illustrates that the relationship between stress and TTs is linear, which satisfied the Clausius–Clapeyron (CC) equation, i.e., $\Delta\sigma/\Delta T = \Delta H/T_0\epsilon_{tr}^{max}$ where $\Delta\sigma$, ΔT , and ΔH are the change in critical stress, temperature, and transformation enthalpy, respectively, T_0 is the equilibrium temperature and ϵ_{tr}^{max} is the maximum transformation strain [172]. The M_s and A_f temperature as a function of applied stress extracted from the thermal cycling results (Figure 4.4). Since the number of experiments was not good enough for T45 and T90, their CC-slope magnitudes are not trustable. This

figure could prove that changing BD situation has a negligible impact on the TTs of compressive samples since almost the same values were SLM obtained for all conditions. But in a tensile situation, although the same nominal stress was applied to the samples (at higher stress levels), the TTs had a little difference could be due to the difference in local stress distribution that governs the formation of martensite variants.

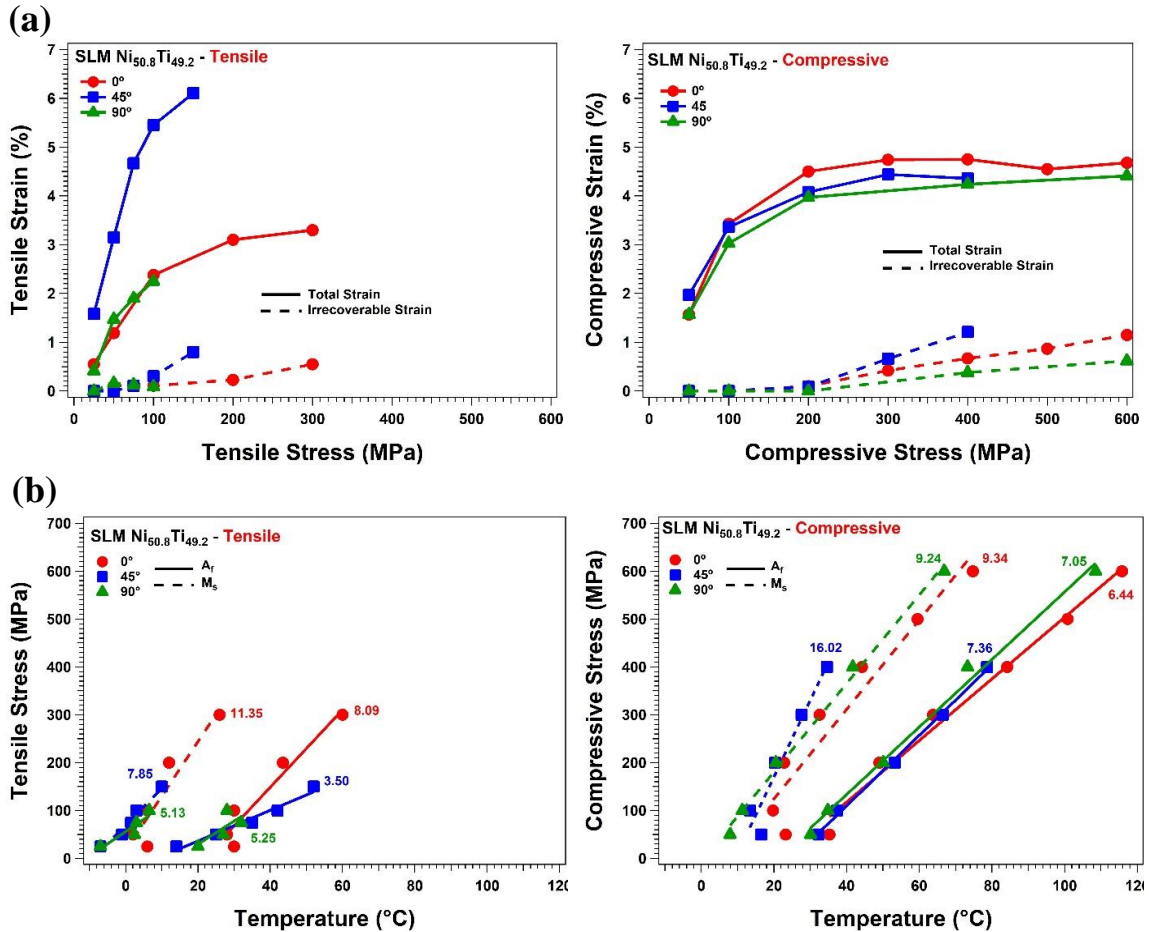


Figure 4.5 (a) The evolution of total strain and total irrecoverable strain with stress for tensile (left) and compressive (right) specimens. **(b)** The changes in TTs with stress for tensile (left) and compressive (right) specimens.

4.5 Superelastic Cycling

To investigate the cyclic response of the compressive samples, they are stress cycled between 5 and 800 MPa for ten cycles at $A_f^\sigma + 10$ °C and subsequently heated to 150 °C

(Figure 4.6). The C0 and C90 samples with [100] || LD texture show almost the same responses regarding the level of the stress plateau and recovery strain, while C45 sample with [110] || LD texture shows higher irrecoverable strain and lower recoverable strain. After heating, both C0 and C90 samples could recover all residual strain resulted from retained martensite locked into the NiTi matrix after each cycle. Due to the locked-in martensite and austenite slip, as the number of cycles goes up, the hysteresis decreases, the level of the stress-induced martensite goes down, and the plateau becomes steeper. All three samples show a stable recovery with no residual strain after ten cycles, indicating that mechanical cycling can be used as an effective training technique for L-PBF-AM-fabricated NiTi.

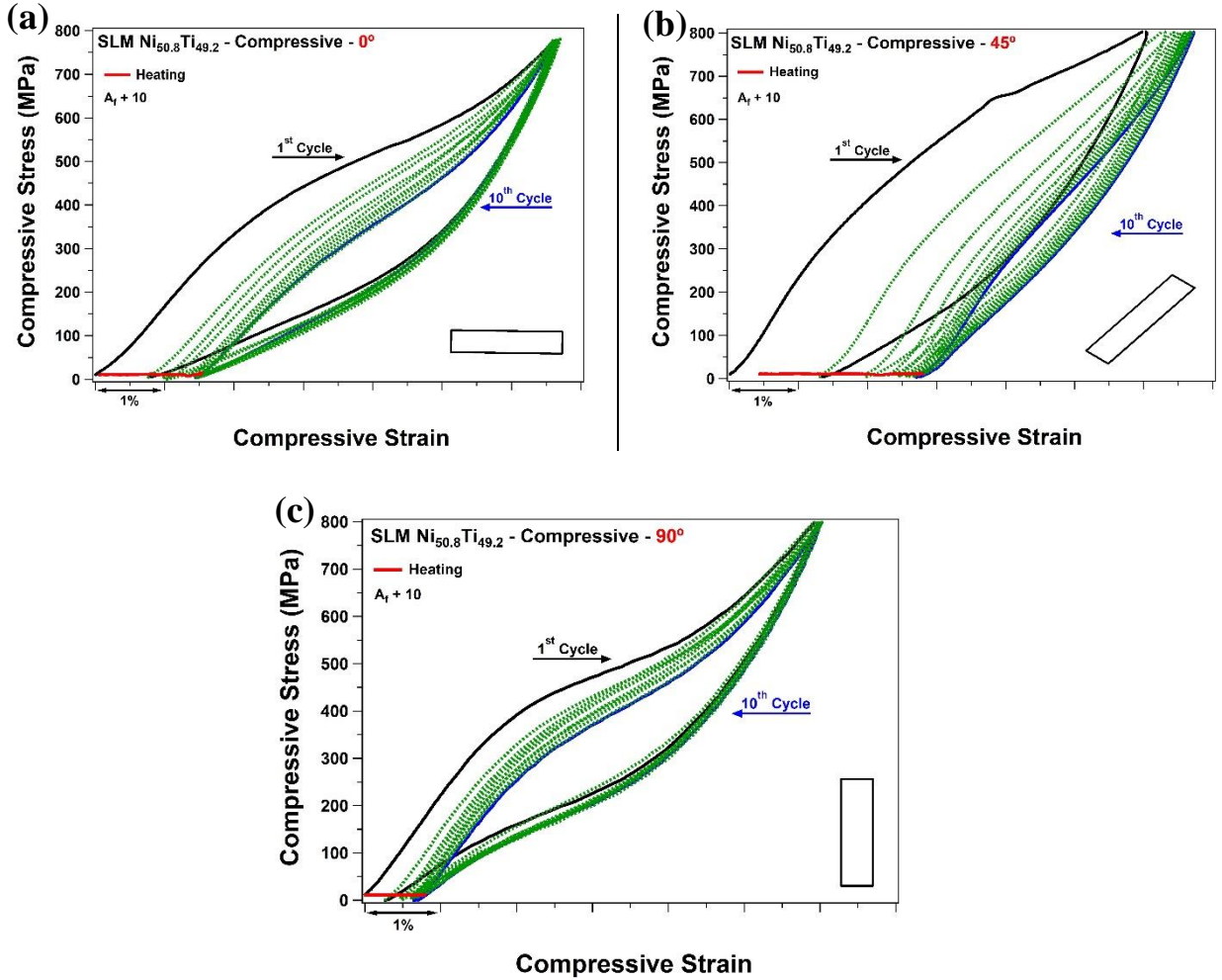


Figure 4.6 Superelastic cycling of L-PBF-AM NiTi under compression at $A_f^\sigma + 10$ °C for samples: (a) C0, (b) C45, and (c) C90.

Table 4.2 summarizes the mechanical response of samples at the first and 10th cycles of compression at $A_f^\sigma + 10$ °C. The total strain (ϵ_{tot} (%)), irrecoverable strain (ϵ_{irrec} (%)), recoverable strain (ϵ_{rec} (%)) and recovery ratio ($\epsilon_{rec}/\epsilon_{tot}$) are provided in this table. It should be noted that these selected values strongly depend on the testing temperature and loading stress levels. According to the results, C90 shows a promising 95.83% recovery ratio at the first cycle and a recoverable strain of 5.34 % after ten cycles. In C0 case, a lower recovery ratio of 88.40% was observed in the first cycle, in which 5.19% strain was stabilized after ten cycles. On the other hand, the C45 presents the poorest compressive

behavior among these samples, with a recovery ratio of 77.78% in the first cycle and a recoverable strain of 4.04% after ten cycles. The mechanical responses show a build orientation dependency of shape memory behavior of L-PBF-AM NiTi attributed to the various crystallographic texture resulting from altering BD in AM.

Table 4.2 Summary of cyclic test results of compressive L-PBF-AM Ni_{50.8}Ti_{49.2} SMAs.

L-PBF-AM Ni _{50.8} Ti _{49.2}	Max Applied Stress MPa	1 st Cycle				Before and After Heating (BH & AH)		10 th Cycle
		ϵ_{tot} (%)	ϵ_{irrec} (%)	ϵ_{rec} (%)	Recovery Ratio (%)	Total ϵ_{irrec} BH (%)	Total ϵ_{irrec} AH (%)	ϵ_{rec} (%)
C0	800	6.64	0.77	5.87	88.40	1.44	0	5.19
C45	800	6.03	1.34	4.69	77.78	2.69	0.45	4.04
C90	800	6.00	0.25	5.31	95.83	0.68	0	5.34

4.6 Discussion

As well-discussed in this chapter, the arrangement of samples on the substrate during fabrication could change the final texture of samples. Since the same PPs have been utilized to fabricate these samples, the same melting pool shape, thermal gradient direction, and cubic texture alignment were expected in all cases. In 0 and 90-degree cases, samples used the 90° symmetry feature of cubic crystal to show similar texture in [100] direction. In 45-degree specimens, although [100] texture has appeared in BD, LD, which was aligned with a diameter of cubic crystal, showed the [110] texture. Therefore, by adjusting PPs, which followed by altering melting pool shape and thermal gradient direction and/or by employing specific direction for building orientation (such as C45 sample in this study), it is possible to control the cubic crystal to fabricate sample with a specific strong orientation in BD and/or LD (such as C45 with [100] || BD and [110] || LD).

4.7 Conclusion

In this section, compression and tension NiTi samples were fabricated with the same PPs but different building orientations of 0, 45, and 90 degree concerning the substrate. Microstructure and thermomechanical properties were investigated, and the following conclusions are made:

- [001] texture align the BD is the preferred growth orientation in L-PBF-AM NiTi and therefore, a strong [001] || BD texture was observed for all of the conditions regardless of their BD.
- The BD plays a significant role in defining the mechanical properties and functional properties of SMAs. In this case, a strong [001] texture could be achieved along the BD, and through tilting the sample, a different texture, [110] || LD for the 45°, was achieved.
- [001] || LD textured samples showed similar mechanical properties with more than 5% of strain recovery. In comparison, the [110] || LD sample exhibited 4.04% stabilized compressive recovery strain with a higher amount of unrecovered strain even after the heating process upon ten cycles under 800 MPa of compressive load.
- The highest recoverable transformation strain was obtained for T45 with 5.31% samples under stress level 150 MPa, which had a good agreement with [110] orientation has formed along with LD.
- Tensile samples were more sensitive to adjusting the sample on fabrication palet compared to the compressive samples. Among tensile samples, the highest strength can be observed in T0 sample, where the LD is perpendicular to the BD, while T90 sample demonstrated the poorest response where the LD is perpendicular to the BD and a higher number of layers were involved in the fabrication.

5 Effect of Heat Treatment on L-PBF-AM and Conventional NiTi

SMA s are highly crystallographic orientation-dependent since higher strength and mechanical hysteresis was reported for conventional $\text{Ni}_{51.5}\text{Ti}_{48.5}$ and $\text{Ni}_{50.8}\text{Ti}_{49.2}$ single crystals [29, 32] compared to the polycrystalline one [173]. Due to displaying transformation under such high stresses and/or temperatures, the [100] orientation has shown to be preferable for NiTi. By introducing aging to [100] orientation, it was possible to obtain ultra-strong NiTi alloys [29, 32, 37]. It should be noted that the mechanical behavior of single-crystal materials was mimicked by highly textured polycrystalline ones fabricated by a conventional method [25]. The previous sections had shown that L-PBF-AM method could alter the texture of fabricated NiTi samples by controlling fabrication parameters, such as the appearance of strong [100] texture when 250 W laser power and 80 μm hatch spacing were implemented, the existence of strong [111] orientation by applying 100 W laser power and 40 μm hatch spacing, or utilizing 45-degree between BD and substrate to form [110] orientation in the fabricated samples.

One of the essential properties of SMA is its heat treatment history. Heat treatment is a very efficient method to control the TTs and improve the strength of Ni-rich NiTi alloys by precipitation [26, 44]. The heat treatment time, temperature, and cooling rate highly impact precipitation characteristics and the corresponding shape memory properties [28, 172, 174-177]. The chemical composition, volume fraction, and coherency of the formed precipitates impact the TTs, matrix strength, hardness, and martensitic morphology in Ni-rich NiTi alloys [146, 178-182]. As it is well known, lower TTs and higher strengths can be achieved by increasing the Ni-content of Ni-rich NiTi matrix [24, 29].

Nevertheless, L-PBF-AM was recently accepted for the fabrication of NiTi parts. The impact of aging on L-PBF-AM NiTi specimens has not been fully understood. Our group reported the effects of heat treatment at different temperatures, times, and prior and following solutionizing on Ni-rich L-PBF-AM NiTi samples fabricated by 250 W laser power and 120 μm hatch spacing, which did not have specific texture [86, 145, 183]. More studies are needed to demonstrate a higher stress and transformation strain to determine proper heat treatment for the L-PBF-AM NiTi. Hence, in the present chapter, L-PBF-AM $\text{Ni}_{50.8}\text{Ti}_{49.2}$ samples fabricated by 250 W laser power, 1250 mm/s scanning speed, and two hatch spacing of 120 (no specific texture) and 80 μm (sharp [100] texture) were selected to present the sensitivity of L-PBF-AM PPs. These samples will be abbreviated as ‘SLM120’ and ‘SLM80’ hereafter, respectively. The as-received ingot and as-fabricated L-PBF-AM samples will be called ‘as-fabricated’ in this study. The XY scanning strategy and 90-degree angle between BD and substrate were utilized. Additionally, the behavior of conventional NiTi was evaluated to demonstrate the power of L-PBF-AM manufacturing compared to the previous methods. To improve the microstructure and thermo-mechanical behavior of samples, specific heat treatment time (1.5 hr) and temperature (550 $^{\circ}\text{C}$) were chosen based on previous single crystal studies [29, 37] on NiTi in trying to mimic single crystal behavior of NiTi by AM. The heat-treated samples will be referred to as ‘aged’ throughout the text.

5.1 Stress-free transformation temperatures (TTs)

Figure 5.1 depicts the DSC results of as-fabricated and aged L-PBF-AM and ingot specimens. The results of as-fabricated SLM120 and ingot were extracted from our previous study [86]. Broader peaks and higher TTs occurred after the L-PBF-AM process

compared to the ingot, consistent with our previous studies [86, 183]. The TTs increases were due to Ni evaporation and/or formation of Ni-rich phases (such as Ni_4Ti_3 , Ni_3Ti_2 , and Ni_3Ti) within L-PBF-AM process, which caused matrix composition depletes in nickel [184, 185]. Therefore, microstructural areas with higher and lower Ni content resulted in broader DSC peaks [144] in as-fabricated L-PBF-AM.

By introducing aging to the samples, similar DSC responses were formed in all alloys. The DSC peaks of aged samples were sharper and shifted to higher temperatures compared with as-fabricated ones. Increasing TTs after aging was attributed to Ni-rich precipitates' formation [186]; thus, composition alteration becomes the main factor in the change of peak positions [183]. On the other hand, the appearance of Ni-rich participates could explain the existence of sharper peaks in aged specimens by making the microstructure of as-fabricated samples more homogenous with heat treatment. Moreover, two-stage transformation was observed during the cooling of aged samples. Based on the literature, heat-treated Ni-rich NiTi alloys usually show R-phase prior to $\text{B}19'$ (martensite phase), which caused to have two staged B2 (austenite phase)-R- $\text{B}19'$ transformation [1]. The appearance of R-phase, which has a martensite nature and trigonal lattice, is attributed to the formation of Ni_4Ti_3 precipitates during aging. Since these precipitates have a large lattice deformation, which results in strong resistance to the formation of $\text{B}19'$, the formation of R-phase with a smaller lattice deformation favors before the $\text{B}19'$ [50, 187, 188].

The enthalpies of aged specimens were close to 18 and ~ 9 J/g for $\text{B}19'$ -B2 and R- $\text{B}19'$ transformations, respectively. The R-phase peaks had an enthalpy of ~ 4 J/g in all aged

samples. The austenite finish temperature, A_f , was increased from 18, 30, and -6 °C for as-fabricated SLM80, SLM120, and ingot, respectively, to around 32 °C for all the aged specimens. This fact shows that the aged samples should be mixed phases at room temperature (24 °C) and in austenite phase at body temperature (37 °C). It should be noted that the DSC responses of aged SLM80 were approximately similar to the aged Ni₅₁Ti₄₉ single crystal ([100] orientation). As the martensite start, M_s , and A_f were -7 & 33 °C for aged single crystal NiTi ([100] orientation) and, were -11 & 32 °C for aged SLM80, respectively [189].

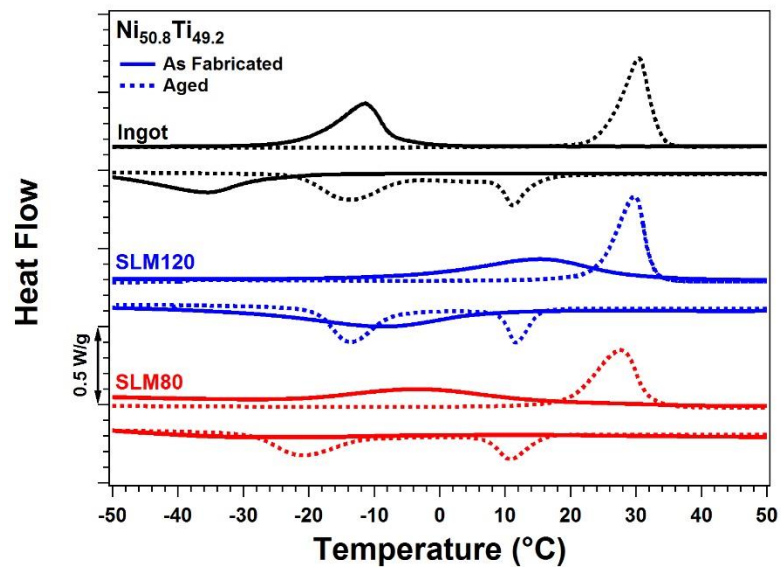


Figure 5.1 DSC responses of as-fabricated (Solid line) and aged (Dash line) ingot, SLM120, and SLM80 samples

5.2 Microstructure Analysis

Figure 5.2 shows the TEM images of microstructures of aged alloys. Microstructures of the as-fabricated L-PBF-AM samples were included from our previous study (Figure 5.2a, b) for comparison [103]. A combination of bright-field and Z-contrast (HAADF images) images highlights the precipitate morphology and orientation in the corresponding

matrix. All the aged samples show the presence of elongated and plate-shaped precipitate features in the matrix. It is noted that precipitates in the aged condition were oriented along a particular direction (Figure 5.2c-g) and go out of diffraction conditions simultaneously on a slight sample tilt. This suggests that the precipitates possess a specific orientation relationship with the matrix. In the aged ingot case, the microstructure showed an array of multiple twinned structures within a parent grain. The twins were parallel suggesting a single twin habit plane was active. The aspect ratio and area fraction of the precipitates, estimated by ImageJ, were about 0.35 (with Standard Deviation (SD) of 0.062) and 3.87% (SD: 2.23), respectively. The inset in Figure 5.2c shows the [001] zone axis diffraction pattern from the matrix of aged ingot. Since B2 structure is an interpenetrating simple cubic lattice, the presence of $\langle 100 \rangle$ spots in the [001] diffraction pattern indicates ordered lattice. However, the absence of (100) super lattice spots in the [001] zone axis pattern implies that the matrix is not an ordered B2 structure. Lattice parameter of the matrix calculated from the diffraction spots is 4.2194 Å. This value agrees closely with the previous literature [190].

In the aged cases, the calculated precipitate area fractions were 2.4% (SD: 1.92) and 2.37% (SD: 1.12), respectively, and the aspect ratios of the precipitates were estimated to be 0.20 (SD: 0.041) and 0.29 (SD: 0.093), respectively. Similar to the aged ingot, the absence of superlattice spots in the $[\bar{1}12]$ diffraction pattern of the aged SLM120 (inset in Figure 5.2d) implies that the aged matrix was disordered. Lattice parameter of the matrix in SLM120, calculated from the diffraction spots, is 4.254 Å. In addition to precipitates, micropores, visible as dark spherical and elongated morphologies in the Z-contrast images (Figures 2e, g), were present in the aged SLM120 and SLM80 microstructures. The

presence of pores could be attributed to gas entrapment or Ni evaporation in the fabrication process. However, no such features were observed in the aged ingot specimen.

By comparing the aged and as-fabricated L-PBF-AM TEM results, it could be concluded that precipitates of different sizes were formed during the aging treatment. Although no Ni_4Ti_3 precipitates were reported in as-fabricated conditions [103], the chemical analyses performed on the precipitates in the aged microstructures, using energy dispersive spectroscopy, confirms that the precipitates were Ni-rich and the composition was close to Ni_4Ti_3 (Figure 5.2h). This observation is in good agreement with the appearance of R-phase in DSC results of aged specimens. The Ni_4Ti_3 precipitates are considered to be formed very rapidly during water quenching due to the high excess of Ni in the austenite matrix.

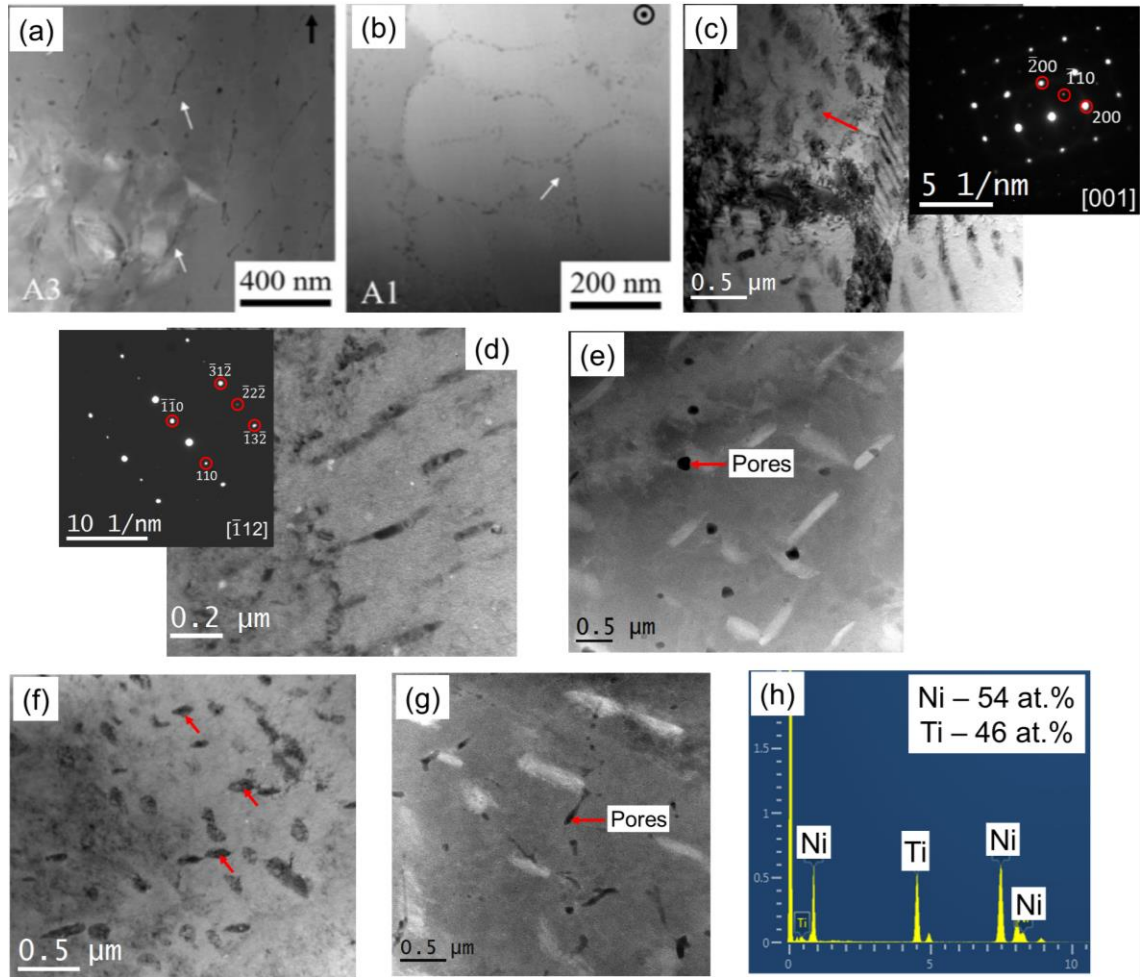


Figure 5.2 Bright field and Z-contrast TEM images of as-fabricated and aged L-PBF-AM alloys. (a) as-fabricated SLM120. (b) as-fabricated SLM80 ((a) and (b) adopted from Ref. [103]). (c) bright field image of aged ingot. Inset shows the [001] diffraction pattern of the matrix. (d) bright field image of aged SLM120. Inset shows the $[\bar{1}12]$ diffraction pattern of the matrix. (e) Z-contrast image of aged SLM120. (f) bright field image of aged SLM80. (g) Z-contrast image of aged SLM80. (h) Representative EDS spectrum of a precipitate. Arrows show precipitate and pore features.

5.3 Load-biased shape memory behavior

In order to characterize the strain recovery and shape memory actuation response, the as-fabricated (solid line) and aged (dash line) samples were thermally cycled between a temperature below the M_f and a temperature above the A_f under constant compressive stresses. After the cycle was completed, the stress was increased to the next level and

thermal cycling repeated. This process was continued until significant plastic strain was accumulated (Figure 5.3). The results of as-fabricated SLM120 and ingot were extracted from our previous study [86].

Figure 5.3a depicts the shape memory behavior of ingot. There was the typical stress effect on transformation temperature, with the M_s increasing from -5 to 3 °C when the stress was increased from 50 to 300 MPa for the as-fabricated ingot. Similarly, the M_s was 15 °C at 50 MPa and increased linearly to 40 °C at 400 MPa for aged ingot. The transformation strain of ingot sample was decreased after aging. A maximum recoverable strain of 3.54% and 2.85% at 200 MPa was observed for as fabricated and aged ingot, respectively. Moreover, the thermal hysteresis was increased from 22 to 34 °C when stress level raised from 50 to 300 MPa for as-fabricated ingot, while the same trend but lower thermal hysteresis of 17 °C under 50 MPa and 23 °C under 400 MPa °C were achieved by introducing aging to the ingot sample.

Figure 5.3b illustrates the shape memory response of SLM120 before and after aging. By changing the fabrication process to L-PBF-AM, higher TTs appeared, which have a good agreement with DSC results. As the stress level increased from 50 to 300 MPa, the M_s also raised from 9 to 20 °C for as-fabricated SLM120. Similar to the ingot sample, the M_s values increased after aging, as 17 °C at 50 MPa and 66 °C at 500 MPa were observed. The as-fabricated and aged SLM120 sample showed almost the same recoverable and irrecoverable strains. The maximum recoverable strain of 3.54% and 3.78% were achieved under 200 MPa before and after aging, respectively. It should be noted that only the recoverable strain of aged SLM120 was higher than aged ingot, and the other strains were

almost similar after and before aging. The same as ingot, this heat treatment made the thermal hysteresis of SLM120 decrease. Although thermal hysteresis of SLM120 had a negligible difference with ingot before aging, it started from below ingot value with 13.75 °C at 50 MPa and reached above ingot values by 30.6 °C at 500 MPa after aging.

The shape memory response of SLM80 (Figure 5.3c) showed a larger temperature window than the other specimens, as the M_s was increased from -1.5 to 99 °C before aging, and 17 to 133 °C after aging when stress was increased from 50 to 1000 MPa. Moreover, stronger shape memory behavior was achieved by decreasing hatch spacing to 80 μm in SLM80 sample, since a maximum recoverable strain of 3.77% and 4.07% at 600 MPa were attained before and after heat treatment, respectively. Additionally, the irrecoverable strain of as-fabricated and aged samples appeared at stress levels higher than 200 MPa for SLM120 and ingot, and 600 MPa for SLM80. In thermal hysteresis case, whereas SLM80 had similar thermal hysteresis values of 17.5 °C at 50 MPa and 25.6 °C at 1000 MPa before and after aging, respectively, smaller values under other stress levels (100-800 MPa) were obtained for aged SLM80 compared to as fabricated one. It worth mentioning that thermal hysteresis of SLM80 had the lowest values and alternation by aging among all the samples.

As was expected, the TTs were increased by applying higher stresses in all specimens. On the other hand, this heat treatment shifts the TTs to higher values, which is attributed to the formation of Ni-rich precipitates and alters the thermal hysteresis to lower numbers. Furthermore, during thermal cycling, triangular shape behavior was observed on cooling under low-stress levels, resulting from two-stage (B2-R-B19') transformation. This extra transformation is expected in Ni-rich NiTi with Ni_4Ti_3 precipitates [191]. The austenite to

R-phase TTs are almost stress independent, while austenite to martensite TTs are highly stress dependent, thus by increasing stress levels, martensite TTs increased above R-phase TTs, R-phase transformation disappears and more symmetric shape memory response appeared [28].

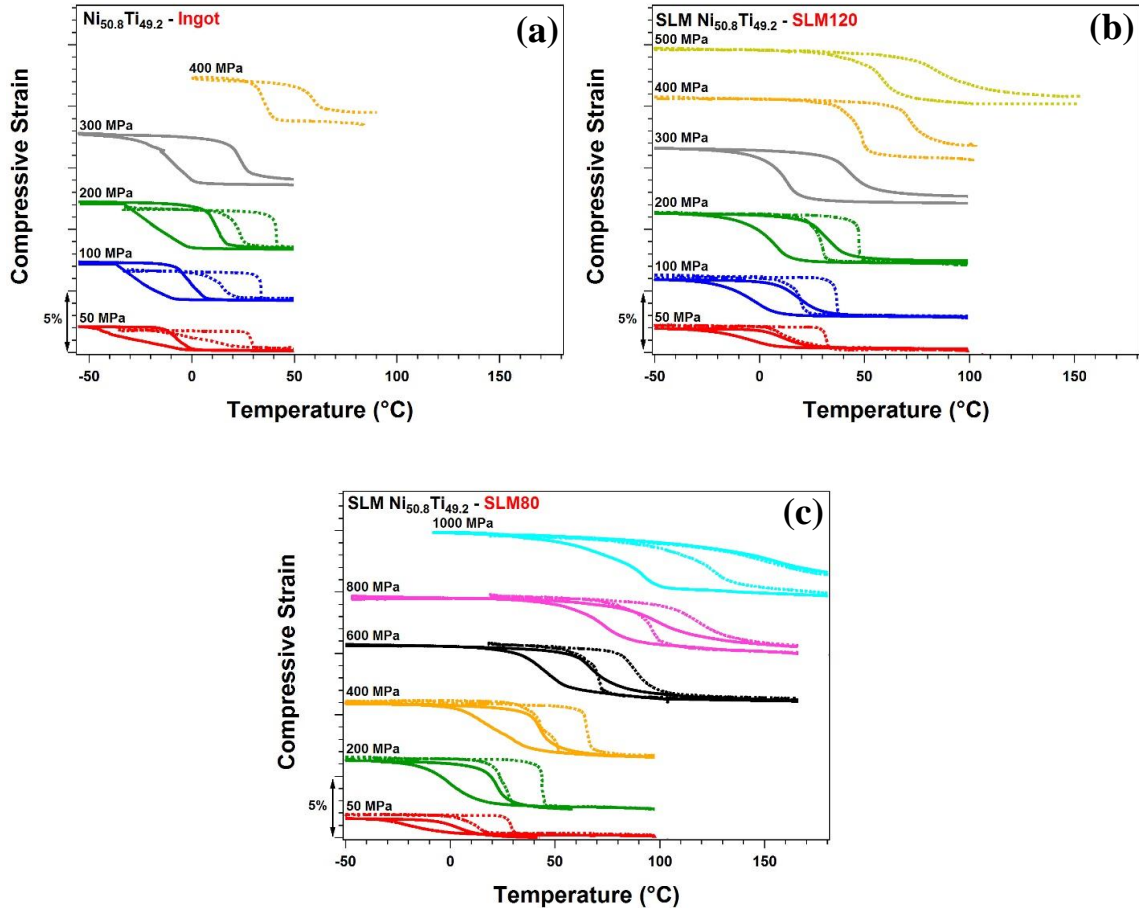


Figure 5.3 Thermal cycling under constant stress levels of (a) Ingot, (b) SLM120, and (c) SLM80 for as-fabricated (solid line) and aged (dash line) samples.

5.4 Failure response at body temperature

Figure 5.4 illustrated the failure results of as-fabricated (solid line) and aged (dash line) samples at 37 °C. Samples were initially loaded elastically at austenite phase and then followed by austenite to martensite phase transformation. Then by applying higher stresses,

specimens deformed elastically in martensite phase until plastic deformation and failure. Critical stresses were similar for all samples, as the difference of failure test and M_s temperature were almost the same. Since As-fabricated ingot had a lower M_s temperature than others, higher critical stress was observed for this specimen. Hence this critical stress was close to the yield stress of as-fabricated ingot, the plateau behavior did not appear.

It should be noted that the ductility of samples decreased by changing the manufacturing process from conventional to L-PBF-AM. Additionally, by altering hatch spacing in L-PBF-AM process, a brittle behavior was observed for SLM80. NiTi ductility decreases as the Ni-rich precipitate size shrink and coherency increases. Moreover, sample texture has a significant impact on the mechanical and fracture response, as brittle behavior was reported for single crystal in [100] orientation and more ductile response for other orientations (such as [110] and [111]) [192, 193]. It is worth mentioning that not only smaller and more coherence precipitates were observed in SLM80 but also stronger [100] texture was reported for SLM80 compared to SLM120 in our previous study [103], which could explain the sudden rapture of SLM80.

The strength of SLM80 was a bit higher than others before aging. As desired, the heat treatment improved the strength of all three samples and postponed the ultimate stress significantly for SLM120 and reasonably for SLM80 and ingot samples to ~1700 MPa for all of them. This improvement is attributed to precipitation hardening.

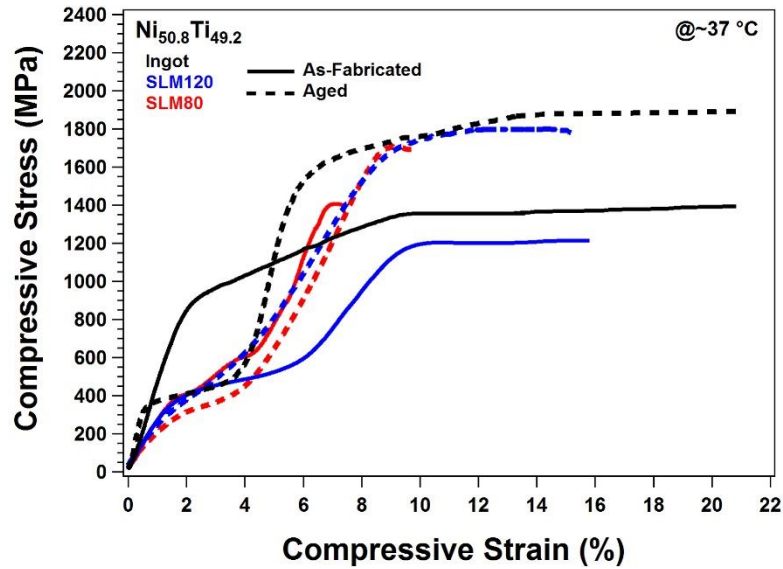


Figure 5.4 Failure responses of As-fabricated (Solid line) and Aged (Dash line) samples.

5.5 Compressive response at selected temperatures

The superelastic responses of as-fabricated (Left) and aged (Right) samples under compression at selected test temperatures above A_f were plotted in Figure 5.5. The material was loaded to a strain value of 1% in the first cycle and then unloaded. In succeeding cycles, the applied strain was incrementally increased by 1% (until a maximum applied strain of 3% for as-received ingot and 4% for aged ingot, 6% for all as-fabricated and aged SLM120, and 7% for aged SLM80 were reached).

Figure 5.5a illustrates the stress-strain response of ingot at selected temperatures. As-received ingot showed residual strain at all strains and temperatures. In order to check how much recovery could be related to martensite reorientations, a heating process was done upon unloading 3% total strain. Heating could not fully recover the strains and an irrecoverable strain of 0.28% at 40 °C, which increased to 0.79% at 75 °C, was obtained. Since it was showed in failure results (figure 4), superelastic plateau could only appear

after introducing aging to the ingot sample. Aged ingot specimen showed partial superelasticity at 1-4% total strains, which mostly recovered by heating the sample at 40 and 55 °C. By increasing the testing temperature, existed residual strain did not fully recover by heating and increased from 0.49% at 75 °C to 1.07% at 95 °C.

Superelastic behavior of SLM120 depicts in Figure 5.5b. The transformation strain of as-fabricated SLM120 was fully reversible with a negligible amount of irrecoverable strain (<0.3%) when the loaded strain was less than or equal to 4%. This sample showed partial superelasticity in 6% at all temperatures and even in 5% strains at temperatures higher than 75 °C. At 40 °C, the irrecoverable strain was 0.49% and it expanded to 0.99% at 115 °C after unloading 5% total strain. As was expected from the failure test (Figure 5.4), the ductile behavior helped this sample to avoid sudden rupture, and obvious plasticity (2% residual strain) appeared under 6 % at 115 °C. By introducing the heat treatment to the sample, significant improvement was observed in superelastic behavior. While aged SLM120 sample mostly full recovered even in 6% until 115 °C (irrecoverable strain less than 0.4%), which was a good development for this sample, the plasticity showed up again at higher temperatures for 6% strains, and the test was done at 135 °C with 1.1% residual strain. Additionally, two-stage transformation (B2-R-B19') was observed at lower temperatures (40 and 55 °C) here, which were appeared in DSC and shape memory behavior results before inducing martensite, too.

Figure 5.5c demonstrates superelastic behavior of SLM80 at different temperatures. As-fabricated SLM80 presented perfect superelastic behavior (with irrecoverable strain less than 0.1% only at 6% strains and higher temperatures) at all temperatures (40 to 95

°C). It fractured at 95 °C, in 6% strain and 1115 MPa stress, which was in good agreement with the failure results shown in Figure 5.4, where it was the most brittle of all the samples. By adding aging, the strength of this sample improved and postponed the failure to 7% strain and 1315 MPa stress at 135 °C. A remarkable feature observed in Figure 5.5 was the very high strength of aged SLM80 sample, which results in perfect superelastic behavior with negligible plastic deformation (less than 0.2%) under compressive loads up to ~1200 MPa and 6% strain at 135 °C. To the best of our knowledge, this is the highest stress level under which a fully reversible shape memory strain (even at 7% strain) has been obtained for L-PBF-AM NiTi.

As it was expected, the critical stress to induce martensite phase was increased by increasing temperature, while it was decreased by introducing heat treatment to the samples. Moreover, this aging not only improved the strength of specimens but also expanded superelastic windows of them. The highest superelastic window was around 100 °C, which belonged to the aged SLM80. Additionally, an increasing trend observed in stress hysteresis of ingot and SLM120 by rising temperature which could be related to greater plastic deformation existed at higher temperatures. In contrast, stress hysteresis of SLM80, which showed perfect recovery upon unloading, decreased by increasing temperature. The stress hysteresis trends have a good agreement with thermal hysteresis calculated from shape memory behavior of specimens.

It should be noted that using AM instead of conventional methods improved the superelastic behavior of NiTi samples. By comparing the superelastic behavior of L-PBF-AM samples, it can be concluded that lower hatch space sample (SLM80) followed by this

heat treatment (500 C for 1.5 hr.) can easily improve the shape memory response of L-PBF-AM NiTi, which could be attributed to the formation of different texture during fabrication of these specimens and precipitation hardening within the aging process.

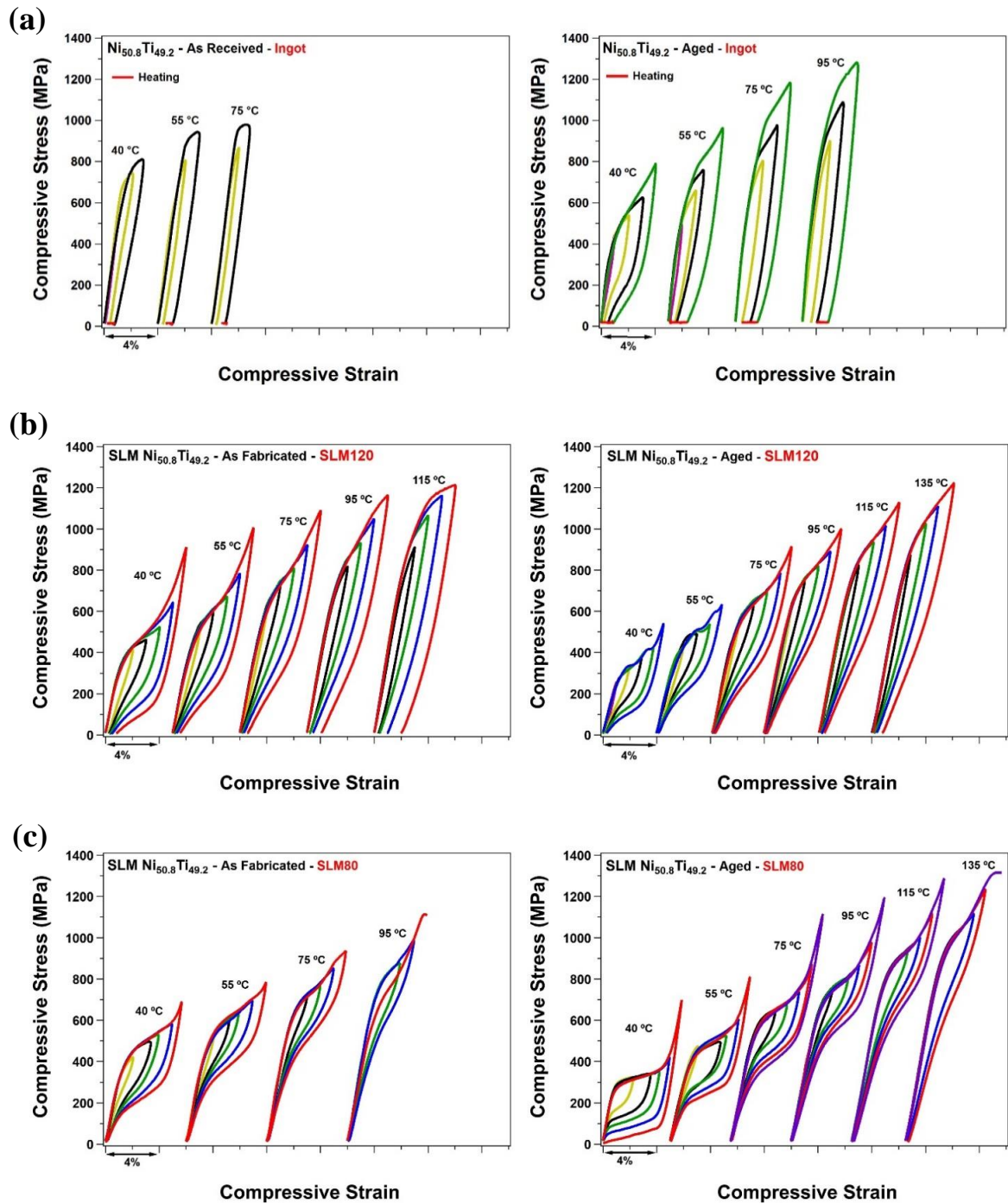


Figure 5.5 Superelastic responses of As-fabricated (Left) and Aged (Right) samples of (a) Ingot, (b) SLM120, and (c) SLM80.

5.6 Discussion

5.6.1 Transformation Strain and Thermal Hysteresis

Figure 5.6a illustrates the recoverable and irrecoverable strains of the as-fabricated and aged specimens as a function of compressive stress, analyzed from the thermal cycling experiments presented in Figure 5.3. The minimum recoverable strain appeared at the lowest applied stress level (~1.5 % at 50 MPa) for all sample conditions. This is not surprising as the transformation strain results from the evolution of martensite variants as a function of external stress. By increasing stress level, the amount of oriented martensite increased and, so did the recoverable strain. The increase in recoverable strain saturated for most cases around 200 MPa as the fraction of preferred martensite variants approaches 100%. Eventually, irrecoverable strain showed up in higher stress levels due to the existence of plastic deformation during the martensite transformation, which cannot be recovered and thus decreased the recoverable strain.

In the case of as-fabricated (solid line) ingot and SLM120, the maximum recoverable strains were 3.47% and 3.55%, respectively, at 200 MPa. By introducing heat treatment (dash line) to the samples the maximum recoverable strain of ingot was decreased to 2.85%, while it was increased to 3.87% for SLM120 at 200 MPa. The SLM80 sample presented the strongest behavior with 3.68% and 3.9% recoverable strain at 200 MPa, which maximized to 3.77% and 4.07% at 600 MPa before and after aging, respectively.

It is worth noting that the L-PBF-AM fabrication depicted stronger shape memory behavior in compression with the conventional method, which could result from formation stronger texture during the L-PBF-AM fabrication process. The actuation response of ingot

could not even improve after aging, which would be attributed to the formation of more obstacles such as larger precipitates during heat treatment, which make the nucleation and growth of martensite difficult, and ended with lower recoverable strain. While the appearance of coherence precipitates was the important factor to improve the shape memory behavior of L-PBF-AM specimens after aging. Additionally, significant impact of L-PBF-AM PPs could be quickly revealed by comparing the shape memory behavior of SLM120 and SLM80, while only changing 40 μm in hatch spacing resulted in a stronger texture and higher resistance against deformation for SLM80, regardless of sample condition.

Hysteresis is the energy dissipated within martensitic transformation, which contains frictional energy due to resistance to the movement of phase boundaries and the dissipation of elastic strain energy. The total energy dissipation is reflected in the thermal or stress hysteresis. Hysteresis depends on strength, orientation, and twinning types. It should be noted that higher hysteresis (higher energy dissipation) is a negative factor in SMA actuator type applications.

The thermal hysteresis was measured between the midpoint of transformation strains during heating and cooling processes (Figure 5.3) and depicted in Figure 5.6b. The behavior of Ingot and SLM120 samples was almost the same, as their temperature hysteresis was raised from ~ 20 $^{\circ}\text{C}$ to ~ 35 $^{\circ}\text{C}$ for as-fabricated, and from ~ 15 $^{\circ}\text{C}$ to ~ 25 $^{\circ}\text{C}$ for aged specimens. While for the strongest sample (SLM80), the temperature hysteresis changed from ~ 17 $^{\circ}\text{C}$ to 25 $^{\circ}\text{C}$.

An increasing trend was observed for temperature hysteresis of all conditions with increasing the stress level attributed to the appearance of plastic deformation in higher stress levels. As was expected the strongest sample with higher resistance against plastic deformation showed lower thermal hysteresis values and changes. It is worth noted that the heat treatment made the temperature hysteresis lower than as-fabricated and almost similar for all aged samples. This decrease could be related to the friction dissipation due to precipitates. Thus, by aging the samples, less variant and less friction involved during transformations cause low energy dissipation, which leads to obtaining smaller hysteresis [194].

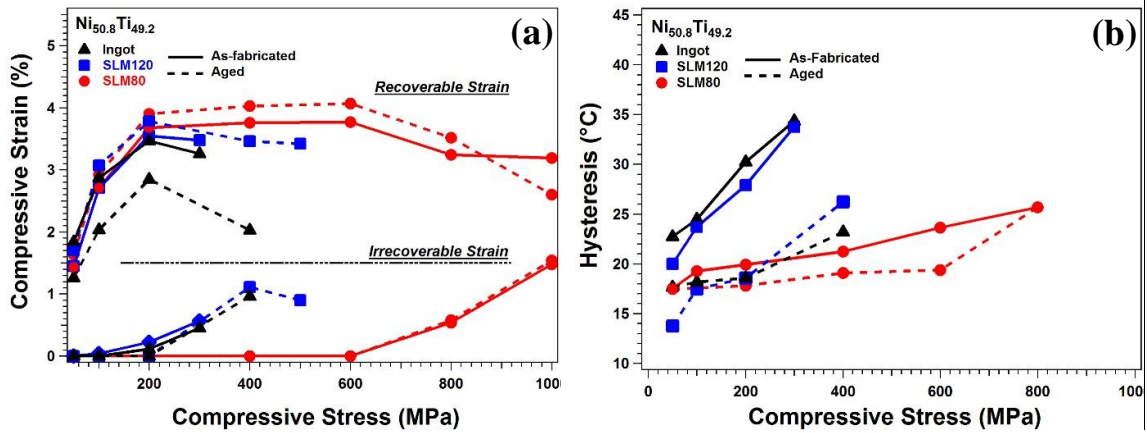


Figure 5.6 (a) Recoverable and irrecoverable strains, and (b) thermal hysteresis vs compressive stress of as-fabricated (solid lines) and aged (dash lines) specimens.

5.6.2 Clausius–Clapeyron relationship and Work Output

Figure 5.7 illustrates the M_s temperature as a function of applied stress extracted from the thermal cycling results (Figure 5.3). The results indicated that M_s increases linearly with stress. This linear relationship satisfies the Clausius–Clapeyron (CC) relation, i.e.

$$\frac{\Delta\delta}{\Delta T} = - \frac{\Delta H}{T_0 \varepsilon_{tr}^{max}}$$

where $\Delta\sigma$ is the change in the critical stress, ΔT is the change in

temperature, ΔH is the transformation enthalpy, T_0 is the equilibrium temperature, and ϵ_{tr}^{max} is the maximum transformation strain.

Based on this relation, the CC slope of as-fabricated ingot, SLM120, and SLM80 were 18.86, 19.15, and 8.88 MPa/°C, respectively. Since the number of experiments was not good enough for ingot and SLM120, these magnitudes are not trustable. However, the SLM80 has the lowest CC slope consistent with the highest transformation strain achieved for this sample. By introducing aging to the specimens, CC slopes decreased to 14.24, 9.34, and 8.16 MPa/°C for ingot, SLM120, and SLM80, respectively. By comparing the CC slopes, it can be concluded that the L-PBF-AM samples were less sensitive to the stress alternation. It should be noted that M_s was increased by introducing aging to the samples, regardless of the fabrication process. Moreover, M_s values are close to each other for aged specimens with a good agreement with DSC results.

Work output is an essential factor to compare the actuator performance among various SMAs. In this study, it was calculated by simply multiplying the recoverable strain by the applied stress obtained from the thermal cycling results (Figure 5.3). The maximum work output was decreased from 6.94 to 5.7 J.cm⁻³ for ingot. While SLM120 and SLM80 had an increasing trend from 7.1 to 7.74 J.cm⁻³ and from 22.62 to 24.22 J.cm⁻³, respectively. As the recoverable strain and applied stress of SLM80 were the highest among these specimens, it was expected to get the highest work output from this sample.

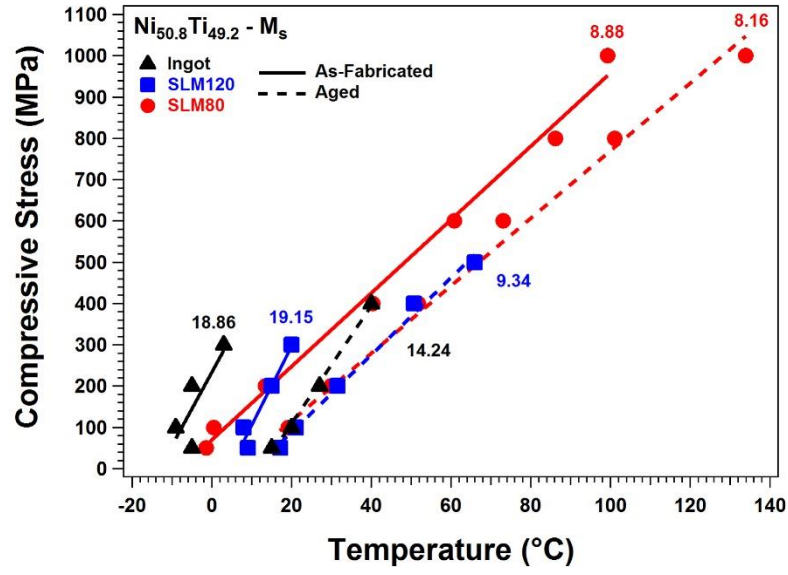


Figure 5.7 The critical stress versus Ms temperatures of As-fabricated (solid line) and Aged (dash line)

5.6.3 Superelastic Temperature Window, Recovery Ratio, and Stress Hysteresis

The superelastic temperature window is dependent on yield strength, thermal hysteresis, and CC slope. Based on the criteria of Liu and Galvin [195] for NiTi superelasticity, the superelastic temperature window can be written as [182]:

$$T_{SE} = \sigma_y / \frac{\Delta\delta}{\Delta T} - (A_f - M_s) \quad \text{Eq. 5.1}$$

where T_{SE} is the superelastic temperature window, σ_y is the austenite yield strength, and $(A_f - M_s)$ is the thermal hysteresis.

By analyzing the data of Figure 5.5, it was observed that L-PBF-AM samples had a higher superelastic temperature window than conventional ones. As they had almost the same yield stress, the reason for this difference could be explained by lower CC-slope of L-PBF-AM samples. By introducing aging to the alloys, the superelastic temperature

window was increased by 20 °C for ingot and SLM120, and by 40 °C for SLM80. It is cleared in Eq.1 that yield stress and hysteresis have a direct impact on superelastic temperature window. Since the aging increased the austenite yield stress (based on failure test in Figure 5.4) and decreased the hysteresis, this rising trend was understandable for superelastic temperature window.

However, aged SLM80 showed the highest superelastic temperature window, which attributed to the formation of coherent precipitate inside its microstructure (Figure 5.2) and made its transformation strain larger than others (Figure 5.6a), ended with the lowest CC-slope and hysteresis (Figure 5.7 & Figure 5.6b), and resulted in the highest superelastic temperature window (100 °C). It worth mentioning that the yield stress generally diminishes and critical stress increases by increasing test temperature; thus, the critical stress for phase transformation reaches the yield strength over a smaller temperature range. By considering these facts, as-fabricated ingot with higher TTs and steep CC slope reasonably exhibited the lowest superelastic temperature window (35 °C).

Figure 5.8a demonstrates the superelastic recovery ratio versus temperature of all sample conditions. The recovery ratio is the proportion of recovered to total strain extracted from 3% and 5% strains of ingot and L-PBF-AM specimens at tested temperatures, respectively (Figure 5.5). In ingot case, the recovery ratio had a decreasing trend by increasing temperature. The maximum recovery ratio was diminished by introducing aging to the sample from 73.5 % at 40 °C to 65.87 % at 55 °C for ingot. Since plastic deformation existed at higher temperatures for SLM120, the recovery ratio was decreased at higher temperatures. However, the maximum recovery ratio increased by aging for this alloy from

91.05 % to 97.37 % at 55 °C. As was revealed through this paper, SLM80 was the strongest alloy among them and showed almost 100 % recoveries upon unloading in most of the temperatures, regardless of the sample condition. This could show the significant impact of fabrication parameters and coherent precipitates again on the shape memory response of L-PBF-AM SMAs.

The stress hysteresis, which is a determinant factor for damping properties, was graphically evaluated from the data in Figure 5.5 as the difference between the loading and unloading curves at the mid-point of the plateau strain (3% for ingot and 5% for L-PBF-AM specimens) and presented at Figure 5.8b. The stress hysteresis of as-received ingot could not be determined accurately because of the existence of large plastic deformation. For the aged ingot, stress hysteresis was 425 MPa at 40 °C and 400 MPa at 95 °C. It was 380 MPa at 40 °C and 460 MPa at 115 °C for the as-fabricated SLM120 sample. The stress hysteresis dropped by introducing aging to the SLM120 sample and was 215 MPa at 40 °C and 340 MPa at 135 °C. It should be noted that the mechanical hysteresis of ingot increased first and then decreased, but SLM120 had a continuously increasing trend by applying higher temperatures. However, in both cases, a good agreement with their recovery ratio behaviors was observed, which presents the direct impact of plastic deformation on stress hysteresis. For SLM80 samples, as aging did not alter the recovery ratio, the same value and behavior were obtained for stress hysteresis before and after heat treatment. It was 275 MPa at 40 °C and was decreased to 165 MPa at 95 °C, then saturated around this value till 135 °C. Generally, the difference in stress hysteresis can be attributed to a change in the compatibility of the transforming phases and/or martensite morphology. Better

compatibility between the transforming phases resulted in less energy dissipation or hysteresis [196]. Moreover, compatibility depends on the lattice parameters of the transforming phases, which are subsequently dependent on matrix composition and temperature [197]. In this study, the manufacturing method and employed PPs followed by aging and testing temperature altered the lattice parameters and the matrix composition to improve the compatibility of transformation and finally decreases the stress hysteresis or energy dissipation to introduce a superalloy such as SLM80.

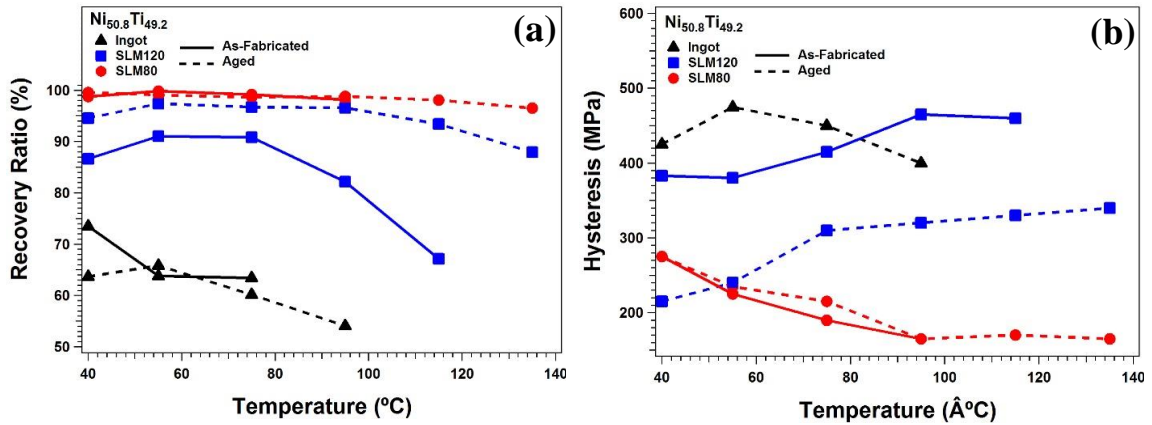


Figure 5.8 (a) Recovery ratio and (b) stress hysteresis versus temperature for as-fabricated (solid line) and aged (dash line) samples.

5.6.4 Comparison to other NiTi

It is worth comparing the results of SLM80 with alloys reported previously on single and poly crystal NiTi shape memory. Previous literatures reported M_s and A_s of -37 and 11 $^{\circ}C$, respectively, for single crystal $Ni_{51.5}Ti_{48.5}$ (at %) in aged (550 $^{\circ}C/1.5$ hr) condition [29], -7 and 27 $^{\circ}C$ for single crystal $Ni_{51}Ti_{49}$ (at %) in aged (500 $^{\circ}C/1.5$ hr) condition [189] and -33 and 7 $^{\circ}C$ for single crystal $Ni_{50.8}Ti_{49.2}$ (at %) in aged (550 $^{\circ}C/1.5$ hr) condition [32]. Maximum recoverable compressive strains of 5.6%, 3.5%, 4.2% and 2.5% along [148], [112], [100] and [111] orientations, respectively, were reported for single crystal

$\text{Ni}_{50.8}\text{Ti}_{49.2}$ in aged (550 °C/1.5 hr) condition [32], 3.45, 2.78, 2.11 and 2.98 % were presented in [100], [011], [111] orientations, for $\text{Ni}_{51}\text{Ti}_{49}$ and polycrystalline $\text{Ni}_{50.8}\text{Ti}_{49.2}$, respectively, in aged (500/ 1.5 hr) condition [37], and 4.3, 3.6 and 3 % along the [100], [110] and [111] directions, respectively, were reported for single crystal $\text{Ni}_{50.8}\text{Ti}_{49.2}$ in aged (500 °C/1.5hr) [198]. Thermal hysteresis decreased from 37, 36 and 39 °C to 15, 24 and 19 °C (before existence of plasticity) along [001], [011] and [111] orientations, respectively, for $\text{Ni}_{51}\text{Ti}_{49}$ and increased from 24 to 66 °C for polycrystalline $\text{Ni}_{50.8}\text{Ti}_{49.2}$ aged (500/ 1.5 hr) condition [37]. CC slope of 9.3 and 7.5 MPa/°C were calculated along [111] and [110] orientations, respectively, for single crystal $\text{Ni}_{51.5}\text{Ti}_{48.5}$ (at %) in aged (550 °C/1.5 hr) condition [29], and 7.7, 11.8, 12.8 and 8.8 MPa/°C were achieved in [100], [011], [111] orientations, for $\text{Ni}_{51}\text{Ti}_{49}$ and polycrystalline $\text{Ni}_{50.8}\text{Ti}_{49.2}$, respectively, in aged (500/1.5 hr) condition [37]. Superelastic with recoverable compressive strains of 3.3%, 3.7% and 3% along [001], [110] and [111] orientations, respectively, were reported for single crystal $\text{Ni}_{51.5}\text{Ti}_{48.5}$ in aged (550 °C/1.5 hr) condition [198]. Partial superelasticity was observed at 4% strain along [011] and [111] directions of single crystal $\text{Ni}_{51}\text{Ti}_{49}$, and polycrystalline $\text{Ni}_{50.8}\text{Ti}_{49.2}$, while perfect superelastic behavior upon unloading of 7% strain was presented for single crystal $\text{Ni}_{51}\text{Ti}_{49}$ along [100] direction in aged (500/1.5 hr) condition [37]. Superelastic temperature window of 170 °C (between 0-170 °C) was reported for single crystal $\text{Ni}_{51.5}\text{Ti}_{48.5}$ along [100] direction in aged (550 °C/1.5 hr) condition [29] and 140 °C (between 40-180 °C) for single crystal $\text{Ni}_{51}\text{Ti}_{49}$ (at %) along [100] direction aged in (500 °C/1.5 hr) condition [37].

The present study has shown that aged SLM80 sample had M_s and A_s of -7 and 20 °C, respectively. The maximum recoverable compressive strain was 4.07 %, thermal hysteresis

was almost constant and around 19 °C before the existence of plasticity and CC-slope was 8.16 MPa/°C. Finally, perfect superelastic behavior was presented for this alloy till 7% strain and a superelastic temperature window of ~100 °C (between 40-135 °C) achieved. It should be noted that the highest work output reported for NiTi is less than 20 J/mm³, while high work output of 24.22 J.cm⁻³ was obtained in this study, which closes to work output of high-temperature SMAs such NiTiHf [146]. By comparing these results with other NiTi, it could be concluded that aged SLM80 has similar TTs, irrecoverable strain, thermal hysteresis, CC-slope, and superelastic behavior with only lower temperature window with aged single crystal along [100] direction which has a good agreement with our texture study presented before [103]. Thus it is correct to say that it could be possible to mimic the single crystal behavior using AM methods and adding heat treatment as post-processing. But keep in mind that changing fabrication parameters, such as hatch spacing in this study, and heat treatment elements could easily change the final response of SMAs.

Additionally, as SLM80 can show perfect superelastic behavior at body temperature, it will be a good choice for biomedical applications, especially as a bone implant. In our previous studies, different porosity levels (32 to 72 %) and unit cells (from simple cubic to triply periodic minimal surface (TPMS)) were combined with numerical studies, which resulted in finding the suitable porosity level of 69% and structure of TPMS Diamond to mimic human bone behavior. The results showed around 79-90 % reduction in young modulus of a dense sample [14, 84]. Thus by having SLM80 as a dense sample and introducing proper porosity level with TPMS structures, a better bone substitute might be presented.

5.7 Conclusions

In this chapter, the heat treatment of 500 °C for 1.5 hr. and the optimum L-PBF-AM fabrication parameters combined to improve the shape memory behavior of NiTi. The results presented that using AM instead of conventional methods improved the shape memory response of NiTi samples. Additionally, this study demonstrates the impact of altering L-PBF-AM fabrication parameters more understandable on the shape memory behavior of NiTi. The mechanical results showed that decreasing hatch space from 120 to 80 μm can improve the thermomechanical and shape memory behaviors of NiTi samples, but the ductility response was eliminated during this change. As was expected, the heat treatment significantly developed the shape memory behaviors of all samples. It should be noted that the best shape memory behavior was observed for lower hatch space and aged sample with 7% strain recovery, ~ 100 °C superelastic window, and 24.22 J.cm^{-3} work output. The TTs, thermomechanical, and superelastic responses of aged L-PBF-AM $\text{Ni}_{50.8}\text{Ti}_{9.2}$ with lower hatch space were similar to the same-aged $\text{Ni}_{51}\text{Ti}_{49}$ single crystal in [100] orientation with only a smaller superelastic window.

6 Summary and Future Work

6.1 Summary and Conclusion

The AM PPs govern the solidification characteristics, which in turn controls the microstructure and mechanical properties. It should be noted that SMAs' properties are highly composition, LD, and orientation-dependent, and L-PBF-AM is determined to be a very powerful method to tailor the microstructure and, thus, the mechanical properties. The heat flow during L-PBF-AM, competitive growth mechanisms, and epitaxial growth due to partial re-melting of the previous layer results in the formation of long elongated grains with a preferential crystal orientation along the BD and LD. Therefore, a comprehensive and systematic study is conducted to gain an in-depth understanding of the relationship between the L-PBF-AM process, microstructure, and shape memory properties of NiTi.

In this study, a detailed investigation was carried out on the TTs, microstructure, and shape memory response of L-PBF-AM Ni_{50.8}Ti_{49.2}. At first, the effects of L-PBF-AM PPs such as laser power and hatch spacing were studied on the thermomechanical behavior of NiTi parts. It was shown that selecting the right PPs could improve the mechanical response of the final products. It was concluded that the linear energy density (ratio of laser power to scanning speed) is one of the main parameters to control the shape, size, and energy of the melt pool while hatch spacing does not significantly affect the melt pool shape, but it affects the thermal gradient and cooling rates of the melt pool which is followed by controlling the final texture. However, it should be noted that hatch spacing (and volumetric energy density) strongly influences the microstructure (texture, grain size, porosity level, the overlap of melting pools, secondary phase formation, and the shape of the grains), TTs (thermal history, the number of re-melting and re-heating processes that affects Ni-

evaporation, impurity and precipitate formation), and the mechanical response (strength depends on composition, porosity, and texture) of L-PBF-AM Ni-rich NiTi specimens. It was found that the decrease of laser power from 250 to 100 W, scanning speed from 1250 to 125 mm/s, and hatch spacing from 80 to 40 μm results in altering the texture from the [001] to [111] orientation. Moreover, it was revealed that TTs, microstructure, texture, and the correlated thermo-mechanical response were improved by applying a hatch spacing lower than the laser beam diameter ($<80 \mu\text{m}$ in this study). It was found that by careful selection of PPs, as-fabricated samples can show 6% superelasticity with more than 87% recovery ratio. Additionally, it was proved that employing the same scanning speed for two laser powers of 50 and 100 W resulted in poorer microstructure and mechanical behavior for lower laser power one. It was evident that the applied scanning speed was too fast for 50 W laser power and presented the result of wrong PPs selection, which was followed by failure during fabrication when higher hatch spacing was utilized. Thus, both linear and volumetric energy densities should be considered for successful fabrication of samples and to achieve desirable properties.

Altering fabrication strategy directly impacts re-melting and reheating processes of L-PBF-AM fabrication, which change the crystallographic orientation of the fabricated sample. Therefore, in a systematic study, the same optimum PPs have been utilized to fabricate tensile and compressive $\text{Ni}_{50.8}\text{Ti}_{49.2}$ samples with three different angles concerning the substrate (0, 45, and 90 degrees) in order to formation of the same melting pool shape, thermal gradient direction, and cubic texture alignment in all cases. It was demonstrated that the highest tensile ultimate strength and elongation could be observed where the LD is perpendicular to the BD. In 0 and 90-degree cases, samples used the 90° symmetry

feature of cubic crystal to present similar texture in [100] orientation. In 45-degree specimens, although [100] texture has appeared in BD, LD which was aligned with a diameter of cubic crystal, showed the [110] texture. [001] || LD textured samples showed similar mechanical properties with more than 5% of strain recovery in compression, while the [110] || LD sample exhibited 4.04% stabilized compressive recovery strain after ten cycles under 800 MPa with a higher amount of unrecovered strain even after the heating process. Isothermal under constant stress results revealed that compressive samples presented higher resistance to the appearance of plasticity with illustrating a higher stress window compared to the tensile ones in all cases. However, the highest transformation strain of 5.31 % was obtained for tensile sample in 45-degree case, which has a good agreement with the property of [110] orientation formed in its microstructure. Finally, it could conclude that by adjusting PPs followed by altering melting pool shape and thermal gradient direction and/or by adjusting the relative position of the sample orientation to the BD it is possible to control the cubic crystal to fabricate a sample with a specific orientation along the BD and/or LD.

In the following study, heat treatment as an efficient method to control the TTs and improve the strength of $\text{Ni}_{50.8}\text{Ti}_{49.2}$ alloys was employed to obtain a superior shape memory behavior by adding a post-processing method to L-PBF-AM NiTi. Therefore, L-PBF-AM $\text{Ni}_{50.8}\text{Ti}_{49.2}$ samples fabricated by 250 W laser power, 1250 mm/s scanning speed, and two hatch spacing of 120 (no specific texture) and 80 μm (sharp [100] texture) were selected to present the sensitivity of L-PBF-AM PPs. The XY scanning strategy and the 90-degree angle between BD and substrate were utilized. Additionally, the behavior of conventional NiTi was evaluated to demonstrate the power of L-PBF-AM manufacturing compared to

the previous methods. Specific heat treatment time (1.5 hr) and temperature (550 °C) were chosen based on previous single crystal studies on NiTi in trying to mimic the single crystal behavior of NiTi by L-PBF-AM. The effects of heat treatment on the transformation characteristics (TTs, thermal hysteresis, and recoverable strain) and microstructure of the L-PBF-AM Ni-rich NiTi SMAs have been investigated through transmission electron microscopy, thermal cycling under stress, and isothermal stress-strain experiments. It was found that L-PBF-AM NiTi samples can show improved shape memory response compared to those fabricated by a conventional method as they mimic the response of [001] oriented NiTi single crystals. By introducing aging to the specimens, transformation temperature increased, hysteresis decreased, and strength of the samples significantly improved, attributed to the appearance of coherence Ni-rich precipitates in the microstructure of specimens. Perfect superelastic behavior was observed for aged L-PBF-AM sample, which fabricated with lower hatch space, until 7% strain with ~100 °C superelastic window.

6.2 Future Work

This study has proved that the selection of L-PBF-AM PPs dramatically changes the response of fabricated alloys. Also, L-PBF-AM is a powerful method to tailor the microstructure and, thus, the mechanical properties. Moreover, aging was found to be an extremely effective tool to improve the shape memory response. An excellent time allocation and future works are required to understand every aspect of L-PBF-AM fabrication and the resultant features of laser fabrication on NiTi SMAs. Some of the very potential future studies can be:

- Employing optimum PPs and scanning strategies to grow specific orientation and sharp texture in the BD and LD of L-PBF-AM specimens.
- Applying the optimized fabrication plans to manufacturer complex geometries suitable for tissue engineering and the medical industry.
- Investigating elastocaloric effects on simple and complex geometries with superelastic behavior at room temperature applicable in refrigeration technologies.
- Insitu observations of melt pool to control the texture of L-PBF-AM products by adjusting the PPs.
- Predicting the shape memory behavior and thermal property of L-PBF-AM specimens with simple/complex geometries (such as TMPS structures) by utilizing multi-scale multi-physical models.

7 Contribution

This work has been conducted with the collaboration of University of Toledo and University of Kentucky. Fabrication of NiTi specimens was conducted at Dynamic and Smart Systems Laboratory at the department of Mechanical Industrial and Manufacturing Engineering of the University of Toledo. In microstructure regard, orientation imaging (OI) was done using an FEI Apreo scanning electron microscope (SEM) at 30KV with an EDAX Hikari Super EBSD camera in collaboration with Ohio State University and the Institute of Condensed Matter Chemistry and Technologies for Energy. A transmission electron microscope (TEM) was utilized in collaboration with the University of New Mexico, to characterize the microstructure of aged L-PBF-AM and ingot NiTi.

References

1. Otsuka, K. and C.M. Wayman, *Shape memory materials*. 1999: Cambridge university press.
2. Greninger, A.B. and V.G. Mooradian, *Strain transformation in metastable beta copper-zinc and beta copper-tin alloys*. 1938.
3. Kurdjumov, G.V. and L.G. Khandros, *First reports of the thermoelastic behaviour of the martensitic phase of Au-Cd alloys*. Doklady Akademii Nauk, 1949. **66**: p. 211-213.
4. Chang, L.C. and T.A. Read, *Plastic deformation and diffusionless phase changes in metals-The gold-Cadmium Beta-phase*. Journal of Metals, 1951. **3**(1): p. 47-52.
5. Buehler, W.J., R.C. Wiley, and J.V. Gilfrich, *EFFECT OF LOW-TEMPERATURE PHASE CHANGES ON MECHANICAL PROPERTIES OF ALLOYS NEAR COMPOSITION TINI*. Applied Physics, 1963. **34**(5): p. 1475.
6. Nematollahi, M., et al., *Application of NiTi in assistive and rehabilitation devices: a review*. Bioengineering, 2019. **6**(2): p. 37.
7. Otsuka, K. and C.M. Wayman, *Shape Memory Materials*. 1998: Cambridge University Press. 298.
8. Lagoudas, D.C., *Shape Memory Alloys: Modeling and Engineering Applications*. 1 ed. 2008, New York: Springer.
9. Saghaian, S.M., *Shape memory behavior of single crystal and polycrystalline Ni-rich NiTiHf high temperature shape memory alloys*. 2015.
10. Yoneyama, T. and S. Miyazaki, *Shape memory alloys for biomedical applications*. 2008: Elsevier.
11. Bansiddhi, A., et al., *Porous NiTi for bone implants: a review*. Acta biomaterialia, 2008. **4**(4): p. 773-782.
12. Elahinia, M.H., et al., *Manufacturing and processing of NiTi implants: a review*. Progress in materials science, 2012. **57**(5): p. 911-946.
13. Jani, J.M., et al., *A review of shape memory alloy research, applications and opportunities*. Materials & Design (1980-2015), 2014. **56**: p. 1078-1113.
14. Saedi, S., et al., *Shape memory response of porous NiTi shape memory alloys fabricated by selective laser melting*. Journal of Materials Science: Materials in Medicine, 2018. **29**(4): p. 40.
15. Duerig, T.W., K. Melton, and D. Stöckel, *Engineering aspects of shape memory alloys*. 2013: Butterworth-Heinemann.
16. Otsuka, K. and X. Ren, *Physical metallurgy of Ti-Ni-based shape memory alloys*. Progress in materials science, 2005. **50**(5): p. 511-678.
17. Dadbakhsh, S., et al., *Laser additive manufacturing of bulk and porous shape-memory NiTi alloys: From processes to potential biomedical applications*. MRS bulletin, 2016. **41**(10): p. 765-774.

18. Miyazaki, S. and C. Wayman, *The R-phase transition and associated shape memory mechanism in Ti-Ni single crystals*. Acta metallurgica, 1988. **36**(1): p. 181-192.
19. Šittner, P., et al., *In situ neutron diffraction studies of martensitic transformations in NiTi polycrystals under tension and compression stress*. Materials Science and Engineering: A, 2004. **378**(1–2): p. 97-104.
20. Khalil-Allafi, J., et al., *Quantitative phase analysis in microstructures which display multiple step martensitic transformations in Ni-rich NiTi shape memory alloys*. Materials Science and Engineering: A, 2006. **438–440**(0): p. 593-596.
21. Khalil Allafi, J., X. Ren, and G. Eggeler, *The mechanism of multistage martensitic transformations in aged Ni-rich NiTi shape memory alloys*. Acta Materialia, 2002. **50**(4): p. 793-803.
22. Bataillard, L., J.-E. Bidaux, and R. Gotthardt, *Interaction between microstructure and multiple-step transformation in binary NiTi alloys using in-situ transmission electron microscopy observations*. Philosophical magazine A, 1998. **78**(2): p. 327-344.
23. Nishida, M., et al., *Experimental consideration of multistage martensitic transformation and precipitation behavior in aged Ni-rich Ti-Ni shape memory alloys*. Materials Transactions, 2003. **44**(12): p. 2631-2636.
24. Tang, W., *Thermodynamic study of the low-temperature phase B19' and the martensitic transformation in near-equiatomic Ti-Ni shape memory alloys*. Metallurgical and Materials Transactions A, 1997. **28**(3): p. 537-544.
25. Ma, J., I. Karaman, and R.D. Noebe, *High temperature shape memory alloys*. International Materials Reviews, 2010. **55**(5): p. 257-315.
26. Nishida, M., C.M. Wayman, and T. Honma, *Precipitation processes in near-equiatomic TiNi shape memory alloys*. Metallurgical Transactions A, 1986. **17**(9): p. 1505-1515.
27. Miyazaki, S., et al., *Characteristics of deformation and transformation pseudoelasticity in Ti-Ni alloys*. Le Journal de Physique Colloques, 1982. **43**(C4): p. C4-255-C4-260.
28. Karaca, H., et al., *Shape memory behavior of high strength Ni54Ti46 alloys*. Materials Science and Engineering: A, 2013. **580**: p. 66-70.
29. Sehitoglu, H., et al., *Shape memory and pseudoelastic behavior of 51.5% Ni–Ti single crystals in solutionized and overaged state*. Acta Materialia, 2001. **49**(17): p. 3609-3620.
30. Kaya, I., et al., *Effects of aging on the shape memory and superelasticity behavior of ultra-high strength Ni54Ti46 alloys under compression*. Materials Science and Engineering: A, 2016. **678**: p. 93-100.
31. Miyazaki, S., et al., *The habit plane and transformation strains associated with the martensitic transformation in Ti-Ni single crystals*. Scripta metallurgica, 1984. **18**(9): p. 883-888.
32. Sehitoglu, H., et al., *Compressive response of NiTi single crystals*. Acta Materialia, 2000. **48**(13): p. 3311-3326.
33. Laplanche, G., J. Pfetzinger-Micklich, and G. Eggeler, *Orientation dependence of stress-induced martensite formation during nanoindentation in NiTi shape memory alloys*. Acta Materialia, 2014. **68**: p. 19-31.

34. Karaca, H., et al., *Compressive response of nickel-rich NiTiHf high-temperature shape memory single crystals along the [1 1 1] orientation*. Scripta Materialia, 2011. **65**(7): p. 577-580.
35. Karaca, H., et al., *Superelastic response and damping capacity of ultrahigh-strength [1 1 1]-oriented NiTiHfPd single crystals*. Scripta Materialia, 2012. **67**(5): p. 447-450.
36. Laplanche, G., et al., *Effect of temperature and texture on the reorientation of martensite variants in NiTi shape memory alloys*. Acta Materialia, 2017. **127**: p. 143-152.
37. Kaya, I., et al., *Effects of orientation on the shape memory behavior of Ni₅₁Ti₄₉ single crystals*. Materials Science and Engineering: A, 2017. **686**: p. 73-81.
38. Elahinia, M., *Shape memory alloy actuators: design, fabrication and experimental evaluation*. 2015: John Wiley & Sons.
39. Tang, W., et al., *New modelling of the B2 phase and its associated martensitic transformation in the Ti–Ni system*. Acta materialia, 1999. **47**(12): p. 3457-3468.
40. Wasilewski, R., et al., *Homogeneity range and the martensitic transformation in TiNi*. Metallurgical Transactions, 1971. **2**(1): p. 229-238.
41. Khalil-Allafi, J., A. Dlouhy, and G. Eggeler, *Ni₄Ti₃-precipitation during aging of NiTi shape memory alloys and its influence on martensitic phase transformations*. Acta Materialia, 2002. **50**(17): p. 4255-4274.
42. Frenzel, J., et al., *Influence of Ni on martensitic phase transformations in NiTi shape memory alloys*. Acta Materialia, 2010. **58**(9): p. 3444-3458.
43. Khamei, A.A. and K. Dehghani, *Modeling the hot-deformation behavior of Ni₆₀wt%–Ti₄₀wt% intermetallic alloy*. Journal of Alloys and Compounds, 2010. **490**(1–2): p. 377-381.
44. Turabi, A.S., et al., *Experimental characterization of shape memory alloys*. Shape Memory Alloy Actuators: Design, Fabrication, and Experimental Evaluation, 2015: p. 239-277.
45. Nishida M, Wayman CM, Honma T. Metall Trans 1986;17A:1505.
46. Tirry, W. and D. Schryvers, *Quantitative determination of strain fields around Ni₄Ti₃ precipitates in NiTi*. Acta materialia, 2005. **53**(4): p. 1041-1049.
47. Li, D. and L. Chen, *Shape of a rhombohedral coherent Ti₁₁Ni₁₄ precipitate in a cubic matrix and its growth and dissolution during constrained aging*. Acta materialia, 1997. **45**(6): p. 2435-2442.
48. Bojda, O., G. Eggeler, and A. Dlouhý, *Precipitation of Ni₄Ti₃-variants in a polycrystalline Ni-rich NiTi shape memory alloy*. Scripta materialia, 2005. **53**(1): p. 99-104.
49. Dehghani, K. and A. Khamei, *Hot deformation behavior of 60Nitinol (Ni₆₀ wt%–Ti₄₀ wt%) alloy: Experimental and computational studies*. Materials Science and Engineering: A, 2010. **527**(3): p. 684-690.
50. Carroll, M., C. Somsen, and G. Eggeler, *Multiple-step martensitic transformations in Ni-rich NiTi shape memory alloys*. Scripta Materialia, 2004. **50**(2): p. 187-192.

51. Michutta, J., et al., *Elementary martensitic transformation processes in Ni-rich NiTi single crystals with Ni₄Ti₃ precipitates*. Acta materialia, 2006. **54**(13): p. 3525-3542.
52. Prasher, M. and D. Sen, *Influence of aging on phase transformation and microstructure of Ni 50.3 Ti 29.7 Hf 20 high temperature shape memory alloy*. Journal of Alloys and Compounds, 2014. **615**: p. 469-474.
53. Knowles, K. and D. Smith, *The crystallography of the martensitic transformation in equiatomic nickel-titanium*. Acta Metallurgica, 1981. **29**(1): p. 101-110.
54. Zheng, Y., et al., *The microstructure and linear superelasticity of cold-drawn TiNi alloy*. Materials Science and Engineering: A, 2000. **279**(1): p. 25-35.
55. Sittner, P., Y. Liu, and V. Novák, *On the origin of Lüders-like deformation of NiTi shape memory alloys*. Journal of the Mechanics and Physics of Solids, 2005. **53**(8): p. 1719-1746.
56. Saghaian, S.M., et al., *Effects of aging on the shape memory behavior of Ni-rich Ni50.3Ti29.7Hf20 single crystals*. 2015. **87**: p. 128-141.
57. Sehitoglu, H., et al., *Compressive response of NiTi single crystals*. Acta Materialia, 2000. **48**(13): p. 3311-3326.
58. Gall, K., et al., *On the mechanical behavior of single crystal NiTi shape memory alloys and related polycrystalline phenomenon*. Materials Science and Engineering: A, 2001. **317**(1): p. 85-92.
59. Sehitoglu, H., et al., *Shape memory and pseudoelastic behavior of 51.5%Ni–Ti single crystals in solutionized and overaged state*. Acta Materialia, 2001. **49**(17): p. 3609-3620.
60. Orgéas, L. and D. Favier, *Stress-induced martensitic transformation of a NiTi alloy in isothermal shear, tension and compression*. Acta Materialia, 1998. **46**(15): p. 5579-5591.
61. Liu, Y., et al., *Effect of pseudoelastic cycling on the Clausius–Clapeyron relation for stress-induced martensitic transformation in NiTi*. Journal of Alloys and Compounds, 2008. **449**(1–2): p. 82-87.
62. Nishida, M., et al., *Electron microscopy studies of twin morphologies in B19' martensite in the Ti-Ni shape memory alloy*. Acta metallurgica et materialia, 1995. **43**(3): p. 1219-1227.
63. Gall, K. and H. Sehitoglu, *The role of texture in tension–compression asymmetry in polycrystalline NiTi*. International Journal of Plasticity, 1999. **15**(1): p. 69-92.
64. Gall, K., et al., *Tension–compression asymmetry of the stress–strain response in aged single crystal and polycrystalline NiTi*. Acta Materialia, 1999. **47**(4): p. 1203-1217.
65. Liu, Y., et al., *Effect of texture orientation on the martensite deformation of NiTi shape memory alloy sheet*. Acta materialia, 1999. **47**(2): p. 645-660.
66. Parvizi, S., et al., *Effective Parameters on the Final Properties of NiTi-based Alloys Manufactured by Powder Metallurgy Methods: A Review*. Progress in Materials Science, 2020: p. 100739.
67. CHEN, C., *A study on the machinability of a Ti49.6Ni50.4 shape memory alloy [J]*. Mater Lett, 1999. **40**: p. 27-32.

68. Wu, M.H. *Fabrication of nitinol materials and components*. in *Materials Science Forum*. 2002. Trans Tech Publ.
69. Andani, M.T., et al., *Metals for bone implants. Part 1. Powder metallurgy and implant rendering*. *Acta biomaterialia*, 2014. **10**(10): p. 4058-4070.
70. AYDOĞMUŞ, T. and A.Ş. BOR, *Production and characterization of porous TiNi shape memory alloys*. *Turkish Journal of Engineering and Environmental Sciences*, 2011. **35**(2): p. 69-82.
71. Pattanayak, D.K., et al., *Bioactive Ti metal analogous to human cancellous bone: fabrication by selective laser melting and chemical treatments*. *Acta Biomaterialia*, 2011. **7**(3): p. 1398-1406.
72. Yan, C., et al., *Ti-6Al-4V triply periodic minimal surface structures for bone implants fabricated via selective laser melting*. *Journal of the mechanical behavior of biomedical materials*, 2015. **51**: p. 61-73.
73. Lindner, M., et al., *Manufacturing of individual biodegradable bone substitute implants using selective laser melting technique*. *Journal of Biomedical Materials Research Part A*, 2011. **97**(4): p. 466-471.
74. Jahadakbar, A., et al., *Design, Modeling, Additive Manufacturing, and Polishing of Stiffness-Modulated Porous Nitinol Bone Fixation Plates Followed by Thermomechanical and Composition Analysis*. *Metals*, 2020. **10**(1): p. 151.
75. Read, N., et al., *Selective laser melting of AlSi10Mg alloy: Process optimisation and mechanical properties development*. *Materials & Design (1980-2015)*, 2015. **65**: p. 417-424.
76. Kempen, K., et al., *Processing AlSi10Mg by selective laser melting: parameter optimisation and material characterisation*. *Materials Science and Technology*, 2015. **31**(8): p. 917-923.
77. Li, R., et al., *316L stainless steel with gradient porosity fabricated by selective laser melting*. *Journal of Materials Engineering and Performance*, 2010. **19**(5): p. 666-671.
78. Takaichi, A., et al., *Microstructures and mechanical properties of Co-29Cr-6Mo alloy fabricated by selective laser melting process for dental applications*. *Journal of the mechanical behavior of biomedical materials*, 2013. **21**: p. 67-76.
79. Vandenbroucke, B. and J.P. Kruth, *Selective laser melting of biocompatible metals for rapid manufacturing of medical parts*. *Rapid Prototyping Journal*, 2007.
80. Moghaddam, N.S., et al., *Three dimensional printing of stiffness-tuned, nitinol skeletal fixation hardware with an example of mandibular segmental defect repair*. *Procedia CIRP*, 2016. **49**: p. 45-50.
81. Moghaddam, N.S., et al., *Metallic fixation of mandibular segmental defects: Graft immobilization and orofacial functional maintenance*. *Plastic and Reconstructive Surgery Global Open*, 2016. **4**(9).
82. Jahadakbar, A., et al., *Finite element simulation and additive manufacturing of stiffness-matched niti fixation hardware for mandibular reconstruction surgery*. *Bioengineering*, 2016. **3**(4): p. 36.

83. Moghaddam, N.S., et al., *Anisotropic tensile and actuation properties of NiTi fabricated with selective laser melting*. *Materials Science and Engineering: A*, 2018. **724**: p. 220-230.
84. Saghaian, S.E., et al., *Mechanical and shape memory properties of triply periodic minimal surface (TPMS) NiTi structures fabricated by selective laser melting*. *Bio. Eng. Med.*, 2018. **5**(3): p. 1-7.
85. Bormann, T., et al., *Microstructure of selective laser melted nickel–titanium*. *Materials Characterization*, 2014. **94**: p. 189-202.
86. Saedi, S., et al., *Thermomechanical characterization of Ni-rich NiTi fabricated by selective laser melting*. *Smart Materials and Structures*, 2016. **25**(3): p. 035005.
87. Dadbakhsh, S., et al., *Effect of SLM parameters on transformation temperatures of shape memory nickel titanium parts*. *Advanced Engineering Materials*, 2014. **16**(9): p. 1140-1146.
88. Dadbakhsh, S., et al., *Influence of SLM on shape memory and compression behaviour of NiTi scaffolds*. *CIRP annals*, 2015. **64**(1): p. 209-212.
89. Bayati, P., et al., *Toward low and high cycle fatigue behavior of SLM-fabricated NiTi: considering the effect of build orientation and employing a self-heating approach*. *International Journal of Mechanical Sciences*, 2020: p. 105878.
90. Bormann, T., et al., *Tailoring selective laser melting process parameters for NiTi implants*. *Journal of Materials Engineering and Performance*, 2012. **21**(12): p. 2519-2524.
91. de Wild, M., et al., *Damping of selective-laser-melted NiTi for medical implants*. *Journal of materials engineering and performance*, 2014. **23**(7): p. 2614-2619.
92. Speirs, M., et al. *The effect of SLM parameters on geometrical characteristics of open porous NiTi scaffolds*. in *High Value Manufacturing: Advanced Research in Virtual and Rapid Prototyping: Proceedings of the 6th International Conference on Advanced Research in Virtual and Rapid Prototyping, Leiria, Portugal, 1-5 October. 2013*.
93. Haberland, C., et al. *Additive manufacturing of shape memory devices and pseudoelastic components*. in *Smart Materials, Adaptive Structures and Intelligent Systems*. 2013. American Society of Mechanical Engineers.
94. Haberland, C., et al., *On the development of high quality NiTi shape memory and pseudoelastic parts by additive manufacturing*. *Smart materials and structures*, 2014. **23**(10): p. 104002.
95. Thijs, L., et al., *The influence of process parameters and scanning strategy on the texture in Ti6Al4V part produced by selective laser melting*. 2013. **1**: p. 21-28.
96. Roberts, I.A., et al., *A three-dimensional finite element analysis of the temperature field during laser melting of metal powders in additive layer manufacturing*. 2009. **49**(12-13): p. 916-923.
97. Nadammal, N., et al., *Effect of hatch length on the development of microstructure, texture and residual stresses in selective laser melted superalloy Inconel 718*. *Materials & Design*, 2017. **134**: p. 139-150.

98. Thijs, L., et al., *Strong morphological and crystallographic texture and resulting yield strength anisotropy in selective laser melted tantalum*. Acta Materialia, 2013. **61**(12): p. 4657-4668.
99. Jia, Q. and D. Gu, *Selective laser melting additive manufacturing of Inconel 718 superalloy parts: Densification, microstructure and properties*. Journal of Alloys and Compounds, 2014. **585**: p. 713-721.
100. Amato, K., et al., *Microstructures and mechanical behavior of Inconel 718 fabricated by selective laser melting*. Acta Materialia, 2012. **60**(5): p. 2229-2239.
101. Murr, L., et al., *Microstructure and mechanical behavior of Ti-6Al-4V produced by rapid-layer manufacturing, for biomedical applications*. Journal of the mechanical behavior of biomedical materials, 2009. **2**(1): p. 20-32.
102. Sidambe, A., et al., *Effect of processing parameters on the densification, microstructure and crystallographic texture during the laser powder bed fusion of pure tungsten*. 2019. **78**: p. 254-263.
103. Moghaddam, N.S., et al., *Achieving superelasticity in additively manufactured NiTi in compression without post-process heat treatment*. Scientific reports, 2019. **9**(1): p. 41.
104. Saedi, S., et al., *On the effects of selective laser melting process parameters on microstructure and thermomechanical response of Ni-rich NiTi*. Acta Materialia, 2018. **144**: p. 552-560.
105. Buehler, W.J., J. Gilfrich, and R. Wiley, *Effect of low-temperature phase changes on the mechanical properties of alloys near composition TiNi*. Journal of applied physics, 1963. **34**(5): p. 1475-1477.
106. Otsuka, K. and X. Ren, *Recent developments in the research of shape memory alloys*. Intermetallics, 1999. **7**(5): p. 511-528.
107. Moghaddam, N.S., et al., *Recent advances in laser-based additive manufacturing*. Laser-Based Additive Manufacturing of Metal Parts: Modeling, Optimization, and Control of Mechanical Properties, 2017: p. 1-22.
108. Amerinatanzi, A., et al., *Application of the superelastic NiTi spring in ankle foot orthosis (AFO) to create normal ankle joint behavior*. Bioengineering, 2017. **4**(4): p. 95.
109. Moya, X., S. Kar-Narayan, and N.D. Mathur, *Caloric materials near ferroic phase transitions*. Nature materials, 2014. **13**(5): p. 439-450.
110. Mañosa, L., et al., *Large temperature span and giant refrigerant capacity in elastocaloric Cu-Zn-Al shape memory alloys*. Applied Physics Letters, 2013. **103**(21): p. 211904.
111. Cui, J., et al., *Demonstration of high efficiency elastocaloric cooling with large ΔT using NiTi wires*. Applied Physics Letters, 2012. **101**(7): p. 073904.
112. Hou, H., et al., *Elastocaloric cooling of additive manufactured shape memory alloys with large latent heat*. Journal of Physics D: Applied Physics, 2017. **50**(40): p. 404001.
113. Ossmer, H., et al., *Evolution of temperature profiles in TiNi films for elastocaloric cooling*. Acta materialia, 2014. **81**: p. 9-20.

114. Tušek, J., et al., *A regenerative elastocaloric heat pump*. Nature Energy, 2016. **1**(10): p. 1-6.
115. Tušek, J., et al., *The elastocaloric effect: a way to cool efficiently*. Advanced Energy Materials, 2015. **5**(13): p. 1500361.
116. Elahinia, M., et al., *Fabrication of NiTi through additive manufacturing: A review*. Progress in Materials Science, 2016. **83**: p. 630-663.
117. Hassan, M., M. Mehrpouya, and S. Dawood. *Review of the machining difficulties of nickel-titanium based shape memory alloys*. in *Applied Mechanics and Materials*. 2014. Trans Tech Publ.
118. Shayesteh Moghaddam, N., et al., *Fixation release and the bone bandaid: A new bone fixation device paradigm*. Bioengineering, 2017. **4**(1): p. 5.
119. Shishkovsky, I., I. Yadroitsev, and I. Smurov, *Direct selective laser melting of nitinol powder*. Physics Procedia, 2012. **39**: p. 447-454.
120. Meier, H. and C. Haberland, *Experimental studies on selective laser melting of metallic parts*. Materialwissenschaft und Werkstofftechnik, 2008. **39**(9): p. 665-670.
121. Elahinia, M., et al., *Additive manufacturing of NiTiHf high temperature shape memory alloy*. Scripta Materialia, 2018. **145**: p. 90-94.
122. Krishna, B.V., S. Bose, and A. Bandyopadhyay, *Laser processing of net-shape NiTi shape memory alloy*. Metallurgical and Materials transactions A, 2007. **38**(5): p. 1096-1103.
123. Bandyopadhyay, A., et al., *Application of laser engineered net shaping (LENS) to manufacture porous and functionally graded structures for load bearing implants*. Journal of Materials Science: Materials in Medicine, 2009. **20**(1): p. 29.
124. Malukhin, K. and K. Ehmman, *Material characterization of NiTi based memory alloys fabricated by the laser direct metal deposition process*. 2006.
125. Saedi, S., *Shape Memory Behavior of Dense and Porous NiTi Alloys Fabricated by Selective Laser Melting*. 2017.
126. Lagoudas, D.C., *Shape memory alloys*. Science and Business Media, LLC, 2008.
127. Moghaddam, N.S., et al. *Selective laser melting of Ni-rich NiTi: selection of process parameters and the superelastic response*. in *Behavior and Mechanics of Multifunctional Materials and Composites XII*. 2018. International Society for Optics and Photonics.
128. Moghaddam, N.S., et al. *Influence of SLM on compressive response of NiTi scaffolds*. in *Behavior and Mechanics of Multifunctional Materials and Composites XII*. 2018. International Society for Optics and Photonics.
129. Kruth, J.-P., et al., *Additive manufacturing of metals via Selective Laser Melting: Process aspects and material developments*. 2015.
130. Kruth, J.-P., et al., *Consolidation phenomena in laser and powder-bed based layered manufacturing*. CIRP annals, 2007. **56**(2): p. 730-759.
131. Song, B., et al., *Differences in microstructure and properties between selective laser melting and traditional manufacturing for fabrication of metal parts: A review*. Frontiers of Mechanical Engineering, 2015. **10**(2): p. 111-125.

132. Nematollahi, M., et al., *Additive manufacturing of ni-rich nitihf 20: Manufacturability, composition, density, and transformation behavior*. Shape Memory and Superelasticity, 2019. **5**(1): p. 113-124.
133. Ma, J., et al., *Spatial control of functional response in 4D-printed active metallic structures*. Scientific reports, 2017. **7**: p. 46707.
134. Kusuma, C., *The effect of laser power and scan speed on melt pool characteristics of pure titanium and Ti-6Al-4V alloy for selective laser melting*. 2016.
135. Thijs, L., et al., *A study of the microstructural evolution during selective laser melting of Ti-6Al-4V*. Acta materialia, 2010. **58**(9): p. 3303-3312.
136. Li, R., et al., *Balling behavior of stainless steel and nickel powder during selective laser melting process*. The International Journal of Advanced Manufacturing Technology, 2012. **59**(9-12): p. 1025-1035.
137. Schwartz, A.J., et al., *Electron backscatter diffraction in materials science*. 2000: Springer.
138. Pröbstle, M., et al., *Superior creep strength of a nickel-based superalloy produced by selective laser melting*. Materials Science and Engineering: A, 2016. **674**: p. 299-307.
139. Wang, Y.M., et al., *Additively manufactured hierarchical stainless steels with high strength and ductility*. Nature materials, 2018. **17**(1): p. 63.
140. Sames, W.J., et al., *The metallurgy and processing science of metal additive manufacturing*. International Materials Reviews, 2016. **61**(5): p. 315-360.
141. Bormann, T., et al., *Microstructure of selective laser melted nickel-titanium*. 2014. **94**: p. 189-202.
142. Mehrabian, R., *Rapid solidification*. International Metals Reviews, 1982. **27**(1): p. 185-208.
143. David, S. and J. Vitek, *Correlation between solidification parameters and weld microstructures*. International Materials Reviews, 1989. **34**(1): p. 213-245.
144. Frenzel, J., et al., *Influence of carbon on martensitic phase transformations in NiTi shape memory alloys*. Acta materialia, 2007. **55**(4): p. 1331-1341.
145. Saedi, S., et al., *The influence of heat treatment on the thermomechanical response of Ni-rich NiTi alloys manufactured by selective laser melting*. Journal of Alloys and Compounds, 2016. **677**: p. 204-210.
146. Saghaian, S., et al., *High strength NiTiHf shape memory alloys with tailorable properties*. Acta Materialia, 2017. **134**: p. 211-220.
147. Nematollahi, M., et al., *Laser Powder Bed Fusion of NiTiHf High-Temperature Shape Memory Alloy: Effect of Process Parameters on the Thermomechanical Behavior*. Metals, 2020. **10**(11): p. 1522.
148. Toker, G.P., et al., *Shape memory behavior of NiTiHf alloys fabricated by selective laser melting*. Scripta Materialia, 2020. **178**: p. 361-365.
149. Rolink, G., et al., *Laser metal deposition and selective laser melting of Fe-28 at.% Al*. Journal of Materials Research, 2014. **29**(17): p. 2036.

150. Li, S., et al., *Microstructure characteristics of Inconel 625 superalloy manufactured by selective laser melting*. Journal of Materials Science & Technology, 2015. **31**(9): p. 946-952.
151. Sun, S.-H., K. Hagihara, and T. Nakano, *Effect of scanning strategy on texture formation in Ni-25 at.% Mo alloys fabricated by selective laser melting*. Materials & Design, 2018. **140**: p. 307-316.
152. Tan, C., et al., *Laser Powder Bed Fusion of Ti-rich TiNi lattice structures: Process optimisation, geometrical integrity, and phase transformations*. International Journal of Machine Tools and Manufacture, 2019. **141**: p. 19-29.
153. Glicksman, M.E., *Principles of solidification: an introduction to modern casting and crystal growth concepts*. 2010: Springer Science & Business Media.
154. Dong, Z., et al., *Effect of Hatch Spacing on Melt Pool and As-built Quality During Selective Laser Melting of Stainless Steel: Modeling and Experimental Approaches*. Materials (Basel, Switzerland), 2018. **12**(1): p. 50.
155. Higashi, M. and T. Ozaki, *Selective laser melting of pure molybdenum: Evolution of defect and crystallographic texture with process parameters*. Materials & Design, 2020. **191**: p. 108588.
156. Teichert, N., et al., *Structure and giant inverse magnetocaloric effect of epitaxial Ni-Co-Mn-Al films*. 2015. **91**(18): p. 184405.
157. Saghaian, S.E., et al., *Effect of hatch spacing and laser power on microstructure, texture and thermomechanical properties of LPBF NiTi*. Material Science and Engineering: A, 2021(Submitted).
158. Tan, C., et al., *Selective laser melting of high-performance pure tungsten: parameter design, densification behavior and mechanical properties*. Science and Technology of advanced MaTerialS, 2018. **19**(1): p. 370-380.
159. Takata, N., et al., *Crystallographic features of microstructure in maraging steel fabricated by selective laser melting*. Metals, 2018. **8**(6): p. 440.
160. Jadhav, S.D. *Understanding the texture development in selective laser melted pure copper*. in *4th Workshop on Metal Additive manufacturing, Date: 2019/05/27-2019/06/28, Location: Auditorium 2de hoofdwet, Thermo-Technical institute at KU Leuven campus Heverlee*. 2019.
161. Flemings, M.C., *Solidification Processing*. 2006.
162. Bimber, B.A., et al., *Anisotropic microstructure and superelasticity of additive manufactured NiTi alloy bulk builds using laser directed energy deposition*. Materials Science and Engineering: A, 2016. **674**: p. 125-134.
163. Baghbaderani, K.S., et al., *Mechanical Evaluation Of Selective Laser Melted Ni-Rich Niti: Compression, Tension, And Torsion*. arXiv preprint arXiv:2006.15659, 2020.
164. Safaei, K., et al., *Torsional behavior and microstructure characterization of additively manufactured NiTi shape memory alloy tubes*. Engineering Structures, 2021. **226**: p. 111383.

165. Calandri, M., et al., *Texture and microstructural features at different length scales in inconel 718 produced by selective laser melting*. *Materials*, 2019. **12**(8): p. 1293.
166. Zhang, J., et al., *A review of selective laser melting of aluminum alloys: Processing, microstructure, property and developing trends*. *Journal of Materials Science & Technology*, 2019. **35**(2): p. 270-284.
167. Nematollahi, M., et al., *Building orientation-structure-property in laser powder bed fusion of NiTi shape memory alloy*. *Journal of Alloys and Compounds*, 2021: p. 159791.
168. Yadroitsev, I. and I. Yadroitsava, *Evaluation of residual stress in stainless steel 316L and Ti6Al4V samples produced by selective laser melting*. *Virtual and Physical Prototyping*, 2015. **10**(2): p. 67-76.
169. Liu, Y., et al., *Asymmetry of stress–strain curves under tension and compression for NiTi shape memory alloys*. *Acta materialia*, 1998. **46**(12): p. 4325-4338.
170. Xie, Z., Y. Liu, and J. Van Humbeeck, *Microstructure of NiTi shape memory alloy due to tension–compression cyclic deformation*. *Acta Materialia*, 1998. **46**(6): p. 1989-2000.
171. Saghaian, S., et al., *Tensile shape memory behavior of Ni50. 3Ti29. 7Hf20 high temperature shape memory alloys*. *Materials & Design*, 2016. **101**: p. 340-345.
172. Karaca, H., et al., *Effects of nanoprecipitation on the shape memory and material properties of an Ni-rich NiTiHf high temperature shape memory alloy*. *Acta Materialia*, 2013. **61**(19): p. 7422-7431.
173. Miyazaki, S., et al., *Effect of cyclic deformation on the pseudoelasticity characteristics of Ti-Ni alloys*. *Metallurgical transactions A*, 1986. **17**(1): p. 115-120.
174. Motemani, Y., et al., *Effect of cooling rate on the phase transformation behavior and mechanical properties of Ni-rich NiTi shape memory alloy*. *Journal of Alloys and Compounds*, 2009. **469**(1-2): p. 164-168.
175. Karaca, H., et al., *NiTiHf-based shape memory alloys*. *Materials Science and Technology*, 2014. **30**(13): p. 1530-1544.
176. Kaya, M., et al., *The effect of solution treatment under loading on the microstructure and phase transformation behavior of porous NiTi shape memory alloy fabricated by SHS*. *Journal of Alloys and Compounds*, 2009. **475**(1-2): p. 378-382.
177. Uchil, J., K.G. Kumara, and K. Mahesh, *Effects of heat treatment temperature and thermal cycling on phase transformations in Ni–Ti–Cr alloy*. *Journal of alloys and compounds*, 2001. **325**(1-2): p. 210-214.
178. Zarinejad, M., Y. Liu, and Y. Tong, *Transformation temperature changes due to second phase precipitation in NiTi-based shape memory alloys*. *Intermetallics*, 2009. **17**(11): p. 914-919.
179. Meng, X., et al., *Effect of aging on martensitic transformation and microstructure in Ni-rich TiNiHf shape memory alloy*. *Scripta materialia*, 2006. **54**(9): p. 1599-1604.
180. Bigelow, G., et al., *Load-biased shape-memory and superelastic properties of a precipitation strengthened high-temperature Ni50. 3Ti29. 7Hf20 alloy*. *Scripta Materialia*, 2011. **64**(8): p. 725-728.

181. Acar, E., et al., *Role of aging time on the microstructure and shape memory properties of NiTiHfPd single crystals*. Materials Science and Engineering: A, 2013. **573**: p. 161-165.
182. Saghaian, S.M., et al., *Effects of aging on the shape memory behavior of Ni-rich Ni₅₀.₃Ti₂₉.₇Hf₂₀ single crystals*. Acta Materialia, 2015. **87**: p. 128-141.
183. Saedi, S., et al., *Texture, aging, and superelasticity of selective laser melting fabricated Ni-rich NiTi alloys*. Materials Science and Engineering: A, 2017. **686**: p. 1-10.
184. Haberland, C., H. Meier, and J. Frenzel. *On the properties of Ni-rich NiTi shape memory parts produced by selective laser melting*. in ASME 2012 conference on smart materials, adaptive structures and intelligent systems. 2012. American Society of Mechanical Engineers.
185. Saburi, T., *Ti-Ni shape memory alloys*. Shape memory materials, 1998: p. 49-96.
186. Zheng, Y., et al., *Effect of ageing treatment on the transformation behaviour of Ti–50.9 at.% Ni alloy*. Acta Materialia, 2008. **56**(4): p. 736-745.
187. Zhou, Y., et al., *Origin of 2-stage R-phase transformation in low-temperature aged Ni-rich Ti–Ni alloys*. Acta materialia, 2005. **53**(20): p. 5365-5377.
188. Allafi, J.K., X. Ren, and G. Eggeler, *The mechanism of multistage martensitic transformations in aged Ni-rich NiTi shape memory alloys*. Acta Materialia, 2002. **50**(4): p. 793-803.
189. Kaya, I., et al., *Positive and negative two-way shape memory effect in [111]-oriented Ni₅₁Ti₄₉ single crystals*. Materials Science and Engineering: A, 2015. **639**: p. 42-53.
190. Otsuka, K., T. Sawamura, and K. Shimizu, *Crystal structure and internal defects of equiatomic TiNi martensite*. Physica status solidi (a), 1971. **5**(2): p. 457-470.
191. Sam, J., et al., *Tensile actuation response of additively manufactured nickel-titanium shape memory alloys*. Scripta Materialia, 2018. **146**: p. 164-168.
192. Gall, K., et al., *The influence of aging on critical transformation stress levels and martensite start temperatures in NiTi: part II—discussion of experimental results*. Journal of engineering materials and technology, 1999. **121**(1): p. 28-37.
193. Gall, K., et al., *Fracture of precipitated NiTi shape memory alloys*. International Journal of Fracture, 2001. **109**(2): p. 189-207.
194. Kaya, I., *Shape memory behavior of single and polycrystalline nickel rich nickel titanium alloys*. 2014.
195. Liu, Y. and S. Galvin, *Criteria for pseudoelasticity in near-equiatomic NiTi shape memory alloys*. Acta Materialia, 1997. **45**(11): p. 4431-4439.
196. Cui, J., et al., *Combinatorial search of thermoelastic shape-memory alloys with extremely small hysteresis width*. Nature materials, 2006. **5**(4): p. 286-290.
197. Karaca, H., et al., *Effects of aging on [1 1 1] oriented NiTiHfPd single crystals under compression*. Scripta Materialia, 2012. **67**(7-8): p. 728-731.
198. Gall, K., et al., *Tension–compression asymmetry of the stress–strain response in aged single crystal and polycrystalline NiTi*. Acta Materialia, 1999. **47**(4): p. 1203-1217.

VITA

EDUCATION

- Ph.D., Mechanical Engineering**, University of Kentucky, 2016– **Expected** May 2021
Thesis: Tailoring texture, microstructure, and shape memory behavior of NiTi alloys fabricated by L-PBF-AM
GPA: 4.0
- M.S., Mechanical Engineering**, Islamic Azad University, 2013 – 2015
Thesis: Computational analysis of airflow in the upper part of human respiratory system
- B.S., Mechanical Engineering**, Isfahan University of Technology, 2005-2011

WORK EXPERIENCE

- 01/2021 – PRESENT University of Louisville, Louisville, KY, USA
Research Engineer
- 01/2016 – 12/2020 University of Kentucky, Lexington, KY, USA
Graduate Assistant

HONORS

- Outstanding **Ph.D.** student in the Mechanical Engineering department at University of Kentucky (2018-2019)
- Outstanding **Master** student in the Mechanical Engineering department at the Azad University (2014-2015)

PUBLICATIONS

1. **High strength NiTiHf shape memory alloys with tailorable properties**
SM Saghaian, HE Karaca, H Tobe, AS Turabi, S Saedi, **Sayed E. Saghaian**, YI Chumlyakov, RD Noebe 2017
Acta Materialia 134, 211-220
2. **Shape memory response of porous NiTi shape memory alloys fabricated by selective laser melting**
Soheil Saedi, **Sayed E. Saghaian**, Ahmadreza Jahadakbar, Narges Shayesteh Moghaddam, Mohsen Taheri Andani, Sayed M Saghaian, Y Charles Lu, Mohammad Elahinia, Haluk E Karaca 2018
Journal of Materials Science: Materials in Medicine 29 (4), 40
3. **Anisotropic tensile and actuation properties of NiTi fabricated with selective laser melting** 2018

Narges Shayesteh Moghaddam, **Sayed E. Saghaian**, Amirhesam Amerinatanzi, Hamdy Ibrahim, Peizhen Li, Guher P Toker, Haluk E Karaca, Mohammad Elahinia
Materials Science and Engineering: A 724, 220-230

- 4. Mechanical and shape memory properties of triply periodic minimal surface (TPMS) NiTi structures fabricated by selective laser melting**
Sayed E. Saghaian, A Amerinatanzi, NS Moghaddam, A Majumdar, M Nematollahi, S Saedi, M Elahinia, HE Karaca
Biology, Engineering and Medicine 3 (5), 1-7 2018
- 5. Selective laser melting of Ni-rich NiTi: selection of process parameters and the superelastic response**
Narges Shayesteh Moghaddam, Soheil Saedi, Amirhesam Amerinatanzi, **Sayed E. Saghaian**, Ahmadreza Jahadakbar, Haluk Karaca, Mohammad Elahinia
Behavior and Mechanics of Multifunctional Materials and Composites XII 10596, 105960W 2018
- 6. Influence of SLM on compressive response of NiTi scaffolds**
Narges Shayesteh Moghaddam, Soheil Saedi, Amirhesam Amerinatanzi, Ahmadreza Jahadakbar, **Sayed E. Saghaian**, Haluk Karaca, Mohammad Elahinia
Behavior and Mechanics of Multifunctional Materials and Composites XII 10596, 105960H 2018
- 7. Additive Manufacturing of Ni-Rich NiTiHf20: Manufacturability, Composition, Density, and Transformation Behavior**
M. Nematollahi, G. Toker, **S. E. Saghaian**, J. Salazar, M. Mahtabi, O. Benafan, H. Karaca, M. Elahinia
Shape Memory and Superelasticity, 5(1), pp 113–124 2019
- 8. Shape memory behavior of Ni45Mn40Co5Sb10-xBx magnetic shape memory alloys**
Yildirim Aydogdu, Ali Sadi Turabi, Bhargava Boddeti, **Sayed E. Saghaian**, Ayse Aydogdu, Gokhan Kilic, Omar Abboosh, Haluk Ersin Karaca
Journal of Thermal Analysis and Calorimetry (JTAC), 1-11 2019
- 9. Shape memory behavior of NiTiHf alloys fabricated by selective laser melting**
Guher P Toker, Mohammadreza Nematollahi, **Sayed E Saghaian**, Keyvan S Baghbaderani, Othmane Benafan, Mohammad Elahinia, Haluk E Karaca
Scripta Materialia 178, 361-365 2020
- 10. Laser Powder Bed Fusion of NiTiHf High-Temperature Shape Memory Alloy: Effect of Process Parameters on the Thermomechanical Behavior**
Mohammadreza Nematollahi, Guher Toker, Keyvan Safaei, Alejandro Hinojos, **Sayed E. Saghaian**, Othmane Benafan, Michael J. Mills, Haluk karaca, Mohammad Elahinia
Metals, 10 (11), 1522 2020
- 11. Building orientation-structure-property in laser powder bed fusion of NiTi shape memory alloy**
Mohammadreza Nematollahi, **Sayed E. Saghaian**, Keyvan Safaei, Parisa Bayati, Paola Bassani, Carlo Biffi, Ausonio Tuissi, Haluk Karaca, Mohammad Elahinia
Journal of Alloys and Compounds, 159791 2021

- 12. Load-induced local phase transformation and modulus of shape memory alloys by spherical indentation**
Sayed E. Saghaian, Y.C. Lu, Haluk E. Karaca, Sayed M. Saghaian, 2021
ASME Journal of Engineering Materials and Technology, **Submitted**
- 13. Effect of hatch spacing and laser power on microstructure, texture and thermomechanical properties of LPBF NiTi**
Sayed E. Saghaian, Mohammadreza Nematollahi, Guher Pelin Toker, Alejandro Hinojos, Narges Shayesteh Moghaddam, Soheil Saedi, Charles Y. Lu, Mohammad Javad Mahtabi, Michael J. Mills, Mohammad Elahinia, Haluk E. Karaca 2021
Material Science and Engineering: A, **Submitted**
- 14. Superior shape memory behavior of additively manufactured Ni-rich NiTi by precipitates hardening method**
Sayed E. Saghaian, Mohammadreza Nematollahi, Guhar P. Toker, Sayed M. Saghaian, Narges Shayesteh Moghaddam, Mohammad Elahinia, Haluk Karaca 2021
Acta Materialia, **Submitted**
- 15. Composition Dependence of Shape Memory Response in High-Temperature NiTiHfPd Alloys**
Soheil Saedi, Guher Toker, **Sayed E. Saghaian**, Dipak Banerjee, Emre Acar, and Haluk Karaca 2021
Metallurgical and Materials Transactions A, **Submitted**